UNIVERSITÀ
DEGLI STUDI
FIRENZE

DOTTORATO DI RICERCA IN

INTERNATIONAL DOCTORATE IN ATOMIC AND MOLECULAR PHOTONICS

CICLO XXXIV

COORDINATORE Prof. DIEDERIK S. WIERSMA

Transient Absorption Spectroscopy: a Fundamental Tool for Progress in Medical Therapies, Renewable Energies and Electronic Devices

Settore Scientifico Disciplinare CHIM/02-FIS/03

Dottorando

Dott. Maria Taddei

Tutore

Dott. Mariangela Di Donato

Coordinatore

Prof. Diederik S. Wiersma

Anni 2018/2022

Contents

Introduction

One of the major challenges for researchers in chemistry is that of controlling chemical reactions, among which light-driven processes are particularly relevant. The photoexcitation of a molecule indeed allows to induce fundamental processes by converting light energy into chemical energy without being invasive.
In nature, many chemical and biological processes result from light-driven phenomena. The most known is the photosynthesis of living plants, where solar light is the external stimulus for the production of the oxygen necessary for life. For many years chemists have tried to mimic the extraordinary light-harvesting ability of green plants, in the attempt to duplicate the events in photosynthesis using model compounds. In this way, *artificial* photosynthetic systems were developed for harnessing the free and green energy of sun [1].
Conversion of light energy into chemical energy, not only remains a powerful mean for the production of renewable energy sources, but it is also becoming a convenient mean to induce and control different kinds of processes in different fields. From medical therapies to computer electronic devices, from renewable energies to catalysis of industrial procedures, light-driven chemical reactions are the central crux for an extended ensemble of events.
All of that is mostly associated with the fact that light is an ideal external stimulus: it is non-invasive, in most cases produces no contamination from the medium where the light-sensitive system is embedded, it is orthogonal toward most processes and its wavelength can be precisely tuned with the result of high spatial and temporal resolutions.
In this thesis, transient spectroscopies have been extensively used to characterize several light-driven reactions, promoted in molecules which can find an application in different research fields. Among them, some examples we studied are *Donor-Acceptor* molecular systems, used in the important application of Photodynamic Therapy as Triplet Photosensitizers. In this therapy, the photoactive molecule induces the production of singlet oxygen that is a reactive species determining the disruption of cancer cells. We have furthermore characterized *Organic Dyes* with high absorbance and fluorescence quantum yield, whose application as solar concentrators for the production of innovative solar cells is an important tool for the development of renewable energy sources. A deep analysis has been performed on *Photochromic Molecules*, able of switching between two conformations in a completely reversible light-activated manner. These systems are relevant for countless applications of optical, electronic and biological switching devices.
This PhD thesis is dived as follows. In the first chapter, the Ultrafast Spectroscopic technique called Transient Absorption Spectroscopy (TAS) is presented. Particularly, the first part is centered on the two experimental set-ups used for the acquisition of data, while a second part focuses on the method of data treatment used for the analysis of results. The second and third chapters are centered

on the first class of light activated molecules studied in our laboratories, called Triplet Photosensitizers. An introductory discussion (chapter two) presents two photoinduced processes that determine high triplet quantum yield and the molecular structures mostly used for each of them. This section is followed by the presentation of the experimental results on three particular Donor-Acceptor systems (chapter three).
During the course of the PhD, we studied also two other types of molecules. A single chapter for each of the two systems is presented, showing both a brief description of the theoretical and molecular background and a deep description of the experimental data recorded. Particularly, in chapter four the analysis of the photophysical properties of a new family of organic dyes designed for application as Luminescent Solar Concentrators is presented. Chapter five reports the example of a family of hydrazone molecules used as molecular photoswitches, gathering all the spectroscopic characterization performed, using Uv-visible and IR static and transient spectroscopies.
Finally, a general conclusion resumes the work carried on during these three years and points out the targets achieved.

Chapter 1

Ultrafast spectroscopic techniques

Non-linear spectroscopies are a powerful instrument through which it is possible to describe complex systems composed of interacting molecules. In fact, in these systems the use of classical linear spectroscopies does not allow to extrapolate all the correlations hidden in the complexity of spectra, revealing the dynamic events taking place in the system [2]. Particularly, ultrafast spectroscopies are non-linear techniques where the interaction between multiple external radiation fields and a molecular system induces a non-linear response of the sample polarization.
The interaction with the external field induces a coherent oscillation of the sample dipoles, determining a macroscopic dipole moment (polarization) which acquires the oscillating properties of the incoming radiation fields. The oscillating polarization creates an electromagnetic field which is called Signal field, whose wave vector is correlated and established by the direction of the external fields.

$$P_i = \chi_{ij}E_j + \chi^{(2)}_{ijk}E_jE_k + \chi^{(3)}_{ijkl}E_jE_kE_l + ... \tag{1.1}$$

The multiple fields acting on the sample induce a non-linear response of the specific property of the material called susceptibility (χ_{ij}), which represents the degree of polarization of a sample in response to the applied electromagnetic wave. Several perturbations of the susceptibility introduce new contributions to the polarization term with orders higher than the first. The order of each contribution is given by the number of electric fields interacting with the sample and all these factors together are collected as signal field of the experiment.
Most of the analyzed samples are isotropic media, therefore all the even terms in the polarization expansion are zero. This implies that the third order of susceptibility is the first and simplest source of non-linear signal to be recorded.
Three external fields $E_iE_jE_k$ are applied to the sample. The time sequence and geometry combination of their wave vectors determine the different type of experiment. Each experiment provides the measurement of different effects and properties of the system.
These information are contained in the signal recorded by the detector. In fact, the signal S(t) is the convolution between the molecular response function R($t-\tau$), holding the properties of the system, and the Instrument Response Function (IRF, G(τ)), expressing how the instrument responds to the measurement of a temporally tight impulse (δ).

$$S(t) = \int R(t-\tau)G(\tau)\,dt \tag{1.2}$$

These contributions can be separated by a deconvolution once that the instrumental function is determined. Two different ways can be used to calculate the IRF of the experiment, that is performing an experiment of Heterodyne Detected - Optical Kerr Effect (OHD-OKE) on a reference, or recording the spectrum of a signal due to Stimulated Raman Gain (SRG) whose response function is actually instantaneous.

In the two following sections, we will present the different experiments of non linear spectroscopy that we used to study the molecular systems of interest for this work of thesis.

1.1 UV-Visible Transient Absorption Spectroscopy

Transient absorption spectroscopy (TAS) is an ultrafast technique that follows the deactivation pathway of a molecule through its absorbing and emissive excited states. It is also called *pump-probe* spectroscopy.
TAS is a four-wave mixing experiment where the wave vectors of the three applied fields follow a specific spatial arrangement. The definition of the temporal sequence of the fields is very important and all the fields must be considered as very short pulses of electromagnetic radiation (impulsive disturbance). Moreover some of the fields can be temporally coincident while others can be spaced by a specific time interval chosen for the experiment.
In TAS experiments, the first two electric fields interact with the sample at the same time and together they represent the so-called *pump* field (figure 1.1). The third pulse is instead called *probe* field and it reaches the sample at a different and variable time delay τ.

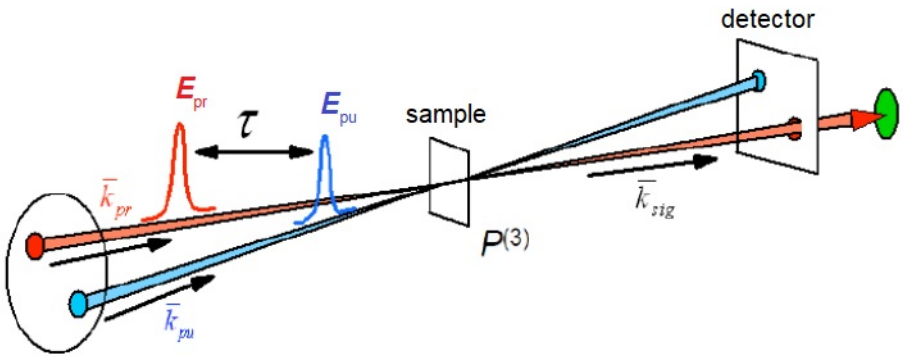

Figure 1.1: Spatial and temporal geometry of the three electric fields used for pump-probe measurements.

This combination of fields, with the first two temporally and spatially coincident, determines an oscillating third-order polarization. Given the specific wave vectors geometry used in TAS, the response of the sample is spatially overlapped to the probe field.
The two first pulses, as pump field of the experiment, promote the system to one of its excited states. The consequent time evolution of the excited system is then followed in time through the use of a probe pulse, reaching the sample with a variable time delay with respect to the pump. Thanks to the femtosecond

time duration of both pump and probe fields and thanks to the short time delays between their arrival on the sample, the system absorbs the probe while still in its excited state. A gradual increase of the pump-probe delay allows probing the deactivation pathway from the reached excited state back to the ground state.
A simplifying representation of a transient absorption experiment can be reported considering a three-level system. Electric fields interact with three electronic or vibrational states of the sample $|0\rangle\,|1\rangle\,|2\rangle$. This interaction induces three events: absorption from the excited state, stimulated emission from the excited state and bleaching of the ground state (figure 1.2).

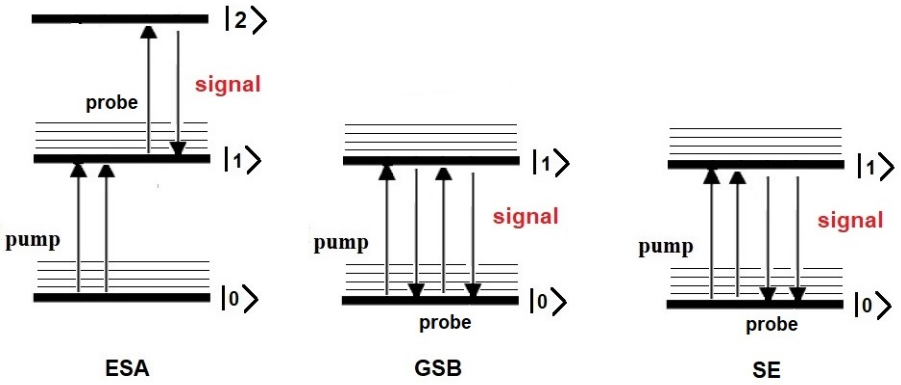

Figure 1.2: Three levels scheme representation of the events induced by TAS: excited state absorption (ESA), ground state bleaching (GSB), stimulated emission (SE).

1. Excited State Absorption (ESA): once the system is brought into its excited state because of the incoming pump pulse, the probe beam brings population in the coherent state $\langle 2\,|\,1\rangle$. The resulting signal oscillates with a frequency relative to the energy difference between the two states (ω_{12}) that negatively interferes with the probe, producing absorption.

2. Ground State Bleaching (GSB): the two pump pulses do not determine the population of the excited state, but the final interacting field is absorbed by the population at the ground state. The resulting coherence produces the emission of a signal field at the frequency ω_{01}.

3. Stimulated Emission (SE): the two pump pulses bring population at the excited state from which the probe stimulates radiative deactivation to the ground state. The resulting signal positively interferes with the probe, producing emission.

The final oscillating polarization given by all these three contributions contains the frequencies relative to the energy of the two excited states of the system (ω_{01} and ω_{12}). To be in resonance with the three-level system, the probe pulse must contain these frequencies and the emitted signal must be recollected splitting the different oscillating contributions with a spectrometer. The stimulated emission signal and the ground state bleaching are recorded at frequency ω_{01}, while at ω_{21} the signal contains the contribution from the excited state absorption.
In case of *UV-Visible* transient absorption spectroscopy, the pump pulse (E_{pu}) is characterized by a wavelength in the UV-visible range (350-700 nm) that excites

the molecules to one of their electronic excited states. The probe pulse is instead a white continuum band, able to probe a large spectral region and to evidence the changes in the absorption spectrum of the sample before and after excitation.

1.1.1 Experimental Setup

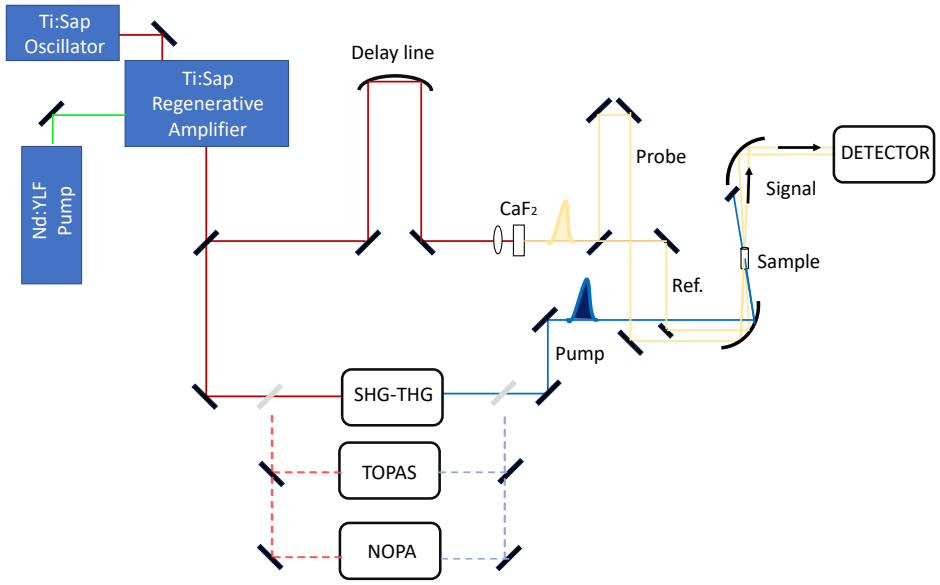

Figure 1.3: TAS setup.

The experimental setup used for the measurements is based on a homemade femtosecond Ti:sapphire laser whose active medium is a sapphire bar (Al_2O_3) doped with Ti^{3+} ions. Through phase locking of the longitudinal modes, this femtosecond oscillator gives as output a final pulse train characterized by a repetition rate of 82 MHz, a single pulse duration of 70 fs, a central wavelength of 800 nm and an energy per pulse of 6 nJ. The time duration of these pulses is actually very short, but their energy is too low for carrying out a transient absorption experiment or to generate in the sample a concentration of excited state molecules such as to provide a detectable signal. The pulse train is thus sent to a Ti:sapphire regenerative amplifier in which decompression, amplification and recompression are carried out, through prisms and grids positioned according to a specific geometry. This process reduces the repetition rate of the pulses and significantly increases their energy, leaving their spectral and temporal properties as much unchanged as possible.
The pulses coming out from the regenerative amplifier have 1 kHz repetition rate, 150 fs duration, 800 nm central wavelength and an energy per pulse of 400-450µJ. With a wedged window the amplified beam is divided into two parts.
The transmitted portion is used to generate the pump pulses. Depending on the

desired excitation wavelength, second harmonic generation using a BBO crystal or parametric amplification can be exploited. In case of second harmonic generation, the 800 nm pulses are focused on a conveniently cut BBO crystal, generating pulses at 400 nm. Using the same principle, third harmonic pulses at 266 nm can also be generated. To generate intense light in range of 400-700 nm, a Non Collinear Optical Parametric Amplifier (NOPA) can be used. In this system a radiation at 400 nm and a white light pulse generated with a sapphire plate are sent on the same BBO crystal. By adjusting their entering angle and their time delay ("phase matching" conditions), broad visible pulses are generated and the wavelength matching the absorption of the sample is extracted using appropriate interference filters. Pump polarization is generally set to 54.7° with respect to probe (magical angle) by rotating a $\lambda/2$ plate. This allows avoiding the contribution of orientational effects in the sample.
The reflected part of the beam (5%) is used to produce the probe pulse and the reference pulse. The beam is focused on a sapphire or calcium fluoride plate and, due to a non-linear optical effect, the radiation at 800 nm is converted into coherent polychromatic light. The probe beam is then collimated by a spherical mirror and divided into two portions by another beam splitter, generating the reference and probe beams. Both probe and reference are focused on the sample through a spherical mirror, together with the pump beam.

The time delay τ between pump and probe is introduced by sending the portion of the 800 nm beam used for probe generation through a motorized and computer-controlled translation stage (delay line). The smallest motor step is about 30 µm, which corresponds to 100 fs delay and the range of analysis can be set between -5 ps to 1.5 ns.
TAS measurements are carried out in a quartz cell (2 mm thick). Since the sample solution is illuminated by a high peak power radiation, the sample cell is inserted into a movable stage to avoid the accumulation of photoproducts. Once passed through the sample, signal, probe and reference beams are directed towards a flat field monochromator that recreates an image of the scattered spectrum. This image is then imprinted on a double silicon diode array which acts as detector (homemade CCD detector).
.

1.2 Uv-visible pump and Infrared probe Transient Absorption Spectroscopy

While transient absorption spectroscopy in the visible range can give information about the electronic excited states of a molecule, showing molecular interactions like energy and electron transfer, it is not able to resolve the structural modifications associated to these dynamics.
However non-radiative deactivation pathways are dominated by structural/vibrational changes. Their detection and assignation are fundamental in the characterization of a photoinduced process of a photoactive material. Vibronic couplings and thermal relaxations are phenomena taking place on the ultrafast timescale (few picoseconds) and they rule most of the transitions between excited states [3].
In order to deeply investigate the structural dynamics in a complex molecular system (figure 1.4), it is necessary to combine visible and infrared transient anal-

ysis. To this purpose, TAS experiments can be performed with a visible pump that excites the system in one of its *electronic* excited states and with an infrared probe exciting the excited state *active vibrational modes*. In the following figure the two phenomena of Excited state vibrational absorption (ESA) and ground state bleaching (GSB) induced by this kind of experiment are presented.

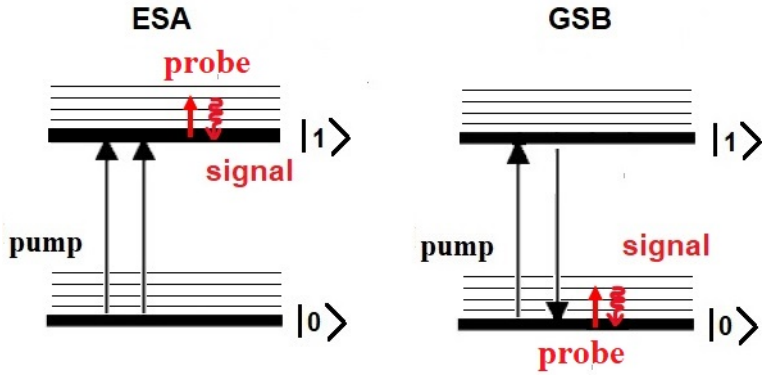

Figure 1.4: Energy levels scheme representation of the events induced by VIs-IR TAS: excited state infrared absorption (ESA) and ground state bleaching (GSB).

Excited state vibrational absorption (ESA) bands allow to follow the structural evolution of the excited state, whereas transient bleaching bands (GSB) are directly related to the recovery of the ground state.
Usually, vibrational spectra of molecules in their excited state show frequency shifts with respect to the same mode in the ground state. This is due to the structural or electronic changes taking place in the excited molecule. The down or up shift of a specific vibrational mode gives information about changes of strength and localization of a specific bond and it provides a significant insight into the transient structures. However, IR transient spectra of complex molecules like those considered here are rather crowded and in many cases the bands measured with TAS consist of the superposition of several normal modes. As we will see in chapter 5, extracting structural information from the analysis of the transient data is not immediate.

1.2.1 Experimental Setup

The following figure presents a schematic view of the Uv-visible pump and Infrared probe Transient Absorption Spectroscopy set-up. The experiment is characterized by a pump-probe geometry, with the first and second pump pulses coincident in time and space.

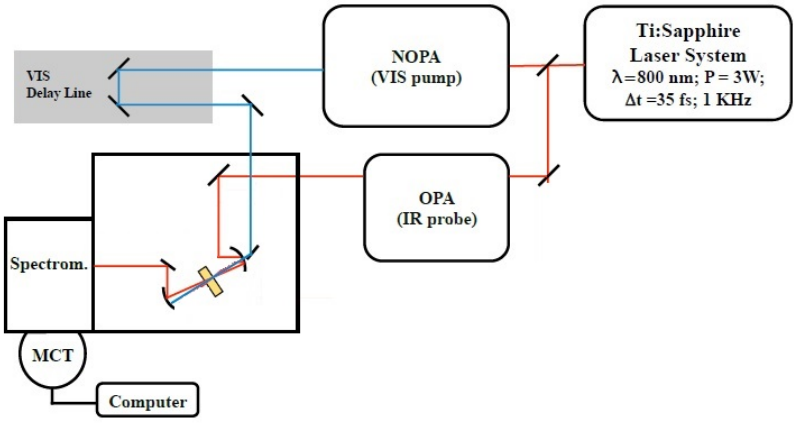

Figure 1.5: Schematic view of the IR-TAS setup.

The source of the three ultrashort laser pulses used for the Vis-IR TAS experiment is a Ti:Sapphire oscillator/regenerative amplifier, operating at 1 kHz with central wavelength at 800 nm with a pulse duration of 40 fs. The output beam is split to generate both the mid-IR probe (1200-1800 cm^{-1}) and the Visible (400-450 nm) pump. Visible pump of different wavelengths are generated by adjusting the beams entering angle and time delay.
The infrared probe is generated using a homemade two-stage optical parametric amplifier (OPA). Here, two near Ir pulses called signal and idler are superimposed in a AgGaS2 crystal determining Difference Frequencies Generation (DFG).
The VIS pump at 400 nm is generated through Second Harmonic Generation (SHG), focusing the 800 nm pulses on a BBO crystal.
Both pump and probe beams are focused on the sample in a 150 micrometers diameter spot. Also in this case, the polarization of the pump is set to the magic angle with respect to that of the probe by rotating a $\lambda/2$ plate. In order to vary the time delay between pump and probe from -5 ps to 1.5 ns, a delay line is set along the pump path.
After the sample, the signal is dispersed in a spectrometer and collected by the detector.

1.3 Data treatment

The following data treatment is valid for both the analysis of Uv-Visible and Infrared data recorded in our laboratories. In both the transient absorption experiments, spectra are acquired at different time delays between pump and probe and they are expressed as a differential absorption of sample (ΔA).

$$\Delta A(\lambda, \tau) = A_{on} - A_{off} = -log(T(\lambda, \tau)) \tag{1.3}$$

If we talk in terms of Transmittance T (1/A), the transient transmittance ΔT represents the ratio between the intensity of the light arriving at the detector in the presence of the pump pulse ($I(\lambda, \tau)$) and that collected in the absence of the pump pulse ($I_0(\lambda, \tau)$). In order to reduce signal fluctuations, the transient transmittance is normalized by the intensity of a reference beam.

$$\Delta T(\lambda, \tau) = \frac{I(\lambda, \tau)}{I_{ref}(\lambda)} \frac{I_{ref}(\lambda)}{I_0(\lambda, \tau)} \tag{1.4}$$

The differential probe intensity also contains the stationary fluorescence of the sample and the scattered pump light, both of which must be subtracted to obtain the pure ΔA. For this reason, all these factors are acquired in presence of the lone pump pulse and they are analytically subtracted by the acquisition software. The analysis of the differential transient absorption ΔA and its time evolution after excitation allows to characterize the excited state deactivation pathway of the samples:

1. The Excited State Absorption (ESA) is a negative transmittance signal, since the destructive interference between the probe and signal fields determines a reduction of the transmitted intensity recorded by the detector. Following equation 1.3, the relative ΔA band is so a *positive* spectral contribution (figure 1.6).

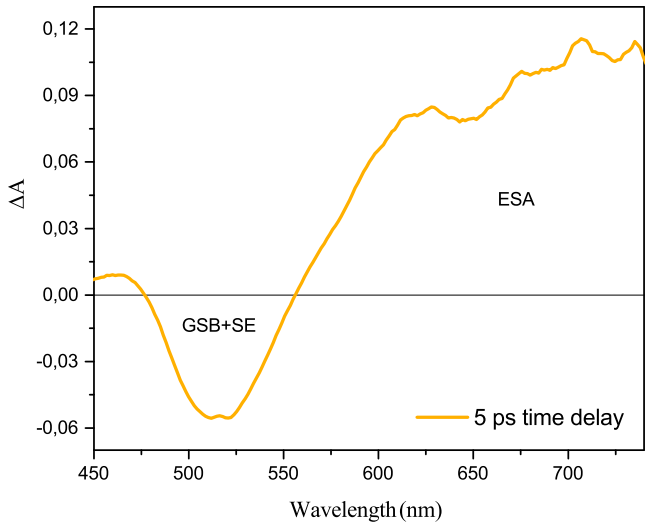

Figure 1.6: Example of a differential spectrum recorded by transient absorption spectroscopy at a specific time delay.

2. The Ground State Bleaching (GSB) represents an increase of the light transmitted to the detector. This signal is given by that part of the probe pulse that excites the residual non excited population of the ground state. Therefore, the ΔA signal is negative because part of the ground state population has been already excited by the pump pulse (negative band in figure 1.6).

3. The Stimulated Emission (SE) is also a ΔA negative band because the emitting contribution is added with constructive interference to the probe field and the relative final transmittance increases (negative band in figure 1.6).

Global analysis is an advantageous method for analyzing the results provided by transient absorption spectroscopy. It allows to simplify as much as possible the description of the system and to estimate its essential properties. The analysis consists in simultaneously fitting all the recorded kinetic traces over the entire spectral range of the probe by means of exponential decay functions. In this way

it is possible to obtain the average decay times of the whole spectrum and to identify all the transitions between different states.
To perform the analysis, it is necessary to use a model based on a specific kinetic scheme. In this thesis, all the analyses reported were carried out using the software Glotaran [4]. The first step of Glotaran analysis consists in performing the "Singular value decomposition" (SVD). This procedure reduces all data to a diagonal matrix S of orthogonal bases: one of time-independent spectra and the other of wavelength-independent kinetics. The singular values on the diagonal of the S matrix indicates the number of independent kinetic components relating to the single species/transient states through which the deactivation proceeds.
At this point, the analyzer has to decide the kinetic model followed by the deactivation thought the excited states, with the two possible options of global or target analysis. In case of global analysis, the deactivation pathway is outlined through a linear sequential model where each step proceeds from a state at higher energy to a different state at lower energy. In target analysis, the kinetic evolution follows a compartmental model (figure 1.7).

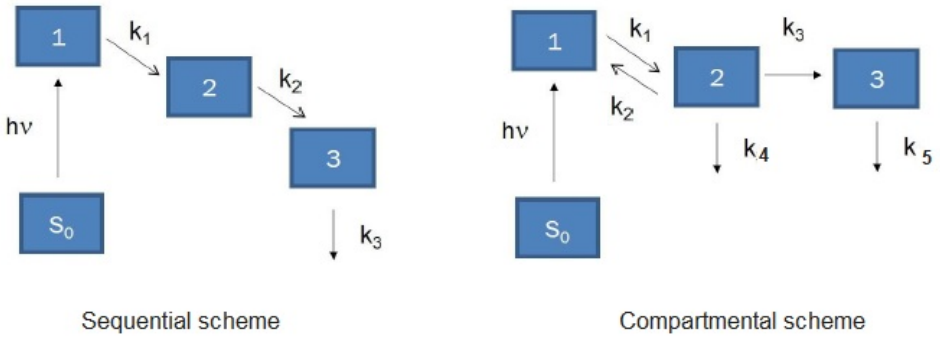

Figure 1.7: Examples of compartmental kinetic schemes for Global and Target analysis.

Once that the number of independent components is defined, as a first approach of fitting, we have to choose a minimum set of values for the kinetics components describing the data. Then, an iterative optimization of the kinetic constants can be made.
The initial values to be included in the fit can be estimated by performing single wavelength fits in the most significant regions of the transient spectrum, that is where the peaks of ground state bleaching or stimulated emission signals appear. Glotaran optimizes iteratively the entered values, until convergence is achieved. After that, depending on the kinetic scheme used it returns the obtained kinetic constants (or their inverse, namely lifetimes) with the related spectral components.
In case a linear decay scheme is applied, the spectral components obtained are called Evolution Associated Difference Spectra (EADS). In the next chapters, these components are reported for all the measurements made and they show the most significant variations occurring in the transient spectrum that can be associated with the time evolution of a molecular system.

Chapter 2

Triplet Photosensitizers

A high absorption in the UV-Visible spectrum and an efficient transition process to excited states with long lifetimes, are very useful properties for the application of organic dyes in innovative research fields.
The energy of a long lifetime excited state can be exploited to catalyze energy transfer processes from an external light source to a system that, alternatively, would not be directly excited. Examples of such energy transfer processes are encountered for instance in the operation of n-type semiconductors inside photovoltaic cells otherwise transparent to part of solar spectrum, or in the generation of oxygen reactive species in the vicinity of cancer cells. In these and other cases, a medium called *photosensitizer* is fundamental to exploit the external light and trigger a specific event.
An ideal photosensitizer should have a series of properties: it should be characterized by an intense absorption of visible/UV light, should efficiently produce long living excited states, should be easy to synthesize and it should have a low cost and low toxicity.
In most cases, the molecules used as photosensitizers can efficiently populate triplet states, so that these systems are classified as *Triplet Photosensitizers*. Applications of these systems can be found in different research areas such as photodynamic therapy, photocatalytic organic reactions and triplet-triplet annihilation up-conversion [5].
Photodynamic therapy is a medical treatment for some types of cancer, precancerous formations, macular infections or degeneration [6]. For the purpose, an organic chromophore is irradiated *in situ* by a radiation which is not harmful for human tissues in order to populate its triplet state. The energy transfer from the sensitizer triplet state to the molecular oxygen can be direct or can occur through a radical intermediate, and it induces the formation of singlet oxygen ($^1O_2$). Singlet oxygen is a cytotoxic agent that can destroy the cells around the specific place irradiated (cancer or damaged cells) (figure 2.1).

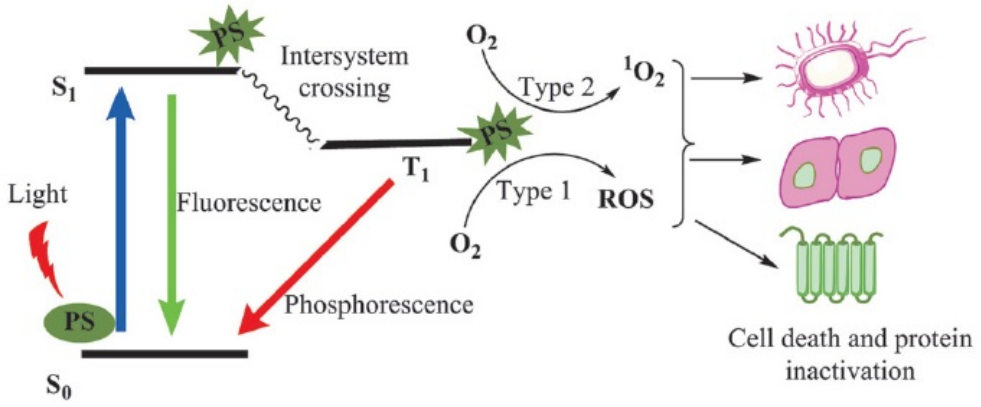

Figure 2.1: Schematic representation of the photochemical processes involved in photodynamic therapy. PS is the photosensitizer, ROS is a reactive oxygen specie [6].

Another major area of application for triplet photosensitizer is organic photocatalysis. In fact, an efficient photocatalyst must absorb in the visible region of the electromagnetic spectrum, has to be easily excited in a stable state and has to remain there for a time long enough to induce electron transfer processes in different substrates [7]. Most of these properties are owned by a good photosensitizer.
Triplet photosensitizers are furthermore used in several optoelectronic devices, exploiting processes such as triplet-triplet annihilation upconversion (TTA) or delayed fluorescence. In case of TTA, an energy transfer process takes place from the triplet state of a donor molecule ($^3ES^*$) to the triplet state of an acceptor molecule ($^3Acceptor$). $^3ES^*$ must be reached with a fast transition and it should have a lifetime above microseconds. This energy transfer is a bimolecular process and it determines the formation of a singlet state with higher energy than that of the donor, resulting in a blue shifted emission (figure 2.2). TTA processes can be used to increase the efficiency of light collectors such as those used in photovoltaic cells [8]. Indeed, through TTA the incident light on the device can be transformed in an emitted light with a lower wavelength, that could have not been otherwise absorbed by the conducting materials of the photovoltaic or photocatalytic cell.

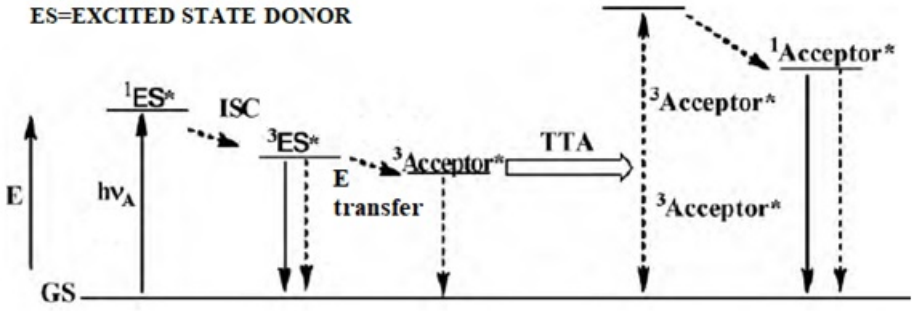

Figure 2.2: Energy level diagram of the upconversion processes between the triplet states of the sensitizer molecule and the triplet acceptor molecule. Solid lines represent radiative processes. GS is ground state, ES is excited state, ISC is intersystem crossing, TTET is triplet–triplet energy transfer, and TTA is triplet–triplet annihilation [9].

Triplet photosensitizers are very promising photoactive materials. Their excited state energy and lifetime are influenced by their specific molecular structure and conformation which can be thus conveniently optimized. In this sense, organic dyes are flexible in their design and synthesis and they could be optimum candidates for the purpose. However, in these simple systems a high population of a stable triplet state is not easily obtained. In fact, the excitation of an organic chromophore generally brings the system in one of its singlet excited states from which transition to triplet states is spin-forbidden.

In the following section, unfavourable old methods and promising new methods to overcome the spin selection rule for increasing the population of the triplet state are presented. Particularly, two specific molecular structural arrangements are theoretically and experimentally (chapter 3) examined.

2.1 Triplet state

Once photoexcited, a molecule can undergo different relaxation processes. After vibrational relaxation, one of the faster relaxation pathways is the transition to a lower energy state of the same spin multiplicity (internal conversion, IC) with overlapped vibrational states (figure 2.3).
The conversion between states that are characterized by different spin multiplicity and by energetic superposition of vibrational modes is called intersystem crossing (ISC).

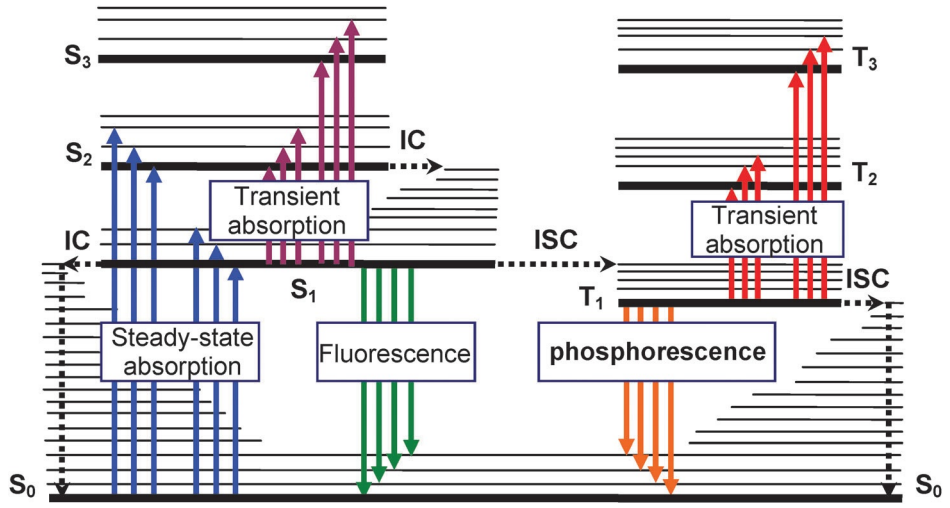

Figure 2.3: Jablonski diagram representing the possible deactivation paths from an excited state. The processes of photoexcitation, radiative and non radiative decay are outlined [5].

A triplet state reached through an ISC process, is an electronic state in which two electrons in different molecular orbitals have parallel spins. For this reason one of the main properties of the triplet electronic density is paramagnetism. Spin variation with respect to singlet states ensures long lifetime of the triplets, generally in the order of microseconds. Triplet emission with relaxation to the ground state is called phosphorescence.
Requiring a total spin change, intersystem crossing is prohibited for spin symmetry and for this reason, it is many orders of magnitude slower than internal conversion. However, in some cases this transition takes place anyway and, if it proceeds, the lifetime characterizing the reached excited triplet state is in range of $10^{-7} - 10^{-11}s$. We talk about ISC also for transition from an excited state to the ground state characterized by different spin multiplicity; in these cases the lifetime of the process is generally less than $10^{-7}s$.
The main interaction determining intersystem crossing is the Spin-Orbit (SO) coupling, representing the coupling between the orbital angular momentum of the electron and its spin angular momentum. In the Hamiltonian describing the interaction between two states with different multiplicity, the SO term is generally small and often neglected. Finding methods to enhance the spin-orbit coupling is a major challenge in photochemistry.
What follows presents different ways of designing systems in which intersystem crossing is favored, at first using the addition of heavy atoms and then developing fully organic triplet photosensitizers which present notable advantages in terms of cost, toxicity and easy synthesis.

Heavy atoms

A first method for enhancing ISC is the introduction of atoms with high atomic number within the structure of the molecule. In fact, an electron moving around a nucleus with a high positive charge is accelerated to relativistic speeds and the coupling between its spin and its orbital angular momentum deeply increases [10]. This behavior appears evident in the dependence of the spin-orbit operator to the

fourth power of the nuclear charge parameter (Z).
However, even though the attachment of a heavy atom to a chromophore greatly increases the ISC yield, it generally leads to a notable decrease of the absorption coefficient of the system. Furthermore, the addition of heavy atoms increases the toxicity of the molecule, a fundamental parameter to be considered for biological applications.

El-Sayed rule

A simple way for increasing ISC is to design chromophores with a low energy singlet state having one electron in a non-bonding orbital (n) and the other in a π^* orbital. This state, classified as (n, π^*) would proceed towards the triplet through a $S_1(n, \pi^*) \rightarrow T_1(\pi, \pi^*)$ transition. This transition respects the conservation of total angular momentum because both the orbital and spin angular momentum change by one unit. The spin-orbit term thus becomes different from zero as well as the transition probability between the two states. This rule is termed as El-Sayed selection rule [11] and even if it appears of easy obtainment, it is not respected in many of the organic chromophores. In fact, in the majority of organic molecules, the singlet state closer in energy to a triplet state is a $S_1(\pi, \pi^*)$ state, making ISC unfavorable.

New methods

Recently, different methods have been developed to enhance the singlet to triplet transition, most of all trying to overcome the limits posed by the use of heavy atoms [5]. Despite common methods, we present different systems where high ISC yields are obtained in simple organic structures, usually containing a donor-acceptor pair. We will focus in particular on two new promising different mechanisms to enhance ISC.
In the first case, a stable radical specie is connected to a chromophore with a high absorbance in the Uv-visible spectrum. The enhancement of intersystem crossing in the presence of a radical is granted by the spin coupling between the two units (RE-ISC).
In the second case, compact donor-acceptor pairs are considered, designed such as the two moieties can adopt an orthogonal orientation. In these systems, a photoinduced electron transfer is followed by charge recombination on a relatively fast timescale (generally on the 1-100 ns timescale). Charge recombination is accompanied by a significant change in the orbital angular momentum of the system, which can be compensated by a variation of the spin angular momentum promoting a spin flip for the production of a triplet state. Because of its characteristics, this mechanism is usually termed as Spin Orbit Charge Transfer-Inter System Crossing (SOCT-ISC).

In the following, we will describe in detail these new two mechanisms and several experimental results will be reported in the next chapter.

2.2 Radical enhanced inter system crossing (RE-ISC)

The first method called Radical enhanced inter system crossing (RE-ISC) is based on the attachment of a stable radical to a chromophoric compound characterized by a high absorption in the Uv-visible spectrum. The spin coupling with the radical determines the enhancement of the efficiency of ISC [12].
The molecular linker between the two moieties affects the strength of their electronic coupling and the spin states of the two species can interact separately *without a complete electronic delocalization* on the entire molecule. For this reason, the two spin states can be considered interacting but at the same time *distinct*.
The interaction between radical and chromophore is designed as *spin-spin exchange interaction* and it is described by the following hamiltonian [13]

$$H_{exch} = JS_RS_C \tag{2.1}$$

J is the coupling constant and it depends on the distance between the spins and on the mechanism through which their orbitals interact; S_R is the quantum number of the spin momentum localized on the Radical, while S_C is the quantum number of the spin momentum localized on the Chromophore. The spin exchange between the moieties stabilizes the total energy of the molecular system and it becomes different from zero when the chromophore turns to a triplet state.
Depending on the overlap between the orbitals of the two interacting species, J can be approximated by the exponential function [14]

$$J(r) \cong J_0 e^{-\alpha(r-d)} \tag{2.2}$$

where r is the inter-radial distance, J_0 is the magnitude of the exchange interaction at distance d of the closest approach and α is a characteristic length factor.
At the ground state of the molecule, the radical species has a spin momentum $S_R = \frac{1}{2}$ (D_0) while the chromophore with no unpaired electrons has a total spin $S_C = 0$ (S_0). Even though the spin multiplicity of the entire system (chromophore+radical) is a doublet (D_0), thanks to the distance between the spins, the system can be described as a $S_0 - D_0$ pair (figure 2.4).

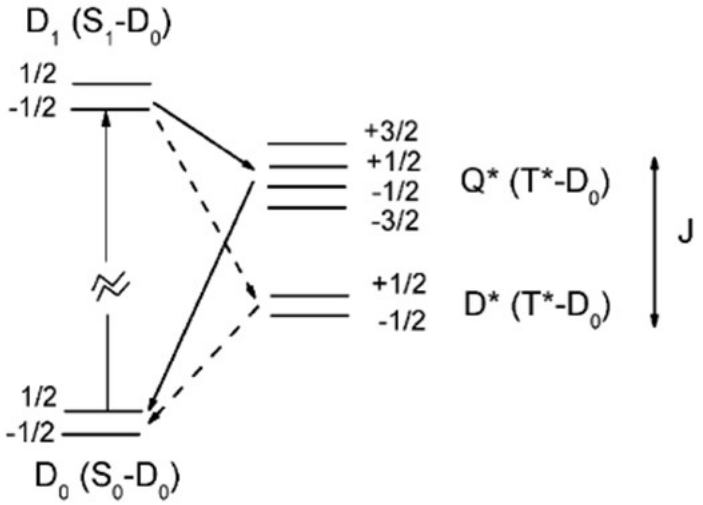

Figure 2.4: Energy diagram describing the photoexcitation and deactivation path of a chromophore linked to a radical species.

Considering the system as a spin pair, its excitation and following deactivation pathway can be described as follow.
After the absorption of the irradiated light, the system is promoted to an excited state of the same multiplicity than the ground state, that is characterized by the chromophore in its excited singlet state ($S_n - D_0$). From this state, inter system crossing is one of the possible ways back to the ground state, but it is generally prohibited, because the transition moment integral between two states with different spin multiplicity is zero (selection rule). However, if a spin-spin exchange interaction between the chromophore and the radical determines the formation of a *localized* triplet state on the chromophore and a localized doublet state on the radical ($T^* - D_0$), ISC becomes permitted.
In fact, considering the whole chromophore-radical pair, the three unpaired spins (one on the chromophore triplet state T^* and two on the radical doublet state D_0) can arrange such as the entire molecule could be both a doublet D^* ($S = \frac{1}{2}$) and a quartet Q^* state ($S = 1$). The transition from the initially populated doublet state ($S_n - D_0$) or globally D_n, and the state ($T^* - D_0$) or D^* is then *spin-allowed*. Therefore, the rate of ISC appears deeply enhanced.
The energy difference between the doublet and the quartet states depends on the J value. When $J > 0$ the spin interaction is classified as antiferromagnetic and the doublet state is at a minor energy; when instead $J < 0$ the interaction is called ferromagnetic and the quartet state appears more stable. The energy difference between the two states is equal to 3J.

2.3 Spin Orbit Charge transfer inter system crossing (SOCT-ISC)

Spin orbit charge transfer inter system crossing is gaining increasing attention as a suitable mechanism to obtain heavy-atom free long lived triplet states with high quantum yield [13] [15] [16].
In order to be efficient, highly compact donor acceptor dyads (D-A) are linked through a short bridge, making them orthogonal to each other. In these systems Photoinduced Electron Transfer (PET), followed by charge recombination occurring on a relatively fast timescale, induces the enhancement of inter system crossing.
Charge recombination is indeed accompanied by a change in the orbital angular momentum which is stabilized by the spin-flip to a triplet state. The angle and the relative molecular orbital orientation between the two moieties of the dyad clearly affect the entity of the orbital angular momentum change.
To better understand this process, it is fundamental to describe the PET interaction between the reactant species and the product species. A complete description of PET process is fully reported in Appendix A and the following limited description must be referred to it.

The reactant species involved in PET is the localized excited state (LE), while the product species is the state formed by the electron transfer and called Charge Separated state (CS). The same PET interaction also takes place from the formed CS state to another excited state ($CS \rightarrow LE$) or from CS to the ground state ($CS \rightarrow GS$): we refer to these processes to as *Back Electron Transfer* (BET).

In each case, the rate constant for electron transfer among a donor and acceptor species depends on different factors following the general relation

$$k_{el} = \nu_n \cdot \kappa_{el} \cdot e^{\frac{\lambda}{4}\left(1+\frac{\Delta G_{el}}{\lambda}\right)/RT} \tag{2.3}$$

Considering the complete description made in Appendix A, in the following paragraph we present a brief discussion of the factors affecting k_{el}. Indeed these factors are fundamental in the treatment of the PET process, but they also determine the specific mechanism inducing the population of the triplet state that only in some cases takes place as SOCT-ISC.

Nuclear reorganization energy λ and driving force ΔG_{el}

The two parameters λ and ΔG_{el} in equation (2.3) are the factors characterizing the region in which electron transfer proceeds (paragraph A.3.1).
ΔG_{el} is the driving force of the process and it is calculated by using experimental redox potentials and taking into account the molecular properties through the Weller equation (A.9). The total reorganization energy λ is the energy required to distort the product state to the equilibrium geometry of the reactant state.
Considering these two factors, PET rate increases with the increasing of the reaction exothermicity, because of the enhancement of the driving force ($|\Delta G_{el}| >>$). However, after a specific point related to λ and called *activationless regime* ($\Delta G_{el} \simeq -\lambda$), this intuitive kinetic trend reverses. Even if the driving force increases, the barrier of the process becomes higher and the rate decreases. This regime is called *inverted region* ($\Delta G_{el} < -\lambda$, figure A.8).

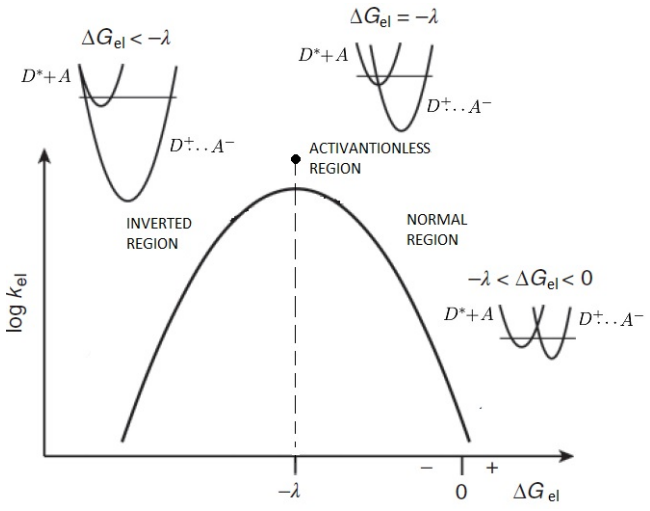

Figure 2.5: Relationship between the electron transfer rate constant and the driving force of a PET process according to Marcus quadratic expression. Each regime has been evidenced by the bell-shape curve and by the insertion of the interactive parabolic potentials of reactant and product states [17].

The distinction between these regions is important because their different trend can be used to enhance the direct photoinduced electron transfer while decreasing the rate of back electron transfer to the ground state.
The optimal region requested to enhance PET is that where no thermal activation

energy is required ($\Delta G_{el} \simeq -\lambda$). However, at the same time, the desired prevention of a fast BET process to the ground state should require that the transition between CS and GS owns to the inverted region. Fortunately, in most cases charge recombination from CS to GS is characterized by an energy difference between reactant and product states so high that the resulting value of ΔG_{el} is lower than $-\lambda$ and the electron transfer process revert its kinetic. Under these optimal conditions, even a low electronic coupling as small as $V \geq 1.7cm^{-1}$ makes it possible to go forward from the reactant to the product state on a (sub)nanosecond time scale [15], producing a CS state living beyond the nanosecond time scale.

Electronic coupling H_{el}

Electronic coupling H_{el} between the interacting moieties is the other important parameter in the description of PET process. It determines two different ranges of conditions (limits) followed by different channels of charge recombination.

1. *Weak limit*
   Typically, the electronic coupling is weak for dyads with high distances between donor an acceptor. In this limit, under non-adiabatic conditions, electron transfer rate is proportional to the square of the electronic matrix that couples the localized excited state (LE, reactants) and the charge separated state (CS, products):

$$k_{el} \simeq \nu_n \cdot \frac{2}{\pi} \langle \Psi_{LE} | \hat{H}_{el} | \Psi_{CS} \rangle^2 \frac{1}{(4\pi\lambda k_B T)^{1/2}} \cdot e^{\frac{\lambda}{4}\left(1+\frac{\Delta G_{el}}{\lambda}\right)/RT} \tag{2.4}$$

   The crossing point between the potential curves of LE and CS is permitted and thermal activation energy is needed to overcome the high energetic barrier for electron transfer (right panel, figure 2.6).

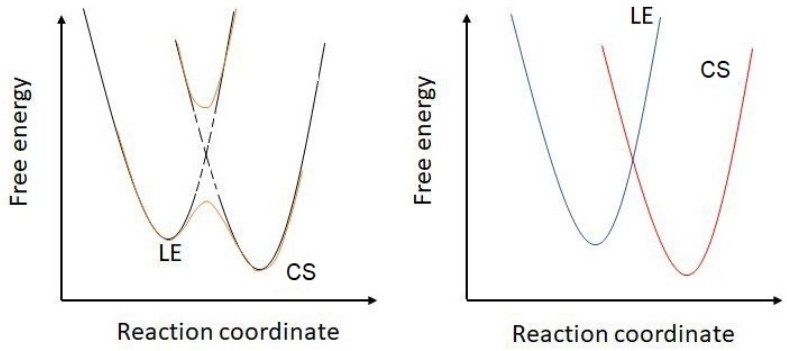

Figure 2.6: Potential energy curves of reagent and product for electron transfer in the adiabatic (left) and non-adiabatic (right) limit [13].

   In this limit the rate of PET is strongly reduced. However, if the system conditions for PET are thermodinamically optimal, as mentioned above, the electron transfer can be anyway reasonably achieved with a rather small value of H_{el} ($1.7cm^{-1}$).

2. *Strong limit*
   Large values of H_{el} identify the adiabatic limit of electron transfer. A strong interaction between donor and acceptor determines a high level of interaction also between product and reagent states.
   The strength of the coupling introduces new terms in the Hamiltonian describing the system. The potential curves obtained by the resolution of that Hamiltonian appear different, with a quasi-continuum from the reactant to the product state and a consequent low energy barrier (left panel figure 2.6). In this case the transition from LE to CS occurs with a continuous change of the reaction coordinate, from a strong localized character to a strong charge transfer character of the electronic state.
   High values of electronic coupling can be generally obtained in compact dyads and they reduce the energy barrier for the $LE \rightarrow CS$ transition. However, at the same time, high values of H_{el} also reduce the energy barrier for BET process with consequent reduction of CS lifetime. The rate of back electron transfer increases proportional to H_{el} and when back electron transfer is favored, it generally induces the decay to the ground state. Moreover, even if a localized triplet state is present near the CS state, inter system crossing is generally not permitted, because the electronic coupling vanishes between states of different multiplicity.

In spite of all these difficulties in both relative weak and strong limit, when the molecule is well designed to increase the stability of the CS state and decrease the BET rate to the ground state, different channels of deactivation populating a triplet state at long time delay can become possible and highly favored.

For donor-acceptor systems with *weak electronic coupling* due to long separation distance (D-M-A), an intermediate triplet CS state $^3(D^{\bullet-}-M-A^{\bullet-})$ is generally present at lower energy, close to the singlet CS state (figure 2.7).

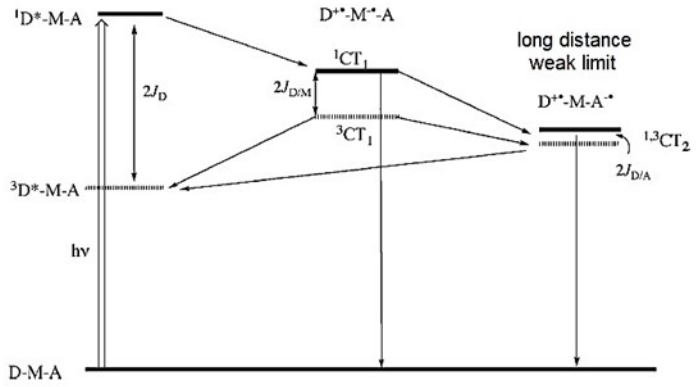

Figure 2.7: Typical energy level diagram of a triad containing two acceptors (M and A) and one donor (D) [15].

The energy difference between these two states is given by the exchange interaction between the two unpaired electrons located at different positions within the dyad ($2J_{D/A}$). The magnitude of the energy gap is thus provided by the J parameter of the electron spin-spin exchange Hamiltonian, that is related to the

spatial overlap of the two electronic wavefunctions. The higher is the distance between the moieties, the smaller is the relative J value ($2J_{D/M} > 2J_{D/A}$).
When the absolute value of 2J is low, the interaction between the electron spin and nuclear spin of both donor and acceptor takes place (hyperfine interaction, HFI) and induces the inter system crossing. In fact, the sum of the HFI of the donor radical anion ($D^{\bullet -}$) and that of the acceptor radical cation ($A^{\bullet +}$) is higher than their electronic coupling (2J) and induces the population of $^3D^{\bullet -}-M-A^{\bullet -}$.
In this case we talk of Radical Pair inter system crossing mechanism (RP-ISC).
Usually, RP-ISC is followed by a spin selective charge recombination with the decay to the lowest localized triplet state of either donor or acceptor subunit (^1LE or $^3D^*-M-A$). The yield of inter system crossing in electron donor-acceptor systems showing RP-ISC mechanism is generally quite low. Furthermore their synthesis is usually very difficult, since it requires the attachment of two moieties at long distances through long molecular bridges.

Compact donor acceptor dyads are easier to prepare, but at low distances the energy gap between the singlet ^1CS and the triplet ^3CS state is significantly higher. In these conditions the RP-ISC mechanism is unlikely and the system is in the regime of *high electronic coupling* [16].
Generally in compact dyads, charge recombination to a lower triplet state is not permitted because of the different multiplicity. Long lifetime triplet states are not easily achieved. However, at the same time charge recombination to the ground state can be delayed designing the molecule in such a way that the CS state is higher in energy and CR occurs under deep inverted region conditions. In this way, the electron transfer kinetic of the direct process proceeds in picoseconds, but the CS state lives beyond microseconds, giving the chance of proceeding to different deactivation channels.
If donor and acceptor are characterized by an orthogonal geometry, the previous electron transfer between orbitals displayed in a perpendicular plain determines a large orbital angular momentum change of the electron, that can be compensated by a following spin flip (figure 2.8).

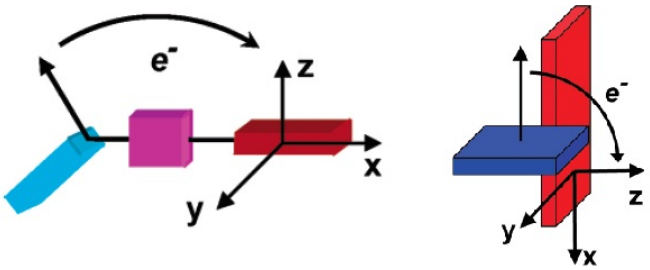

Figure 2.8: Two representations of an electron transfer process between orbitals oriented in the x-z plane and resulting in a large change in the orbital angular momentum along y component [16] [18].

In this way the angular momentum conservation is satisfied and the inter system crossing to ^3LE is strongly enhanced. In the past few years this mechanism has attracted much attention and it has been referred to as spin-orbit charge transfer intersystem crossing (SOCT-ISC).

In figure 2.9 the two ISC mechanisms above mentioned are represented (RP-ISC and SOCT-ISC), with the energetic scheme of the excited states involved.

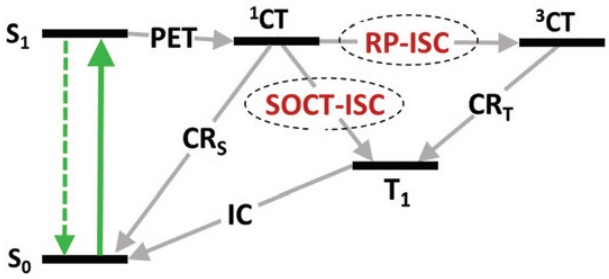

Figure 2.9: Jablonsky diagram showing two possible mechanisms for inducing inter system crossing in donor-acceptor dyads [19].

Spin orbit mechanism is the major process responsible for the formation of triplet states in closely spaced-dyads, most of all in those in which the donor and the acceptor are directly linked through a single C-C bond [19]. In these systems the orthogonal arrangement is due to the steric hindrance between the subunits. If the dihedral angle is less than 70° the probability of SOCT-ISC is strongly reduced together with the triplet sate yield.
However, there are also evidences that the orthogonal geometry between the acceptor and donor is not exclusively sufficient to populate the triplet state, in fact some compact dyads, showing efficient charge separation, display a non efficient inter system crossing [20]. Furthermore, there are even some dyads that have shown efficient SOCT-ISC without an orthogonal geometry but with spectral evidences of this specific type of mechanism [21].
We can conclude that despite the numerous studies performed in this field, the full understanding of the governing principles of this process is still in progress.

In our laboratories, we have analyzed various systems where SOCT-ISC promotes high triplet quantum yields ([22] [23] [24] [25] [26]). In the following we will present in detail a few examples of these studies.

Chapter 3

Characterization of long-lived triplet states in Donor Acceptor systems

This chapter presents the experimental spectroscopic characterization of several donor-acceptor dyads which can undergo efficient triplet formation through different mechanisms. Samples have been synthesized by the Photochemistry and Photophysics group of the Dalian University of Technology led by Professor J. Zhao.
The analyzed systems exploit two different mechanisms for enhancing triplet formation. In the first case, a radical species has been connected to a chromophore with a high absorbance in the UV-visible spectrum to promote triplet formation through RE-ISC. In the second type of systems, donor-acceptor pairs of chromophores were orthogonally linked to undergo an efficient intersystem crossing through the previously described SOCT-ISC mechanism.

3.1 RE-ISC

In our laboratories we have studied with transient absorption spectroscopy three different systems designed for Radical Enhanced intersystem crossing. Before presenting the analysis of one of these triplet photosensitizers, we want to describe some parameters considered in designing these types of promising molecular systems.
Both the choice of the chromophore and that of the molecular linker connecting the radical, are fundamental factors in the design of efficient triplet photosensitizers. The distance and the orientation between the two moieties deeply affects their spin-spin interaction, together with the consequent formation of doublet and quartet states [27].

Chromophore

Chromophores generally used to design promising triplet photosensitizers are characterized by strong absorption in the Visible spectral range and high fluorescence. However, when the triplet state is produced by the interaction between a stable radical spin and the lowest excited singlet state of the chromophore (RE-ISC), the latter can even lack high fluorescence and intrinsic inter system crossing abil-

ity [28].
Only a limited number of chromophores have been used to induce the specific radical enhanced inter system crossing process, for instance naphthalene [29], naphthalendiimidde [30], anthracene [31], pyrene [32], bodipy [33] and perylene [34].
The systems that we have studied are characterized by the presence of *naphthalendiimide*, *perylene* and *pyrene* as chromophores, showing high absorbance in the UV-visible spectral range and high fluorescence or ISC ability.
The aromatic molecule naphthalendiimide is one of the molecules used for RE-ISC with the strongest absorption of visible light. Its absorbance wavelength can be modulated by linking substituents on specific aromatic core positions without reducing its extinction coefficient. Moreover, other important properties of this core are high electron-acceptor character and high fluorescent quantum yield.
Pyrene and perylene moieties attached to different radicals have been also frequently used to study photoinduced intramolecular spin exchange through π-conjugation [32] [28]. Both these chromophores are robust organic dyes, they are easily functionalized and photochemically stable. For this reason they generate significant interest as photoactive materials in a wide variety of photonics applications.

Radical

In all of the three molecules provided by the photochemical group of professor Zhao, the radical inducing a spin exchange with the triplet state of the excited chromophore is the oxoverdazyl radical (figure 3.1).

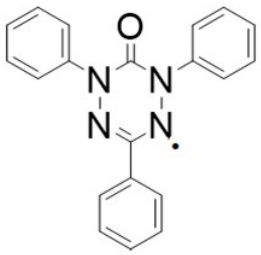

Figure 3.1: Structure of the Oxoverdazyl radical.

This radical has been already used for the study of photoinduced spin coupling in different paramagnetic systems and it has demonstrated high stability [32] [30] .

Molecular linker

The molecular linker is another important parameter influencing the efficiency of the photosensitizer. As we have already said, it determines the strength of the spin coupling in the radical-chromophore pair. In previous studies different linkers have been tested to examine both the weak and strong coupling regime.
The weak electron spin-spin exchange interaction is the most studied situation and it is usually observed for systems where the radical and chromophore are mechanically mixed or covalently linked through *saturated* bonds. When radical-triplet complexes are generated by physical encounter through mechanical mixing,

the quartet to doublet energy splitting is due to the through-space exchange interaction usually showing negative sign [27]. In the case of exchange through σ bonds, J depends on the direct overlap between orbitals of unpaired electrons and on spin polarization [35]. The addiction of π-conjugation between radical and chromophore determines a major delocalization of the electron density, increasing the spin-spin interaction.
Alterations of distance and orientation of the radical relative to the chromophore are other important parameters that change the magnitude of the electronic coupling.
The work of E. Giacobbe et all. on three different compounds of PDI (perylene-3,4:9,10-bisdicarboximide) differently attached to a tert-butylphenyl-nitroxide radical shows that the electron exchange interaction determines the overall intersystem crossing rate and it depends directly on the entity of the electronic overlap between the excited state localized on the chromophore and the singly occupied molecular orbital of the radical. In fact, a *nearer* spin density of the radical places enough π spin density within the carbon attached and produces a sufficient electronic coupling that drives ultrafast RE-ISC.
However, the results of one of our previous studies [30] show that the sample with a *longer* distance between the chromophore and the radical appears to be more efficient in the enhancement of intersystem crossing, following a faster triplet formation. This behavior has been associated with the fact that the longer linker with the triple bond enhances the rigidity of the structure and forces the planarity of the molecule. For this reason, even if the radical and the chromophore are more distant, the orbital overlap between them is higher, as well as their spin-spin exchange interaction.
With the purpose of improving the design of triplet photosensitizers, different systems have been synthesized. As an example of the study made on Radical Enhanced Inter System Crossing method, in the following section we report the characterization of a family of compounds with perylene as chromophore linked to the oxoverdazyl radical.

3.1.1 Photophysical properties of Perylene-Oxoverdazyl dyes

The results reported in this section are based on the publication on ChemPhysChem 2020, with authors Imran M., Taddei M., Sukhanov A. A., Bussotti L., Ni W., Foggi P., Gurzadyan G. G., Zhao J., Di Donato M. and Voronkova V. K. [36].

Three systems have been prepared with different connections between the two moieties: Pery-Vz-1 characterized by a direct connection, Pery-Vz-2 and Pery-Vz-3 with two different orientations of an additional phenyl ring between radical and chromophore (figure 3.2).

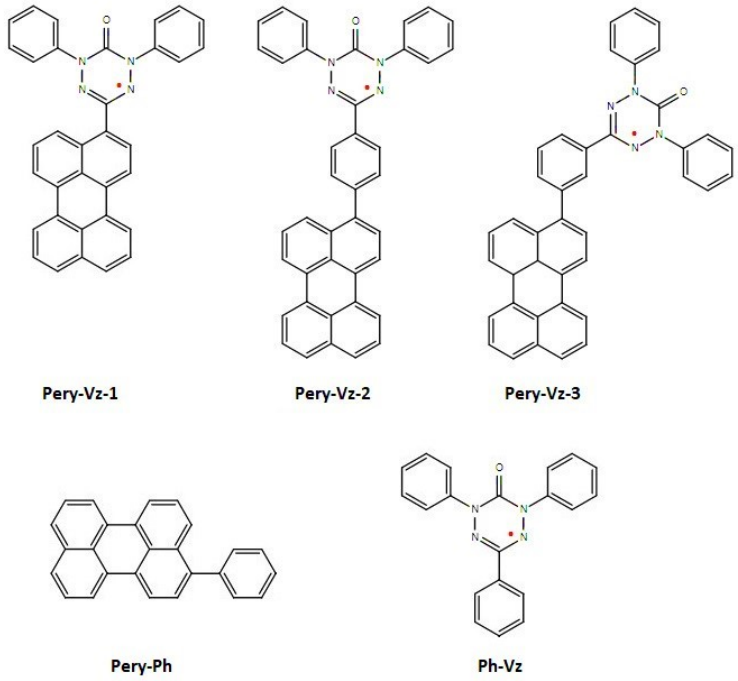

Figure 3.2: Perylene-oxoverdazyl radical dyads with different spacers. The two references compounds Pery-Ph and Ph-Vz are shown in the bottom

Steady-state characterization

UV-Visible absorption spectra and fluorescence emission spectra of the three Perylene-Oxoverdazyle samples together with the two references 3-phenyl perylene and phenyl Oxoverdazyle (figure 3.3) have been acquired in toluene.
Figure 3.3 reports the absorption spectra of the samples, each compared with the spectra of the two references.

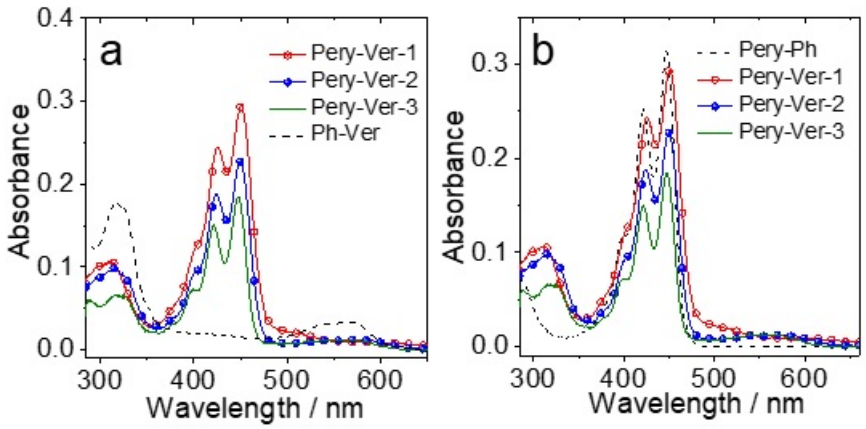

Figure 3.3: UV-Visible absorption spectra of (a) Pery-Ver-1, Pery-Ver-2, Pery-Ver-3 and Ph-Ver; (b) Pery-Ph, Pery-Ver-1, Pery-Ver-2 and Pery-Ver-3 in toluene.

Each compound shows the characteristic absorption band of perylene, presenting a strong vibronic progression and assigned to its $\pi - \pi^*$ transition. This

band is centered at 451 nm and it does not present any big shift for the different molecules. The reference compound Ph-Vz is characterized by two peaks centered at 320 and 567 nm. These same two bands can be observed for all the samples but with a decreased intensity, probably because of the presence, at the ground state, of a limited interaction between the radical and the chromophore. In the case of Pery-Vz-1 sample, the perylene absorption band shows a broad tail in the red region that could suggest the presence of a stronger interaction between the two moieties.
The reduction of perylene fluorescence quantum yield following the attachment of the radical indicates that the two moieties interact in the excited state. Indeed, pristine perylene owns a fluorescence quantum yield of 94% with an emission band centered at 445 nm. In Pery-Vz-1 this band is almost completely quenched (figure 3.4) and similar results are obtained for all the other samples.

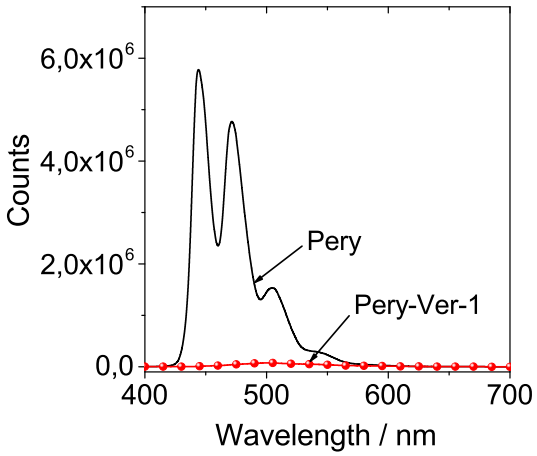

Figure 3.4: Fluorescence emission spectra in optically matched solution of Pery and Pery-Ver-1 in toluene, with an excitation wavelength of 390 nm.

The transition to the triplet state is favored by the spin-spin exchange interaction and it removes population from the fluorescent excited state of the molecule. However, it is not the only process that can determine the fluorescence quenching of perylene. Other processes that can compete with the radical influence are Förster energy transfer (FRET) or photoinduced electron transfer (PET).
The energy transfer process between radical and chromophore depends on the overlap between the fluorescence band of the donor moiety (perylene) and the absorption band of the acceptor (verdazyle). In this case, this overlap is not optimal and the extinction coefficient of the radical is very small; for these reasons the FRET quenching mechanism is expected to be not very fast nor efficient.
One indication against PET comes from the measurements of fluorescence in different solvents, showing that emission is quenched also in low polar solvents. Indeed PET proceeds through the population of a charge transfer state, whose energy is strongly influenced by the polarity of the solvent. The lack of solvent dependence is however not definitive evidence for ruling out electron transfer, since the process could be diffusion controlled [38]. For this reason cyclic voltammograms of the radical-containing compounds have been measured. The redox potentials obtained have been used to calculate the free energy changes for the

intramolecular electron transfer process. The values of ΔG result negative even in non-polar solvents (tab 3.1) and for this reason, a charge transfer process can not be completely excluded. Transient absorption measurements appears fundamental to untangle the presence of a possible transient charge transfer state.

Compound	E_{ox} (V)	E_{red} (V)	ΔG_{CS}		
			HEX	TOL	DCM
Pery-Vz-1	+0.49, +0.64	-1.04	-0.15	-0.47	-1.31
Pery-Vz-2	+0.48,+0.58	-1.04	-0.11	-0.44	-1.32
Pery-Vz-3	+0.49	-1.04	-0.16	-0.48	-1.35
Pery-Ph	+0.57	-	-	-	-

Table 3.1: Electrochemical redox potential and driving forces of charge separation ΔG_{CS}.

The photophisical properties of all the samples are reported in the following table.

Compound	λ_{abs} (nm)	λ_{em} (nm)	$\Phi_f(\%)$	$\tau_f(ns)$	$\Phi_\Delta(\%)$
Pery-Vz-1	451/500	510	0.91	4.5	5
Pery-Vz-2	449/570	474	1.25	2.8	7
Pery-Vz-3	447/570	464	1.58	3.8	/
Pery-Ph	447	462	90	4.0	/

Table 3.2: Spectroscopic properties of compounds in toluene solution;Φ_f is the fluorescence quantum yields with perylene as standard (F = 94 %, n-hexane), τ_f is the fluorescence lifetimes in DCM and $\Phi_\Delta(\%)$ is the singlet oxygen quantum yield with $Ru(bpy)_3[PF6]_2$ as standard ($\Phi_\Delta(\%)$ = 0.57 in DCM) in n-hexane; $\Phi_\Delta(\%)$ of Pery-Vz-3 and Pery-Ph was not observed.

Triplet quantum yields were not directly measured, but the values obtained with the singlet oxygen method ($\Phi_\Delta(\%)$) and the intensities of the transient absorption spectra recorded at long time delays (nanosecond) can give an an estimate of the triplet state population.

Transient spectroscopy

In order to investigate the possibility of ISC and its dynamics, all samples have been studied with femtosecond transient absorption spectroscopy (TAS). All the measurements have been performed in deaerated toluene with excitation wavelength at 400 nm. Transient spectra of Pery-Vz-1 are shown in panel a) of figure 3.5.

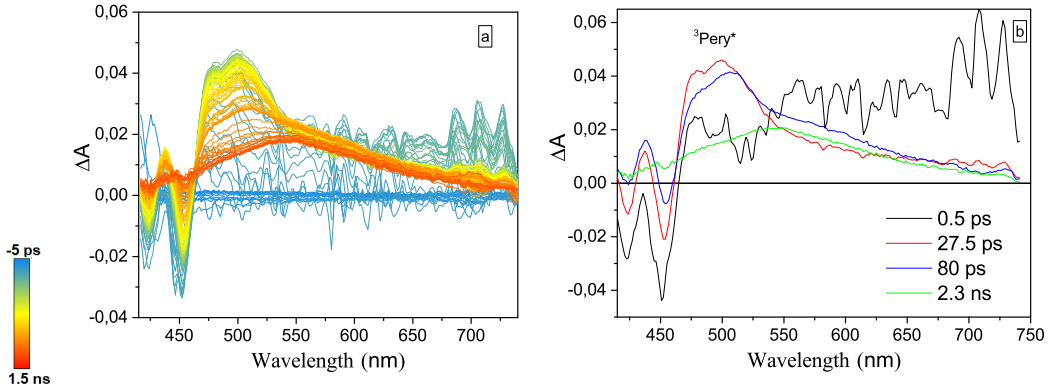

Figure 3.5: Transient spectra (a) and Evolution Associated Difference Spectra (b) of Pery-Vz-1 in toluene. Excitation at 400 nm.

The color code in panel a refers to the time interval of the measurement, from -5 ps (blue spectra) to 1.5 ns (red spectra) after excitation. At early positive times delays, a negative signal with two peaks at 425 and 450 nm is visible. Considered its characteristic band shape, that is the same of the absorption band of perylene moiety (figure 3.3 panel b dotted line), this band is clearly assignable to the ground state bleaching of the molecule (GSB). At the same time, a broad positive signal (ESA) centered at 700 nm is detected, which can be assigned to the transient absorption S_1 to S_n, localized on perylene moiety. After few hundred of femtoseconds (0.5 ps) this band decays and another ESA band rises covering the interval from 480 nm to 600 nm, with maximum intensity around 500 nm. This positive band highly resembles the band previously assigned to perylene triplet state $^3Pery^*$ [34]. At longer pump-probe delays the ESA band shape evolves, becoming a broad band centered at 550 nm.
This spectral evolution is better evidenced by the extrapolated Evolution Associated Difference Spectra, obtained by performing a global analysis of the kinetic traces, and reported in panel b of figure 3.5.
The first black trace can be assigned to the state reached upon excitation, which corresponds to the first excited singlet state of perylene. After 0.5 ps, the spectrum evolves towards the red component, assigned as the triplet state of the perylene moiety. A very small part of population will remain in the singlet excited state, and decay by emitting fluorescence in the nanosecond time interval (Φ_f=0.91%, τ_f=4.5 ns 3.5). The intensity of this spectrum slightly decreases after 27 ps with the rising of a little shoulder at 550 nm (blue EADS). The presence of this shoulder could be associated to the early contribution of a long living spectral component that totally develops in 80 ps (evolution from blue to green line). The final green spectrum presents an ESA broader and red shifted with respect to the band assigned to the triplet state of perylene.
However, the green component can also be assigned to a triplet state because of its long lifetime. In fact, this band well corresponds to that detected with nanosecond transient absorption spectroscopy by Professor Zhao and reported in Figure 3.6. From these ns measurements, a triplet state lifetime of 9.5 μs has been estimated.

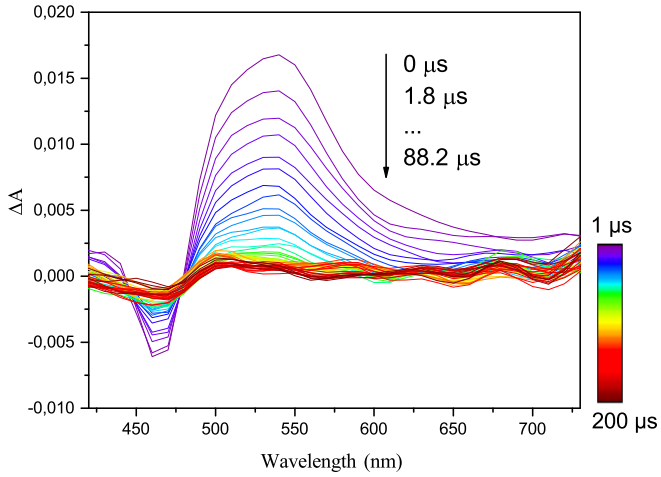

Figure 3.6: Nanoseconds transient spectra of Pery-Vz-1 in toluene, excitation at 400 nm.

The blue and green EADS in panel b of figure 3.5 have been so associated to triplet states, although their spectral shape is not the same. The reason for this difference could arise from a possible interconversion and equilibration among two different triplet states. In fact, assuming spin-spin exchange interaction between the radical and the chromophore, both the formation of D_1 and Q_1 states is envisaged.
In both these two states, perylene is in its triplet state, but if D_1 and Q_1 present a different spin density distribution all over the dyad, the transient absorption spectrum associated with each of them could be different. In the quartet state a stronger interaction between the two moieties could bring to a delocalization of the spin density on the entire molecule, causing its band broadening and red-shifting. A proof for this explanation comes from the DFT calculations of the spin density of the compound. The spin density surface of the Pery-Vz-1 quartet state has been analyzed, showing that it is indeed localized on the entire molecule (figure 3.7).

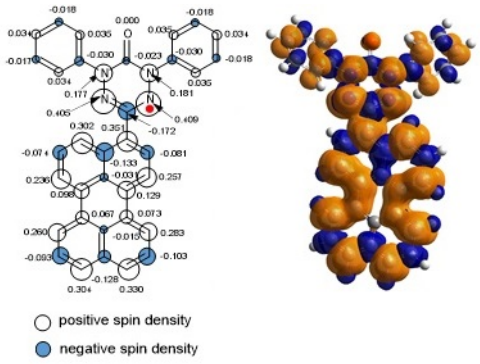

Figure 3.7: Spin density distribution of Pery-Vz-1 lowest optimized quartet excited state (Q_1) obtained by UB3LYP/6-31G (d) level using Gaussian 09W.

Accounting to these results, the evolution observed from the blue to the green

EADS has been assigned to the interconversion between D_1 and Q_1 states, where in D_1 the triplet state is more localized on the perylene moiety, while in Q_1 the spin density is spread much more all over the all system.
The spectrum assigned to Q_1 of Pery-Vz-1 lives beyond the final pump-probe delay accessed with ultrafast pump-probe (1.5 ns) and, according to nanosecond transient spectroscopy, it decays within 9.5 μs.
DFT computations also find out the energy levels of the excited doublet and quartet states. The calculated energies show that the spin-spin interaction between the doublet state of the verdazyl radical and the triplet state of perylene is ferromagnetic, that is with J>0. The quartet state is found at minor energy than the doublet state and the calculated J value is 0.05 eV.

Electronic transition	Excitation energy	Oscillator strength
$D_0 \rightarrow D_1$	1.66 eV	0.0000
$D_0 \rightarrow Q_1$	1.50 eV	0.0062
$D_0 \rightarrow D_3$	2.66 eV	0.7449

Table 3.3: Excitation energies and oscillator strength values measured with TDDFT/UB3LYP/6-31G (d) and Optimized Ground State Geometry.

According to calculations, the absorption at 445 nm can be associated to the $D_0 \rightarrow D_3$ transition. The internal conversion towards D_2 is too fast to be detected through femtosecond transient spectroscopy.
All the information collected on this system allow to depict an energy diagram scheme that clarifies the deactivation pathway of Pery-Vz1 following excitation at 400 nm (figure 3.8).

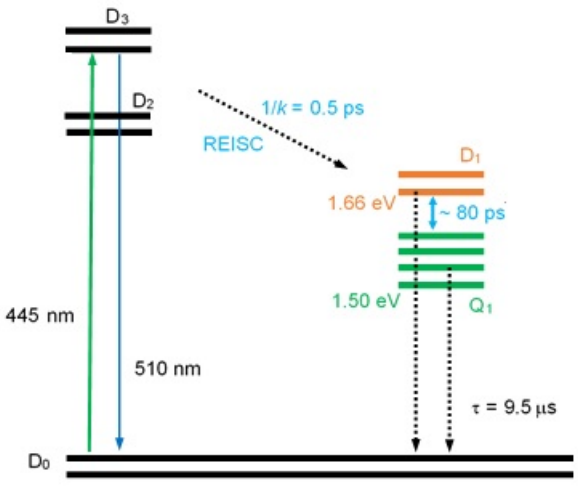

Figure 3.8: Energy level scheme for the deactivation processes of Pery-Vz1

As retrieved from the analysis of the ultrafast transient absorption spectra, ISC takes place on a very fast timescale of 0.5 ps. The interconversion between D_1 and Q_1 takes place in 27/80 ps and the final decay towards the ground state occurs in 9.5 μs The decay from the D_1 state to the ground state is spin allowed

and expected to be faster than that from the quartet.
The singlet oxygen quantum yield measured for this compound is very low (5%), most probably because of the short lifetime of D_1 which is rapidly quenched after Radical Enhanced Internal Conversion (REIC) because of its same spin multiplicity as the ground state. Furthermore, the analysis of the EADS clearly shows that there is no evidence for the involvement of charge transfer states. For this reason the PET quenching mechanism is strongly unlikely.
The results obtained for Pery-Vz-1 can be compared with those of the other compounds reported in figure 3.9.

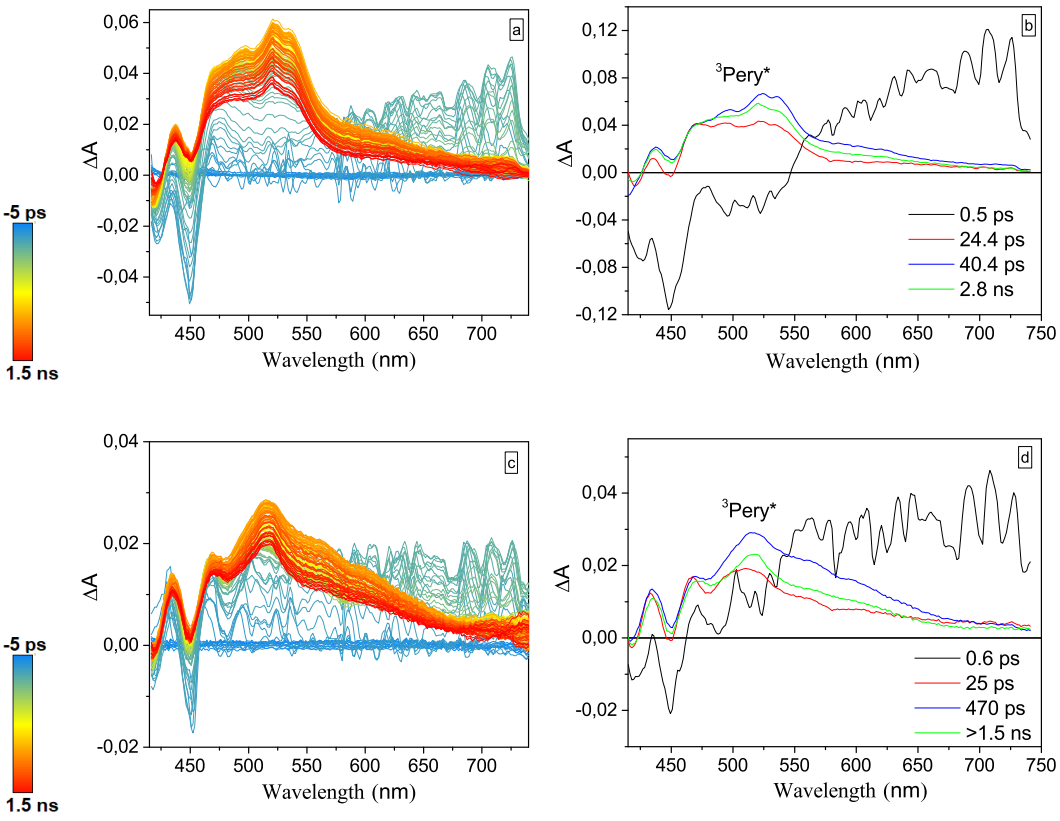

Figure 3.9: Transient spectra and Evolution Associated Difference Spectra of Pery-Vz-2 (panel a and b) and Pery-Vz-3 (panel c and d) in toluene. Excitation at 400 nm.

Transient spectra of Pery-Vz-2 are reported in panel a of figure 3.9, while the relative EADS are reported in panel b. Similarly to Pery-Vz-1, at early times, the transient signal (black trace in panel b) is characterized by the perylene GSB contribution at 450 nm and its intense ESA band at 700 nm. After nearly 0.5 ps, the signal evolves to the red trace that can be assigned to the triplet state localized on the perylene chromophore and reached through RE-ISC. The resulting triplet ESA band appears quite broad, extending from 430 nm to 550 nm. Within 24 ps the intensity of the ESA band changes (blue trace), with a rise in its red part, possibly associated with a biphasic intersystem crossing process. After 40 ps the intensity of the ESA band slightly decreases. The final spectral component lives beyond the time interval of the measurement (>1.5 ns). With respect to the

previous sample, the similarity between the final spectra recorded with ultrafast pump-probe and those spectra obtained with nanosecond transient spectroscopy is even more evident. The higher planarity given by the π-conjugation with the phenyl spacer improves the spin exchange interaction, increasing the electronic delocalization on the entire molecule.
The nanosecond study on this sample also extrapolates the lifetime of the triplet state. Differently from Pery-Vz-1, in this case the kinetic trace at 540 nm shows a bi-exponential decay that can be assigned to the population decay from the doublet state (1.6 μs) and the quartet state (7.8 μs).
The results obtained for Pery-Vz-3 are quite similar to those of Pery-Vz-2, accounting the only structural difference of the radical attachment on the phenyl ring spacer. The transient spectra are reported in panel c of figure 3.9, while the EADS are reported in panel d. Also in this case the GSB band at 450 nm and the ESA band at 700 nm are clearly distinguishable. The ISC takes place on a similar timescale as in previous samples (0.6 ps). Triplet state signal then undergoes to an evolution after 25 ps. Also in this case ISC appears to be a biphasic process. On the following 470 ps, the intensity of the triplet signal partially decreases. The last spectral component lives beyond 1.5 ns.

Conclusions

Three radical-containing compounds have been fully characterized using different techniques, such as transient absorption spectroscopy, cyclic voltammetry, nanosecond transient spectroscopy and DFT calculations. Pery-Vz-2 and Pery-Vz-3 differ from Pery-Vz-1 for a different distance between radical and chromophore because of the presence of a phenyl spacer.
The results demonstrate that in all the three compounds REISC takes place on a very fast timescale of 0.5-0.6 ps. The triplet state of Pery-Vz-1 has a long lifetime (9.5 μs), pretty much higher than other previously reported perylene-radical photosensitizers [34]. However, its low triplet quantum yield suggests the necessity of specific structural changes for practical applications. Nearly the same results have been obtained for the other two samples even if the higher degree of π conjugation between radical and chromophore contributes to a higher planarity of the structure.

3.2 SOCT-ISC

Spin Orbit Charge Transfer mechanism has been studied and characterized by different researchers. From all these studies the property of orthogonality seemed to be a fundamental but not an essential condition for the mechanism. Furthermore, orthogonal geometry between acceptor and donor seems also not to be exclusively sufficient to efficiently populate the triplet state [20].
Certainly, to favor triplet formation long-living charge separated states are very useful. In fact, as we have already said, when the rate of back electron transfer to the ground state is substantially decreased, alternative charge recombination processes are observed, such as recombination to the triplet excited state. There is no clear definition for the long-lived charge separated state: CT states with lifetime longer than a few dozens of ns are often reported, while CT states with lifetime longer than microseconds are very rare.
For this reason, all the molecules studied in this thesis were designed trying to induce the formation of very long living CT state from which a Spin Orbit charge recombination could take place [15]. As already mentioned, this property can be achieved by designing *compact* dyads and making use of their inverted region, or in designing *long distance* donor acceptor systems and making use of the consequent weak electronic coupling between the moieties.

Molecular systems

In most of the studies, the designed molecule is a simple donor-acceptor system where a direct single-step electron transfer forms a long lived CT state. Usually, strong electron donors such as phenothiazine, perylene or anthracene have been linked to visible light harvesting chromophores such as bodipy and perylenemonoimide. For many of these systems, very high triplet state yields (>90%) and long triplet lifetime (up to a few hundreds of microseconds) have been observed [19].
The design of distant donor acceptor systems (D-M-A) generally determines the enhancement of the ISC process through the RP-ISC mechanism instead of SOCT. However, in our work we report the detection of a SOCT-ISC mechanism in an electron donor-donor-acceptor triad, from its last CT state to a localized triplet state, induced by an orthogonal geometry. In this case, it has been possible to study the influence of a *sequential* electron transfer process on the efficiency of the SOCT mechanism.

In the following, we will show the time dependent spectroscopic characterization of two molecular systems undergoing efficient SOCT-ISC. The former is a common donor-acceptor system with a single step electron transfer and an outstanding long lived CT state detected; the latter is a D-M-A triad characterized by a sequential electron transfer process and an efficient ISC.

3.2.1 Photophysical properties of compact spiro Rhodamine Naphthalimide dyes

This section is based on the publication on Angewandte Chemie International Edition 2020, authors D. Liu, A. M. El-Zohry, M. Taddei, C. Matt, L. Bussotti, Z. Wang, J. Zhao, O. F. Mohammed, M. Di Donato, S. Weber [25].

Two compact bichromophoric systems composed by a donor-acceptor couple with Rhodamine B as donor and Naphtalimide as acceptor were prepared and studied with different techniques (figure 3.10). The use of a novel, fully rigid spiro compact dyad induces an orthogonal orientation and a rigid connection.

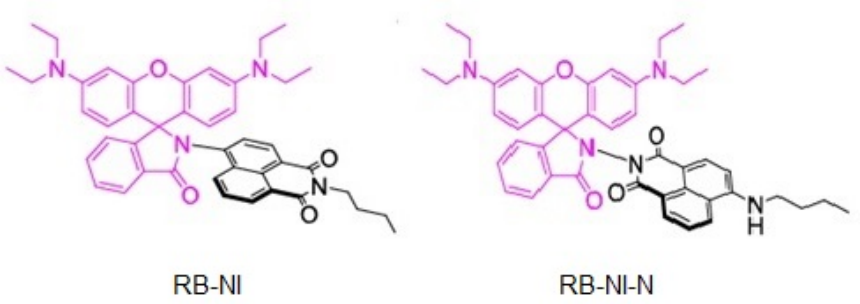

Figure 3.10: Molecular structures of the two RB-NI and RB-Ni-N compounds.

In the RB-NI sample, the acceptor is linked to the donor in the 4-amino position of the naphtalimide moiety. The high constrained conformation and the reduced π-conjugation between the two components determine a very low degree of ground state interaction among the two moieties. RB-NI-N is characterized by the attachment of the two moieties in the amide-position of NI, determining a higher π-conjugation. The localized triplet state of the molecule is expected at a lower energy of the charge separated state.
In both cases, the rigid linker is very short, which deeply enhances the J coupling between the moieties, but reduces the reorganizational energy λ associated to the PET process (for theory see appendix A). In this way the RP-ISC from ^1CS to ^3CS is not favored because of the high energy difference between the two states. The probability of a SOCT-ISC instead rises, following the transition $^1CS \rightarrow ^3 LE$.
Furthermore, the chosen chromophore (Naphthalimide) has no intrinsic ISC ability but the orthogonality of the novel fully rigid spiro compact D-A dyad is expected to induce triplet state population through SOCT-ISC mechanism.
The structures of the two samples were determined through X-ray diffraction on single crystals, and the dihedral angles between the two moieties were calculated as 70.8° in RB-IN and 66.7° in RB-NI-N (figure 3.11).

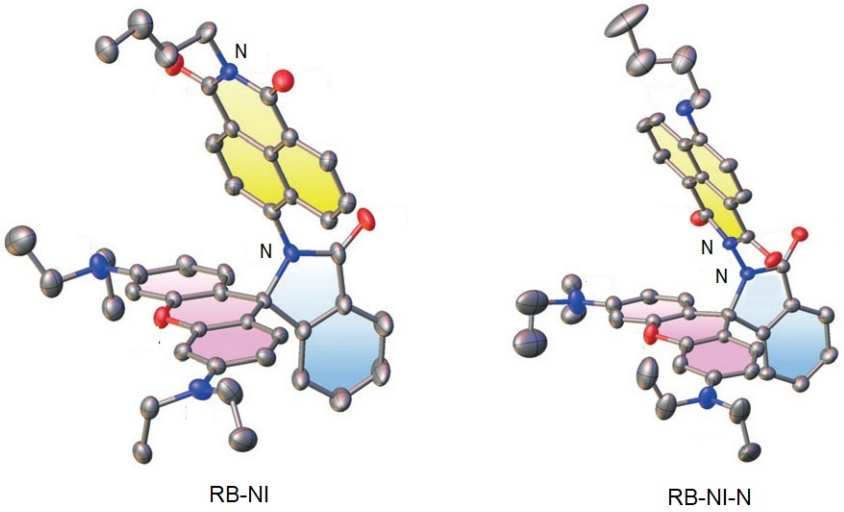

Figure 3.11: Molecular structures of rhodamine–naphthalimide compounds determined with single-crystal X-ray diffraction.

Spectroscopic and electrochemical properties

The Uv-visible absorption and emission spectra of the samples, together with those of the two single moieties (NI-NH and RB-Ph) as references, were recorded in hexane (figure 3.12).

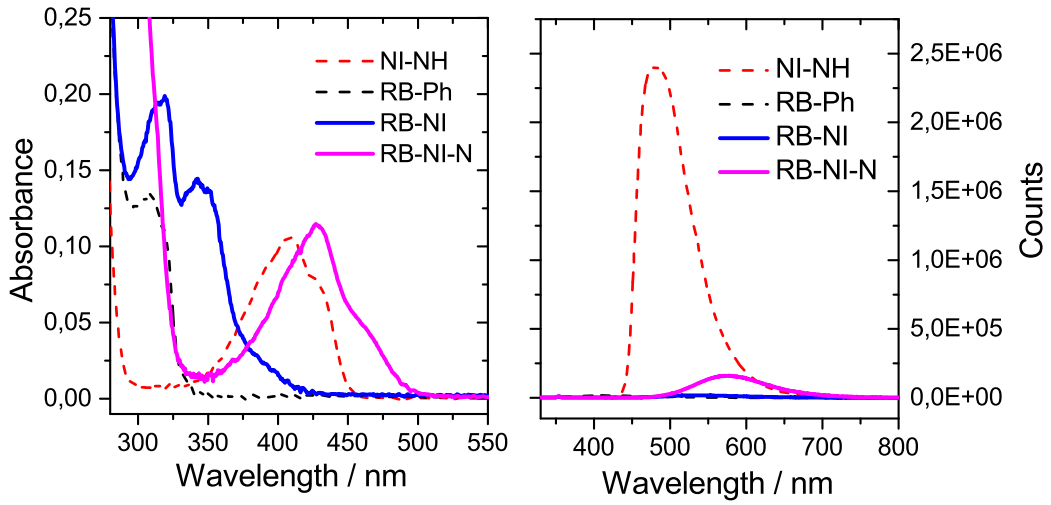

Figure 3.12: UV-visible absorption spectra of the studied compounds in n-hexane.

The absorption band of RB-NI is peaked at 342 nm and it appears clearly blue-shifted with respect to the reference NI-NH (408 nm) and the compound RB-NI-N (427 nm). This shift is probably due to the reduction of electron density on the N atom in the 4-position, related to the orthogonal geometry of the molecule and the consequent decrease of π-conjugation between the moieties. The evidence of a less constricted molecular structure of the sample RB-NI-N can be found in the redshift of its absorption spectrum with respect to the reference NI-NH, indicating a higher conjugation between the two moieties.

With a higher effect on RB-NI, in both samples the characteristic fluorescence emission of naphthalimide (red dashed line figure 3.12 right panel) is strongly quenched (blue and magenta straight line). The sample RB-NI-N shows a weak emission band centered at 578 nm, assigned to its charge transfer state. The presence of this band is due to the high value of the electronic coupling between donor and acceptor moieties.
Fluorescence quenching is a first evidence for a possible photoinduced electron transfer. To support this hypothesis, electrochemical measurements were performed, resulting in negative values for PET driving force ΔG_{CS} in all the solvents (tab 3.4).

Compound	E_{ox} (V)	E_{red} (V)	ΔG_{CS} (eV)	
			HEX	ACN
RB-NI	+0.60	-1.82	-0.85	-1.00
RB-NI-N	+0.52	-2.05	-0.06	-0.27

Table 3.4: Electrochemical redox potential and driving forces for charge separation ΔG_{CS}.

All the photophysical parameters of the samples are reported in the following table. Phosphorescence spectra of the dyads together with the measurements of phosphorescence lifetimes ($\tau_P(ms)$) were also recorded, enhanced by the introduction of iodoethane inducing heavy atom effect. Fluorescence quantum yields ($\Phi_F(\%)$) appear highly reduced compared with that of NI-NH. Singlet oxygen quantum yields ($\Phi_\Delta(\%)$) were furthermore determined, showing a relatively high production of triplet state in both samples.

Compound	λ_A (nm)	λ_F (nm)	$\Phi_\Delta(\%)$	$\Phi_F(\%)$	$\tau_F(ns)$	$\lambda_P(nm)$	$\tau_P(ms)$
NI-NH	408	480	/	67.5	7.5	490	20.3
RB-NI	319/342	545	29.8	1.2	15.7	556/604	20.0
RB-NI-N	427	578	24.5	1.2	15.7	606	36.3

Table 3.5: Photophysical parameters of NI-NH, RB-NI and RB-NI-N in hexane.

Transient Absorption Spectroscopy

Femtosecond transient spectroscopy was performed to study the samples for time intervals from -5 ps to 1.5 ns and with excitation wavelength centered at 400 nm. The acquired kinetic traces were analyzed with global analysis, using a linear decay scheme. Evolution Associated Difference Spectra are reported together with the time constants relative to the excited states evolution. The transient spectra measured for RB-NI in hexane panel a and acetonitrile panel b are reported in figure 3.13, together with the respective EADS (panels c and d).

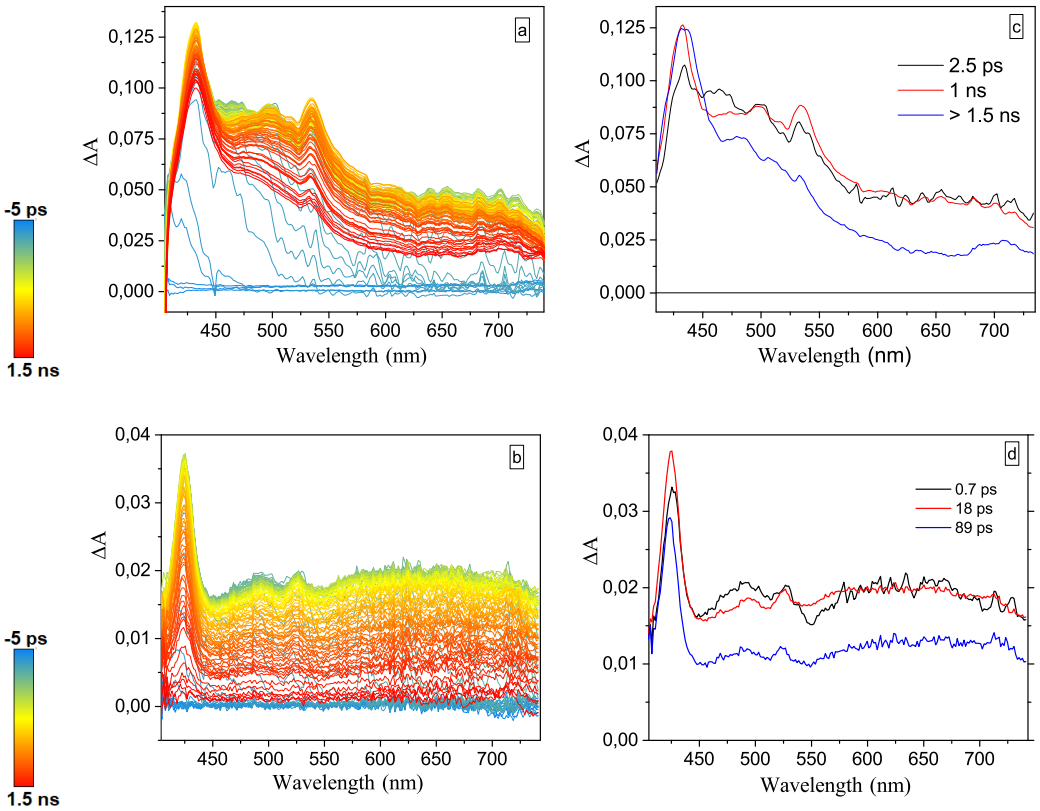

Figure 3.13: Transient absorption spectra recorded for RB-NI in hexane (a) and acetonitrile (b), excitation wavelength at 400 nm. The respective EADS are reported in panels c) and d)

Transient spectra of RB-NI in hexane are characterized by a broad ESA band covering all the spectral range. The comparison with the transient absorption spectra measured for the reference compound NI-NH allows assigning the signal observed in the 600 to 700 nm region to the contribution of the singlet excited state $^1NI^*$ localized on naphtalimide moiety (data reported in the Supporting Information at the end of this section, figure 3.20).
Looking at the EADS reported in panel c, we observe two narrow bands peaked at 425 and 500 nm rising within 2.5 ps (evolution from black to red trace). The peak at lower wavelength can be assigned to the transient radical anion $NI^{-\cdot}$ while that at higher wavelengths to the cation $RB^{+\cdot}$. This attribution is based on spectroelectrochemical measurements performed on Rb-NI (figure 3.21 in Supporting Information) and it confirms the occurrence of electron transfer within few picoseconds.
In acetonitrile, the peak at 425 nm is observed immediately after excitation, suggesting that charge separation is extremely fast occurring within the time resolution of the measurement. Differently from results in hexane, the CS state signal decays to zero before the longest pump-probe delay accessed within the measurement. No triplet state was recorded in this solvent.
In hexane, the two peaks at 425 and 500 nm are characterized by a similar slow decay and they are also observed in sub-nanosecond transient spectra (black trace left panel figure 3.14), as a further demonstration of the PET process

$^1NI^* \rightarrow ^1 CT$.

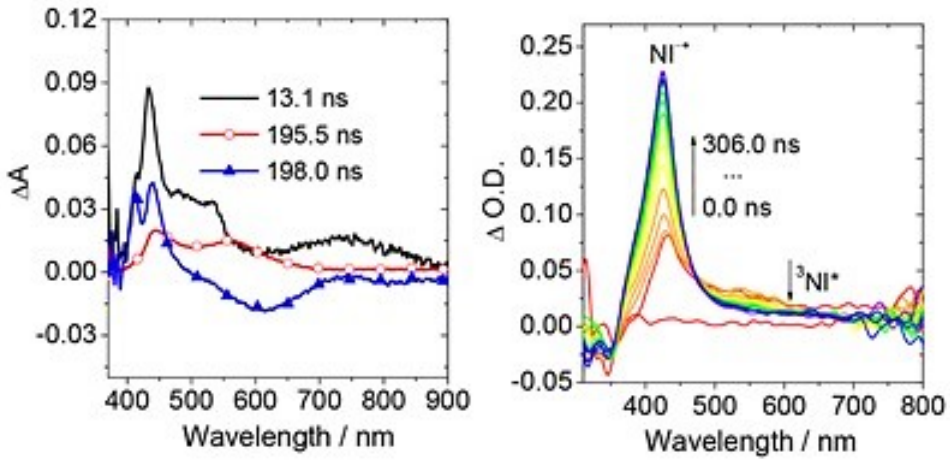

Figure 3.14: Left panel: SADS obtained from the analysis of sub-nanosecond transient absorption spectra acquired for RB-NI in hexane, excitation wavelength at 350 nm. Right panel: nanosecond transient spectra of RB-NI in hexane.

The Species Associated Difference Spectra (SADS) reported in the left panel of figure 3.14 were obtained performing a target analysis on the sub-ns TA spectra. The first extrapolated species (black line) is very similar to the final EADS obtained from ultrafast measurements (blue line in figure 3.13). The peaks clearly associated with the anion/cation species start to decay after 13.5 ns. The ^1CT state decay is accompanied by the formation of two new absorption bands peaked at 447 and 570 nm (red line in the left panel of figure 3.14). This new spectral shape can be assigned to the triplet state, localized on naphtalimmide moiety ($^3NI^*$) [39]. The final blue component rises in 195.5 ns. It is characterized by a positive peak at 425 nm and by a negative signal at 600 nm, that can be attributed to the emission of a charge transfer state. For this reason, this spectrum is assigned to the ^3CT state. The spectral shape of the final SADS of Rb-NI is similar to that of the initial SADS obtained from nanosecond measurements. This signal, which rises in hundreds of nanoseconds, is extraordinary long living as shown in right panel of figure 3.15: a lifetime of 0.94 μs has been measured in deaerated hexane.

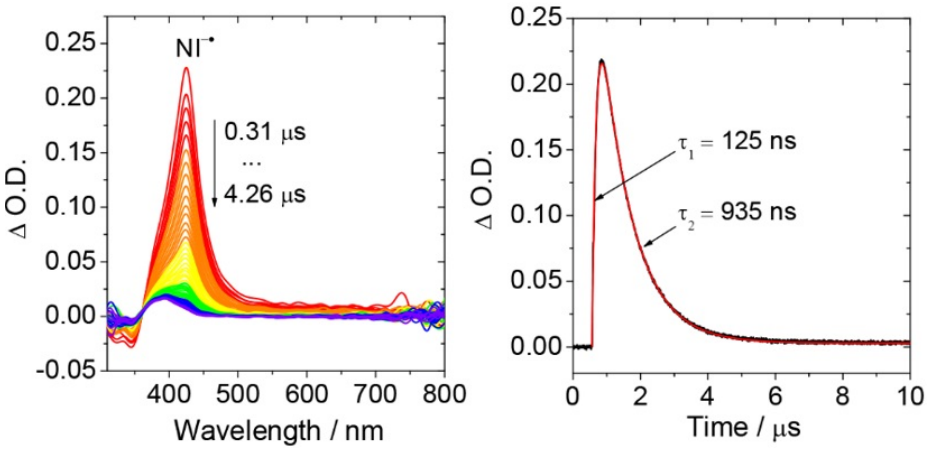

Figure 3.15: Nanosecond transient absorption spectra of RB-NI measured in hexane, excitation wavelength at 350 nm. The right panel reports the kinetic 425 nm together with its fit.

The right panel of figure 3.15 shows also that the kinetic trace at 425 nm measured with ns-transient absorption spectroscopy, which rises within 125 ns. This rising component can be ascribed to a charge separation process that populates the ^3CT excited state. The electron transfer from the singlet to the triplet state is very slow, and only few other examples of charge transfer states are reported presenting such a long lifetime [40].
For the deactivation of RB-NI, the energy diagram of the excited states (figure 3.16) can be constructed based on all the results obtained through transient absorption measurements and performed on different timescales.

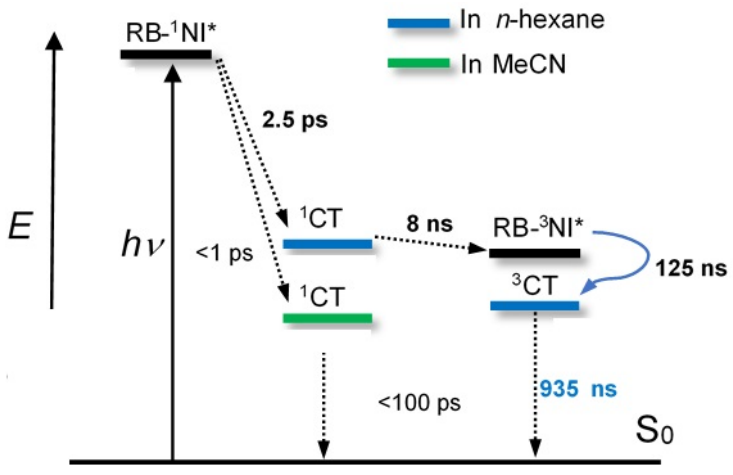

Figure 3.16: Simplified Jablonski diagram illustrating the photophysical processes involved in RB-NI.

In the following figure, the ultrafast transient spectra of RB-NI-N in toluene are reported (figure 3.17).

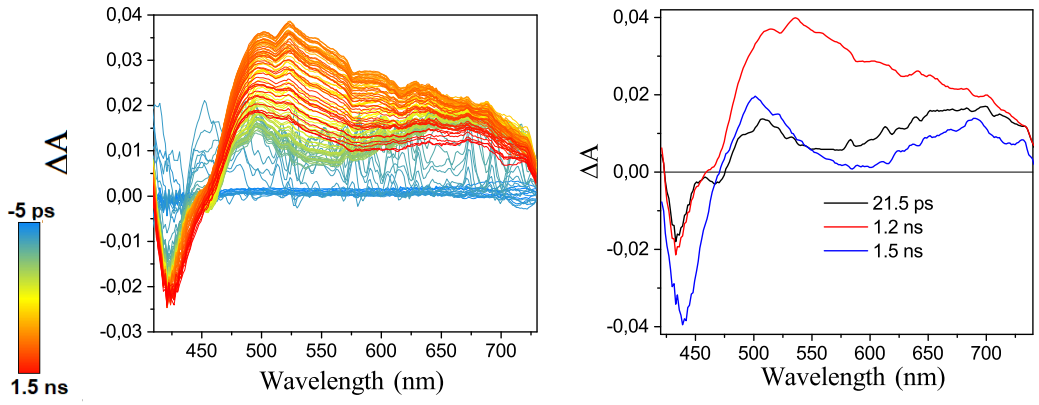

Figure 3.17: Transient absorption spectra and relative EADS recorded for RB-NI-N in toluene, excitation wavelength at 400 nm.

Transient spectra show the presence of the ground state bleaching band of RN-NI-N at 430 nm (GSB), clearly visible due to the red-shifted static absorption of this system. Furthermore, a broad excited state absorption band is observed peaked at about 530 nm. The initial EADS obtained from global analysis (black trace in the right panel of figure 3.17) presents two positive bands at 430-530 nm and 550-700 nm, near the bleaching band. The band in the redder part of the spectrum is very similar to that recorded for NI-NH (data reported in Supporting Information) and also visible in RB-NI. This similarity suggests that the first black EADS represents the transient absorption spectrum of the singlet state localized on the naphtalimmide moiety.
After 21.5 ps, an intense broader band rises around 530 nm (red trace), signaling a transition to a different state. Since $RB^{+\cdot}$ band is expected in this range of wavelengths (spectroelectrochemical measurements in SI), this new state can be interpreted in terms of a ^1CT state whose radical anion contribution ($NI^{-\cdot}$) is probably compensated and covered by the GSB negative band. At long pump-probe delays (1.2 ns), a double peaked spectral shape is observed (blue trace), similar to that observed at short pump-probe delays. Comparing this spectral shape to further time resolved measurements performed on a longer nanosecond timescale, it can be assigned to the triplet state localized on the NI moiety $^3NI^*$ [39].
Figure 3.18 reports the nanosecond transient absorption results recorded in hexane. An intensification of the band peaked at 450 nm is clearly visible, which suggests the following rapid transition from $^3NI^*$ to ^3CT. The final charge transfer triplet state in hexane has a lifetime of 50.5 μs.

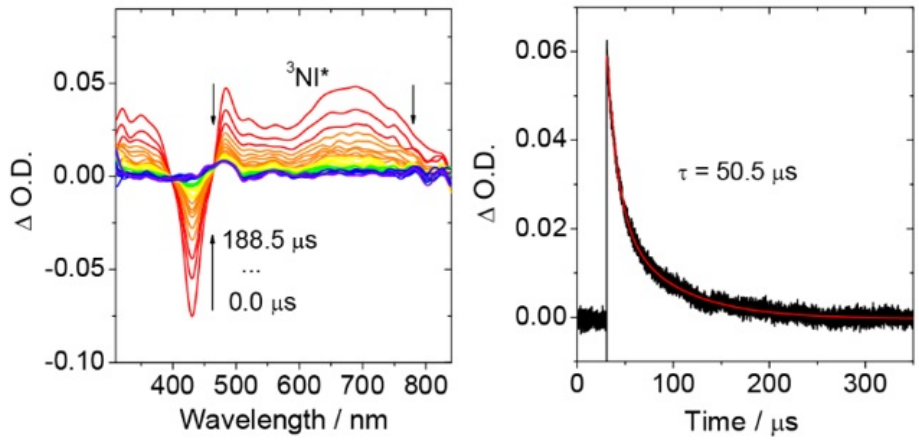

Figure 3.18: Nanosecond transient absorption spectra (right) and kinetic trace at 485 nm in deaerated n-hexane.

The simplified Jablonski diagram represented in figure 3.19 illustrates the photophysical processes occurring for RB-NI-N.

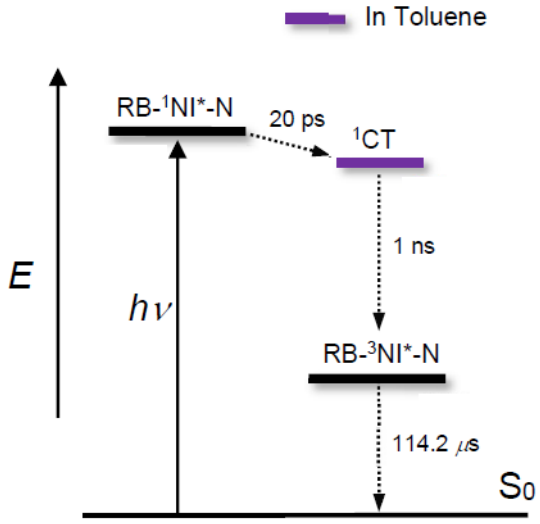

Figure 3.19: Simplified Jablonski diagram illustrating the photophysical processes involved in RB-NI-N.

Conclusions

Two compact spiro Rhodamine-Naphthalimide dyads undergoing efficient photoinduced charge separation were characterized with different techniques. The two samples differ in the linking among the two moieties.
The sample where electron donor and acceptor are separated by three $\sigma-$bonds (RB-NI) shows a deactivation pathway proceeding as $^1NI^* \rightarrow ^1CT \rightarrow ^3NI^* \rightarrow ^3CT$. The first electron transfer is very fast (2.5 ps) and it is followed by ISC with charge recombination occurring in 8 ns. The final state is a CT triplet state populated upon electron transfer from the localized $^3NI^*$ towards the rhodamine moiety. This state is extraordinary long lived, presenting a 0.94 μs lifetime in

deaerated hexane. The obtained results are highly unexpected, since long living triplet charge transfer states were previously never observed in simple compact D-A dyads without heavy atoms or with chromophores owning intrinsic ISC ability. This simple and innovative way of designing dyads to obtain long living CT states is not only useful in the field of triplet photosensitizers, but it introduces new perspectives for designing molecular structures that, since their simplicity, are relevant for all the applications.

Supporting information

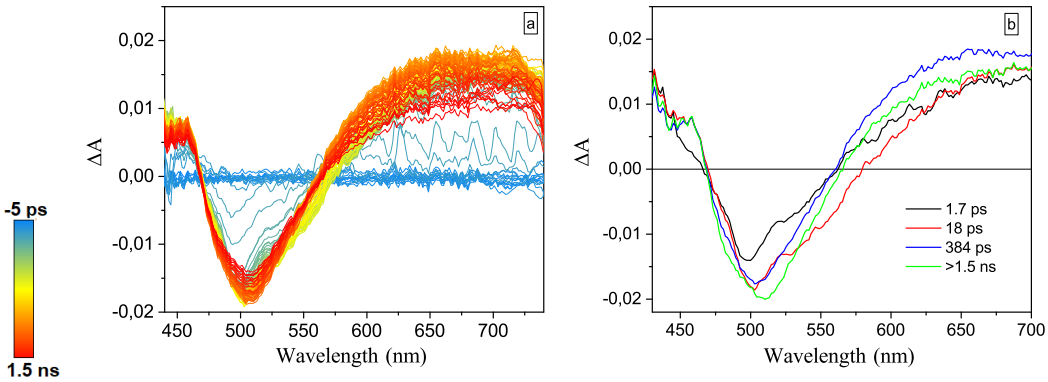

Figure 3.20: Transient absorption spectra recorded for NI-NH in toluene (a) and relative EADS extrapolated from data (b). Color code from blue to red covering the time interval from -5 ps to 1.5 ns.

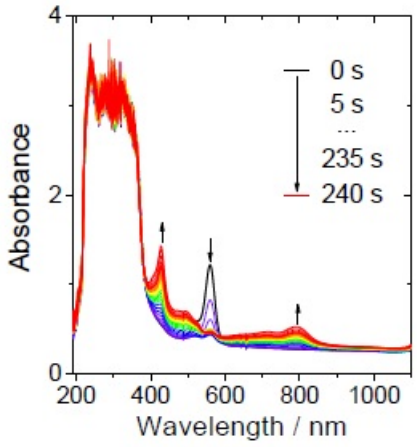

Figure 3.21: UV-Vis absorption spectra of NI radical anion of RB-NI, measured with spectroelectrochemical method in deaerated DCM.

3.2.2 Photophysical properties of compact Carbazole-Anthracene-Bodipy triads

This section is based on the publication on the Journal of Physical Chemistry 2020, authors Zafar Mahmood, Maria Taddei, Noreen Rehmat, Laura Bussotti, Sandra Doria, Qinglin Guan, Shaomin Ji, Jianzhang Zhao, Mariangela Di Donato, Yanping Huo, and Yong Heng Xing [26]

In this section, we present the characterization of two electron donor-donor-acceptor triads where a *sequential* electron transfer takes place between the border moieties. Donor and acceptor species with an appropriate electronic strength has been used to design the triads. Antracene, Carbazole and Bodipy are the three chromophores linked such as to be perpendicular to each other, to enhance the variation of orbital angular momentum promoting intersystem crossing. Carbazole is a typical electron-donating aryl moiety and the BDP-Antracene dyad was already studied as triplet photosensitizer showing strong absorption of visible light, efficient triplet-state formation (quantum yield 90%), and a long-lived triplet state (85 μs) [41].
Distance, relative orientation and position of carbazole moiety have been varied to study the effect of different structural changes on the triplet state quantum yield as well as on the efficiency of the charge transfer. The structures of the analyzed compounds are reported in figure 3.22.

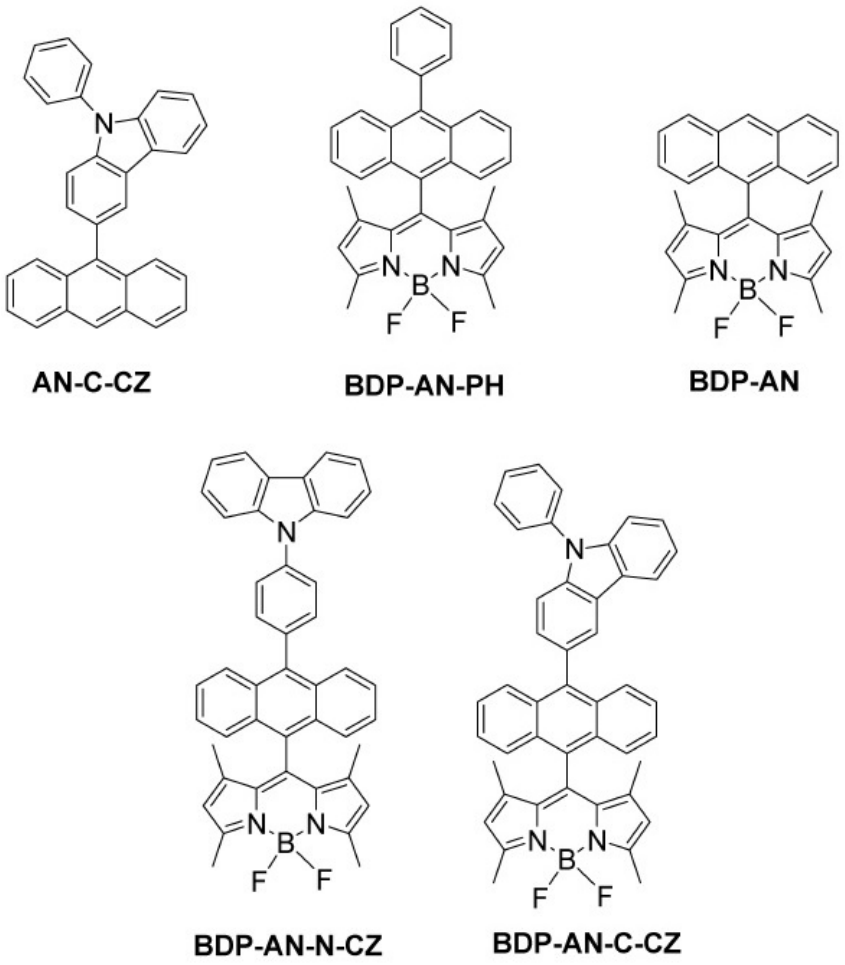

Figure 3.22: Molecular structures of the two Carbazole-anthracene-bodipy compounds and the three references dyads.

All the samples have been analyzed with different static and time-resolved spectroscopic techniques.

Steady-state characterization

Absorption and emission spectra of compounds are analyzed in comparison with those of the reference dyes and are reported in figure 3.23.

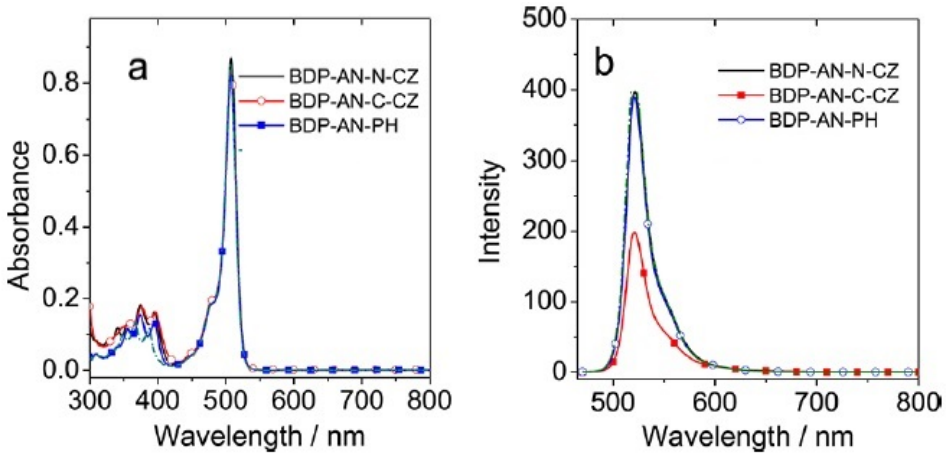

Figure 3.23: a) Uv-visible absorption spectra of the studied compounds in toluene; b) Fluorescence spectra of the compounds in toluene upon excitation at 465 nm.

The absorption spectra are all characterized by an intense band peaked at 500 nm assigned to the absorption of the bodipy moiety and by a small band peaked at 380 nm associated with anthracene. These two bands are not affected by the interaction between the moieties, suggesting that the donor (anthracene) and acceptor (bodipy) weakly interact at the ground state. The fluorescence spectra of all the samples are also very similar, showing only one emission band centered at nearly 520 nm, attributed to the locally excited state emission of the bodipy moiety. The fluorescence of the triads is strongly quenched compared to that of an isolated bodipy, suggesting the possible occurrence of photoinduced electron and/or energy transfer processes.
Fluorescence has been measured in solvents with different polarity. In dichloromethane, a charge transfer band appears in the fluorescence spectra of the triads, peaked around 600 nm. This band is particularly intense for BDP-AN-C-CZ, see figure 3.24.

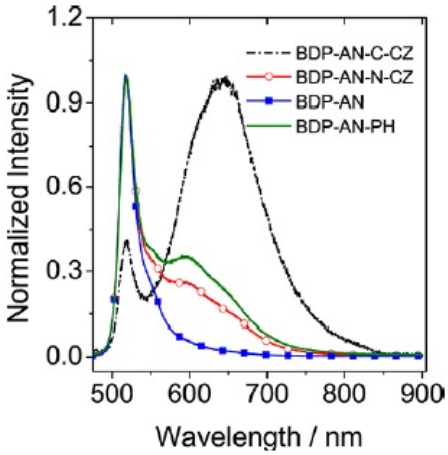

Figure 3.24: Fluorescence spectra of the studied compounds in dichloromethane, upon excitation at 465 nm.

In contrast with BDP-AN-C-CZ, looking at the fluorescence behavior of BDP-

AN-N-CZ, it appears that in polar solvents the local excited band is still more intense than the charge transfer band. This observation suggests that the electronic coupling in BDP-AN-N-CZ is lower than BDP-AN-C-CZ. The reason can be found in the presence of the added phenyl ring as spacer between anthracene and carbazole.

Transient Absorption Spectroscopy

Femtosecond and nanosecond transient absorption spectroscopies were used to characterize the electron transfer steps proceeding in samples, together with the possible spin orbit charge transfer process that populates the triplet state.
Transient absorption spectra with sub-ps time resolution were recorded in the -5 ps-1.5 ns time interval. The samples were excited at 400 nm where the anthracene moiety absorbs. All the recorded transient spectra were analyzed using global analysis to extract the time constants of the photoinduced processes through a multiexponential fit at each wavelength. This fit also retrieves the spectral components representing the evolution of the transient signal (EADS).
Femtosecond transient spectra of the two triads studied in dichloromethane are reported in figure 3.25, with data of BDP-AN-C-CZ in panel a and BDP-AN-N-CZ in panel c.

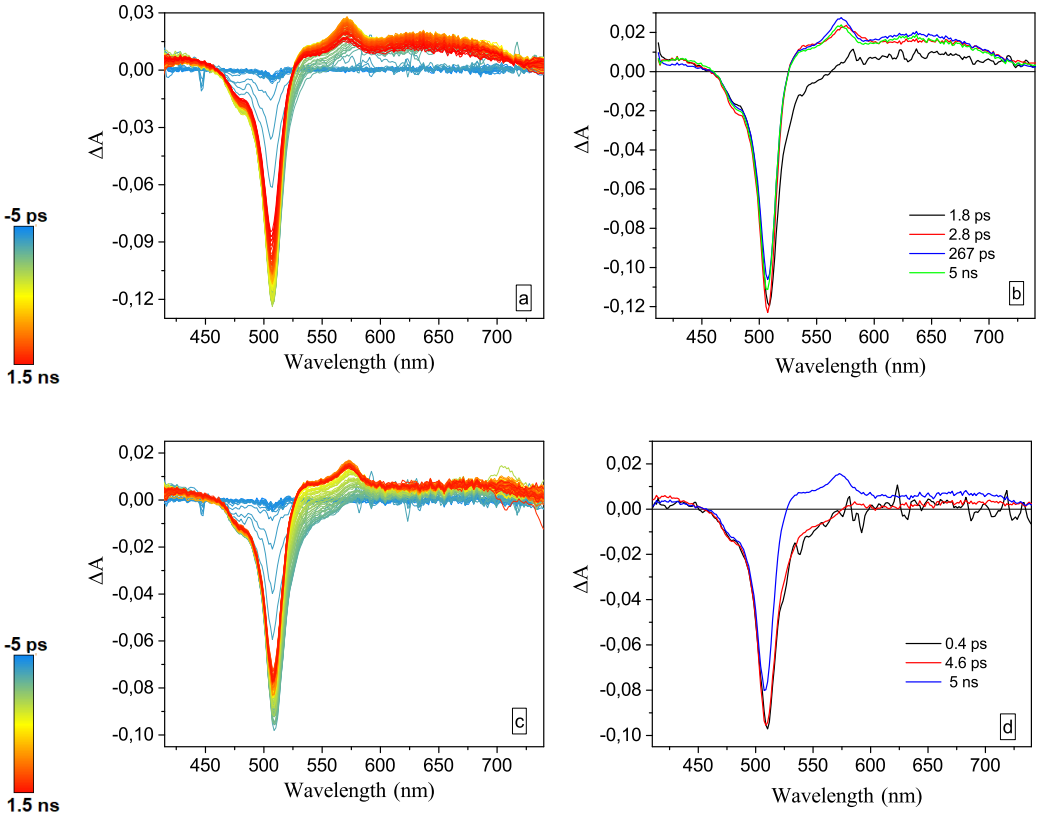

Figure 3.25: Transient absorption spectra recorded for BDP-AN-C-CZ (a) in dichloromethane and relative Evolution associated difference spectra (b), and BDP-AN-N-CZ (c) in dichloromethane with relative EADS (d).

From the transient spectra of BDP-AN-C-CZ (panel a), the global analysis

performed extracted four spectral components (panel b). The initial spectral component (black line) reveals an intense negative bleaching band peaked at 510 nm and clearly assignable to the BDP moiety. Moreover, it shows a broad positive band extending from 550 to 700 nm that however is not completely resolved at the short timescale. In this region the positive signal of BDP anion and AN cation are expected, according to the assignment made in previous literature [42] [43]. The band assigned to the BDP anion is peaked at 580 nm and it is observed to rise after 1.8 ps (red EADS). In the following evolution occurring in 2.8 ps (from red to blue), a broad band at 640 nm develops. The spectral changes observed can be associated with a second photoinduced electron transfer step, from the initial $BDP^{\cdot -} - AN^{\cdot +} - CZ$ radical pair to the following $BDP^{\cdot -} - AN - CZ^{\cdot +}$. In fact, the increase in intensity at 540 nm and the rising signal at 640 nm are attributable to the absorption of the carbazole radical cation [44]. Finally, on the longer timescale, the signal appears slightly to decrease in intensity, with part of the population that remains in the excited state.
Despite the different linker between the carbazole unit and the anthracene, the transient spectra and evolution of BDP-AN-N-CZ (panel c and EADS in panel d) are very similar to those described above. The intensity of the signals and the time scales are slightly different, with the signal assigned to the BDP radical anion rising in 4.6 ps (evolution from the red to the blue spectral component in panel d). The comparison between the two samples indicates that charge separation seems to be faster and possibly more efficient in the BDP-AN-C-CZ triad.
Charge transfer processes take place also in nonpolar solvents, even if with slower kinetics. Data acquired in toluene are reported in figure 3.26, with BDP-AN-C-CZ in panel a and BDP-AN-N-CZ in panel c.

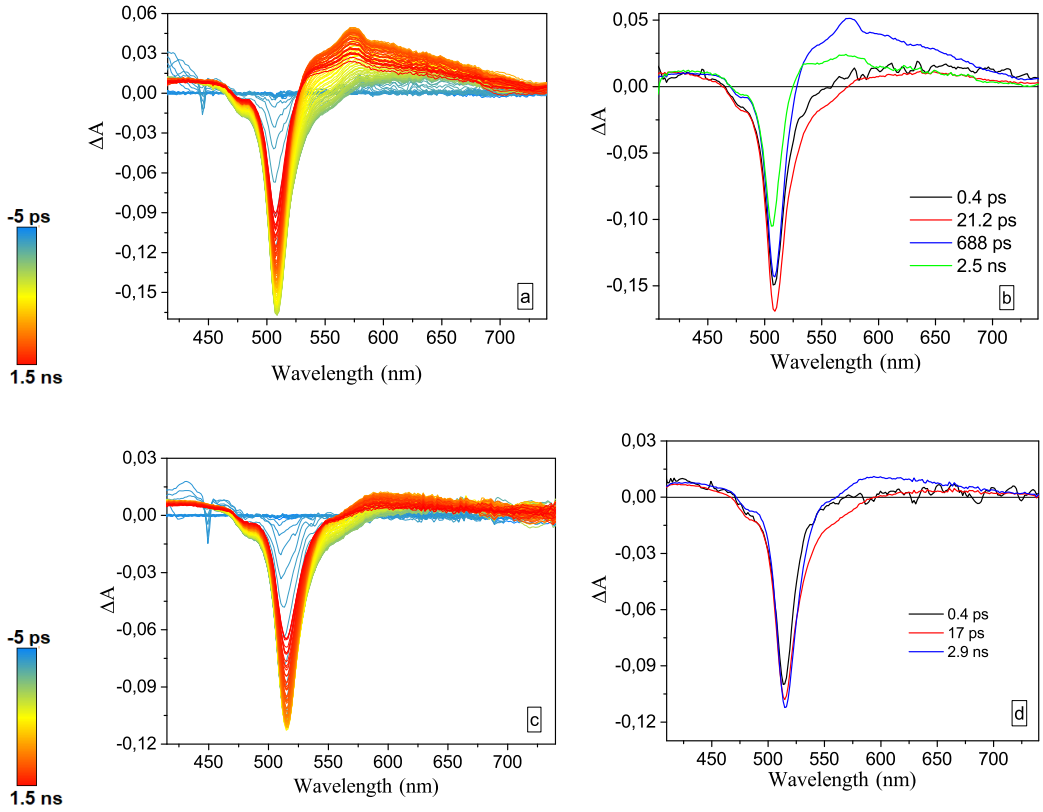

Figure 3.26: Transient absorption spectra recorded for BDP-AN-C-CZ (a) in toluene and relative Evolution associated difference spectra (b), and BDP-AN-N-CZ (c) in toluene with relative EADS (d).

In both these samples, transient data reveal the presence of an energy transfer process that contributes to the energy redistribution of the absorbed light. In both cases this phenomenon takes place in nearly 0.5 ps, as shown by an increase of the BDP bleaching signal from the black EADS to the red one, see panel b for BDP-AN-C-CZ and panel d for BDP-AN-N-CZ. This process occurs because upon excitation at 400 nm, which mostly populates the anthracene excited states, energy is transferred towards the bodipy moiety. Probably this same event is also present in dichloromethane, but it occurs on a timescale faster than the time resolution of the experiment.
The EADS relative to the sample with the carbazole in C-position (panel b), show that the BDP radical anion signal at 580 nm and the broad band over 650 nm assigned to the CZ radical cation rise on a time scale of 20 ps, while for the second sample a slightly faster rate of 17 ps is observed. However, the lower intensity of these bands evidences that in BDP-AN-N-CZ the charge separation is less efficient compared with the other sample, where the $BDP^{\cdot -} - AN - CZ^{\cdot +}$ signals are clearly visible.
The occurrence of a charge transfer process even in nonpolar solvents demonstrates that adding the CZ moiety increases the PET yield and the lifetime of the charge separated state.
Triplet quantum yields have been measured for these samples. Triplet formation is very efficient, in particular for BDP-AN-C-CZ that shows a quantum yield of

$\Phi_T = 1.00$ in dichloromethane. The high triplet quantum yield found in both the samples arises from the formation of a stable CS state, from which ISC has time to proceed following charge recombination (see table 3.6).

Compound	$\tau_T(\mu s)$		$\Phi_T(\%)$	
	DCM	TOL	DCM	TOL
BDP-AN	87	314	0.86	0.03
BDP-AN-N-CZ	95	248	0.90	0.04
BDP-AN-C-CZ	98	197	1	0.46

Table 3.6: Photophysical parameters of BDP-AN-C-CZ, BDP-AN-N-CZ and BDP-AN: τ_T as triplet-state lifetime measured by a nanosecond transient absorption spectrometer in deaerated solvents, while Φ_T as triplet quantum yield measured by the ground-state depletion method using 2,6-diodobodipy as standard.

Triplet quantum yields reported in table 3.6 evidence a solvent-polarity-dependence of triplet production, which supports the SOCT-ISC mechanism. In fact, in non polar solvent the decay rate to the CT state decreases, with consequent reduction of back electron transfer to the triplet state.
All the triplet-state lifetimes reported in table were measured by performing nanosecond transient spectroscopy upon excitation at 500 nm. Figure 3.27 reports the results obtained for BDP-AN-N-CZ in dichloromethane (a) and toluene (c).

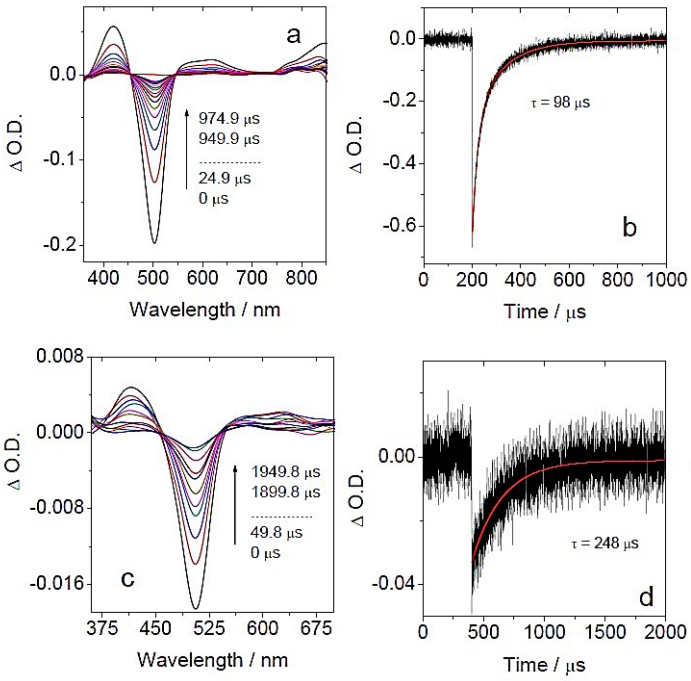

Figure 3.27: Nanosecond transient absorption spectra of compound BDP-AN-N-CZ in dichloromethane (a) and toluene (b) after excitation at 500 nm. In panel c and d their respective decay curves at 505 nm are reported.

The spectral shape is quite the same for all the samples in the different solvents and it is characterized by an intense bleaching band centered at 500 nm and two excited state absorption bands peaked at 420 nm and 610 nm. These features can be found also in the transient spectra of the isolated BDP chromophore. Since of this similarity in shape and lifetime, all the data of the triads in the different solvents can be interpreted as the triplet state in all the systems is completely localized on the BDP moiety. Nanosecond results also show that the triplet state lifetime is comparable in all the derivatives even if only in the case of BDP-AN-C-CZ the quantum yield of ISC appears enhanced in non polar solvents. Triplet state lifetime in toluene is always much higher than in dichloromethane, with the stronger difference between the two values for the triad BDP-AN-N-CZ (248 μs in toluene and 95 μs in dichloromethane, see table 3.6).
DFT calculations have been used to compute the ground-state geometries of the triads and the spin density distribution of the excited states. They confirm the orthogonal molecular structure of the triads whose representation at the ground state is reported in figure 3.28.

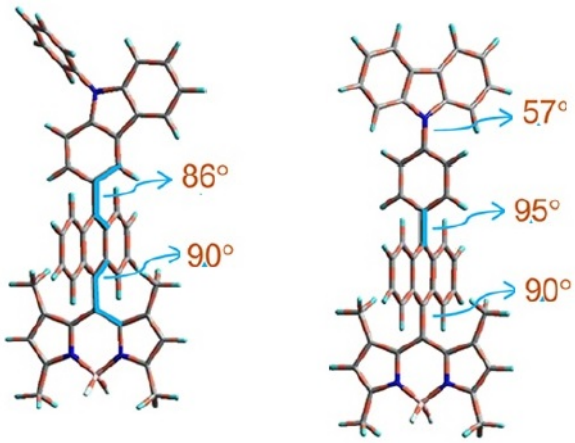

Figure 3.28: Optimized geometry of BDP-AN-C-CZ and BDP-AN-N-CZ calculated at B3LYP/6-31G level with Gaussian 09W.

The results obtained with DFT calculations evidence a nearly 90° angle between AN and BDP in both samples. However, the optimization of the ground state conformations for the sample BDP-AN-N-CZ reveals that the angle between the carbazole moiety and the antracene is 38°, due to the presence of the phenyl spacer that reduces the steric hindrance.
The analysis of the molecular orbitals highlights the density distribution in all the samples at their ground and excited states. In the triads, the HOMO is localized on the AN moiety while the LUMO is localized on the BDP moiety, in line with the first step of photoinduced electron transfer. Moreover, the spin density distribution of the radical cation and anion was calculated (figure 3.29).

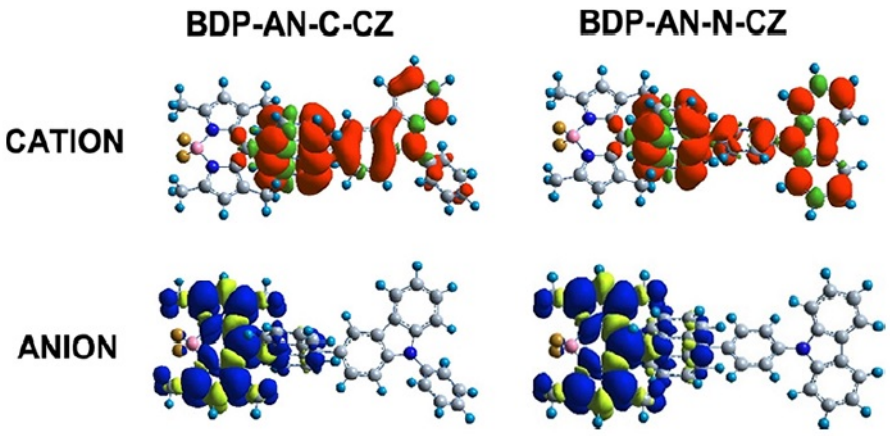

Figure 3.29: Optimized geometry of BDP-AN-C-CZ and BDP-AN-N-CZ calculated at B3LYP/6-31G level with Gaussian 09W.

In both cases the spin density in the anions is completely localized on the BDP moiety that acts undoubtedly as electron acceptor of the system, while the hole appears distributed between AN and CZ demonstrating their equal participation to the PET process in both the samples.
Considering the orthogonal geometry and the charge separation occurring in the triads, the triplet state is formed following SOCT-ISC mechanism. During charge recombination an internal rotation of the molecule favors the spin-forbidden transition. Considering the example of the triad with carbazole linked in C-position, the energy levels diagram reporting the kinetic constants found with transient spectroscopy can be depicted (figure 3.30).

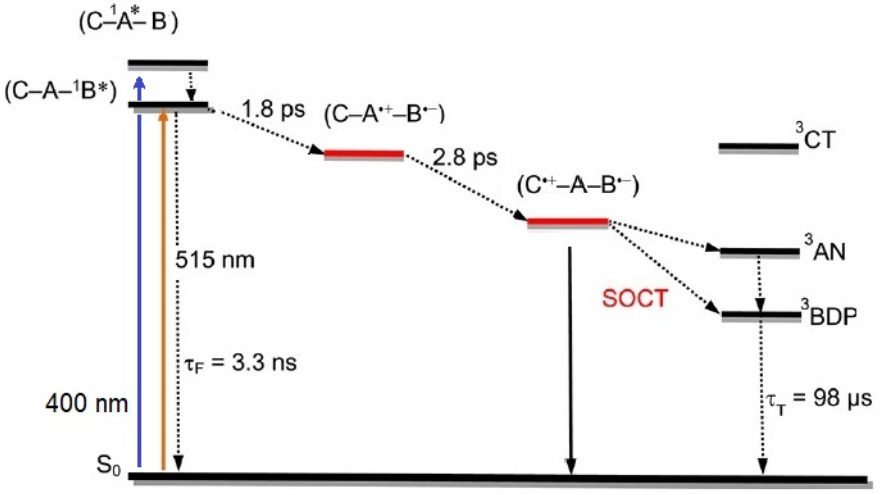

Figure 3.30: Photophysical Processes occurring on BDP-AN-CZ. C stands for the carbazole unit, A stands for anthracene, and BDP stands for the bodipy unit. The superscripted number designates the spin multiplicity.

The singlet excited state rapidly decays to the initial charge separated state in 1.8 ps, with electron transfer from the AN donor to the BDP acceptor. The hole in the antracene moiety suddenly recalls electron density from the electron-rich CZ moiety. For this reason the second step of electron transfer takes place in 2.8

ps, with formation of the ion pair $BDP^{\cdot -} - AN - CZ^{\cdot +}$. This state lasts in the time interval between femtosecond and nanosecond measurements, and the triplet state appears at the early microseconds timescale. The SOCT-ISC proceeds in the time interval between 1.5 ns and 1 μs. The final triplet state lives 98 μs.
The Jabloski diagram of the BDP-AN-N-CZ triad in dichloromethane should appear quite similar. In toluene it would be evident the different energetic stability of the charge separated state that, in this case, is higher in energy and less thermodynamically accessible.

Conclusions

In this section, we presented the spectroscopic characterization of two different triads able to undergo efficient triplet formation trough SOCT-ISC. We analyzed the effect of inducing a sequential electron transfer process on the efficiency of ISC. Two triads were designed as a series of donor-donor-acceptor systems. The two samples differ for the relative orientation and linking of the moieties, and they were studied to understand the influence of a multi step PET on the quantum yield and stability of a final triplet state. In BDP-AN-C-CZ triad an efficient and fast multi steps electron transfer was observed, resulting in a very high triplet quantum yield even in non polar solvents like toluene. The different attachment of the carbazole on the N-position influences considerably the PET process in the non polar solvent, where the rate of charge separation is strongly decreased. In a polar solvent the electron transfer proceeds in few picoseconds in both dyads and the charge recombination determined the population of the final triplet state.

Chapter 4

Photophysical properties of new organic dyes for Luminescent Solar Concentrators

The massive use of fossil fuels has nowadays determined an increase in pollution, global warming and acid rain. The exploitation of solar radiation can be an advantageous alternative to fulfill the high demand of energy at the base of human life, thanks to properties like infinite abundance, easy utilization and sustainability.
Photovoltaic devices are a fundamental instrument to convert sunlight into electricity. In the field of photovoltaics, the main research goals concern with reaching higher efficiency, better stability and lower costs, making solar based technologies a competitive and renewable source for energy production [45].
An important discovery in the achievement of higher efficiency of solar cells has been that of concentrating the solar radiation reaching the device through the operation of a Luminescent Solar Concentrator (LSCs). These devices are able to harvest solar light and concentrate it on a small surface exploiting the principle of total internal reflection. In the following, we will briefly describe the operating principles of solar cells and LSCs, more details will be found in appendix A.3.2.

4.1 Solar Cells and LSCs

Solar cells are photovoltaic devices whose active medium is a semiconductor material. Upon light absorption, the electrons of the semiconductor are promoted to the conduction band of the material where they can freely move. At the same time vacancies, or holes, are created in the valence band and move within the lattice as particles with a positive charge. If an electric field is applied to the semiconductor, the recombination of the electrons and holes is prevented and charge carriers are displaced in opposite directions creating an electric current. This current can be carried out through an external circuit and used for different purposes.
The performances of a solar cell are measured in terms of power conversion efficiency (PCE), calculated as the ratio between the incident light power and the output electrical power. First generation solar cells are based on crystalline silicon and they are still the most used devices so far. They have high PCE values and a good stability, but at the same time they are really expensive since they require a pure, defect-free silicon material [46].

Different generations of solar cells have been then developed, with the aim of obtaining good performances at a lower cost. Among the most cost effective alternatives we can find the dye-sensitized solar cells (DSSCs), quantum dot solar cells (QDSCs), conjugated polymer (PSCs) and perovskite solar cells (PVSCs) [47–50].

Although notable progress has been made in this field, the performances and costs of solar based technologies are still not competitive compared to traditional energy sources [51]. In this contest, Luminescent Solar Concentrators (LSCs) result as a valid tool to reduce costs and improve the performances of solar cells. In fact, these devices are able to collect solar light from a broad range of angles and *concentrate* it on a small area of a silicon cell coupled to them.
In recent years, planar LSCs have been used for the development of building integrated devices and mostly applied into windows facades, allowing to transform a simple window in a energy-producing element (example in Figure 4.1).

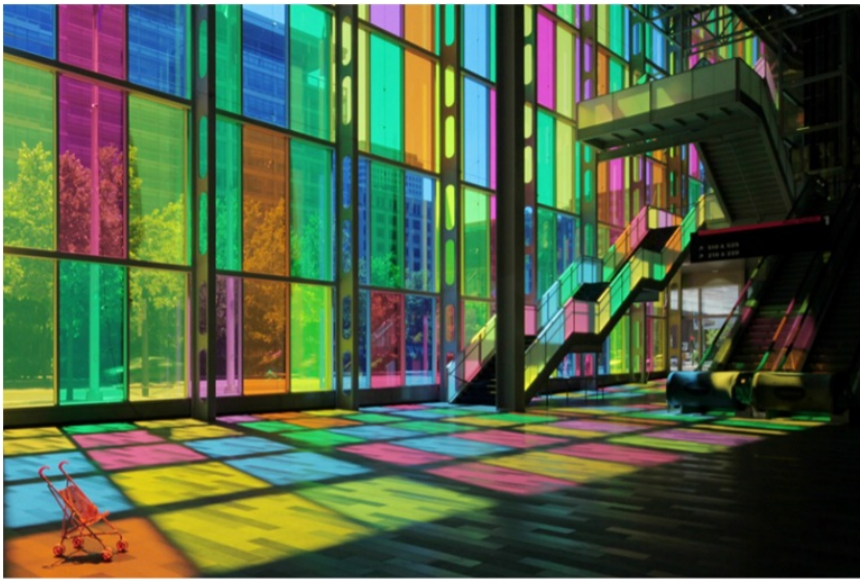

Figure 4.1: Diagram depicting luminescence solar concentrators for harvesting solar energy [52].

LSCs have further been used in noise barriers, artworks, urban furniture and bicycle sheds. In all these applications, one of the main advantages of these devices is their ability to efficiently concentrate incident light even if diffuse; that allows their use in different illumination conditions.
A luminescent solar concentrator is constituted by a transparent material with a specific dye dispersed inside (see figure 4.2).

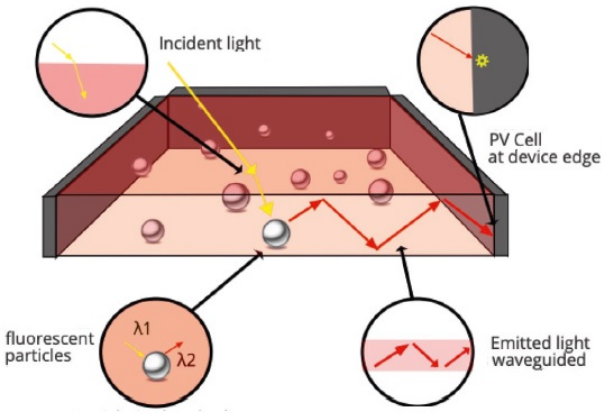

Figure 4.2: Diagram depicting luminescence solar concentrators for harvesting solar energy [53].

The dye must be able to absorb light in a certain spectral range and efficiently emit radiation in a red-shifted region. The spectral difference between absorption and emission, called Stokes-shift, is essential to prevent, or strongly reduce, the probability of re-adsorption of the emitted light, which limits the efficiency of the device. The light emitted by the dye propagates through the material into a specific angular range through total internal reflection (TIR) and it finally gathers at the edges.
Proper devices are fabricated such as the top of the concentrator is larger than its edges. A solar cell is then coupled to the edge of the LSC with sufficient reduced dimension. In this way, together with dimensions the costs of the cells are strongly reduced and the ability to concentrate both direct and diffuse light allows all the LSC different and difficult locations (most of all that on building integrated photovoltaics).
The light emitted in the TIR range is transported to the edges thanks to the transparent material acting as a wave guide. Before reaching the edges of the devices, the light is reflected many times, which decreases the fraction of light reaching the solar cell and determines the main loss channel of the device [54]. A brief description of the main losses of luminescence solar concentrators is reported in the appendix A.3.2.

Taking care of all the loss mechanisms, the optical efficiency of a LSC can be expressed as:

$$\eta_{opt} = (1 - R) \cdot \eta_{abs} \cdot \eta_f \cdot \eta_S \cdot \eta_t \cdot \eta_{tr} \cdot \eta_{self} \tag{4.1}$$

Different parameters determines the efficiency of an LSC device. Among them, we find the ratio between the absorbed photons over the incident light intensity (η_{abs}), the quantum efficiency of fluorescence (η_f), and the so called Stokes efficiency (η_S), that to say the ratio between the average energy of emission compared to absorption. The parameter η_t represents the efficiency of light trapping into the collector with dependence on its refractive index, while η_{tr} takes into account losses connected to light transported inside the matrix and η_{self} the losses arising from self-absorption. R is the reflection coefficient for the incident light on the surface.
The optical efficiency can be written in a simpler way as the ratio between the power coming out from the edges of the LSC (P_{out}), (which implicitly accounts

for all the loss mechanisms) and the incident power (P_{in}).

$$\eta_{opt} = \frac{P_{out}}{P_{in}} \tag{4.2}$$

The η_{opt} factor, termed as optical conversion efficiency, is directly connected to the performances of the LSC.
A further parameter to be taken into account is the Effective Concentration Factor (ECF), given by the product between the geometrical gain factor (G) and the optical conversion efficiency:

$$ECF = G \cdot \eta_{opt} \tag{4.3}$$

The geometrical gain factor G is the ratio between the top and the edge surface areas, which depends on the dimension of the device. The ECF parameter is better known as the Concentration factor (C).
A fundamental issue for the development of LSCs devices is the choice of an optimal fluorophore. The fluorophore must have a broad absorption spectrum, a high luminescence efficiency, a high photostability, a good solubility in the host matrix. Finally, its emission must match the absorption range of the PV cell coupled to the LSC.
At the same time, the material of the collector has to be highly transparent and it should be a good solvent for the specific dye. Usually plastic and glass, or organic solvents contained between them, are used as the matrix in which the fluorophore is dispersed to collect the incoming light.
Therefore both fluorescent molecules and matrix collectors must be chosen or designed with attention, balancing the properties of the latter in order to increase the efficiency of the former.

4.1.1 Matrix collectors

Optimization of the matrix component is required, since some of the reflection and scattering losses are matrix dependent. Among them, the re-adsorption of the emitted light by the host material and the value of the angle of total reflection depends on the refractive index of the matrix (TIR losses), while the photoluminescence quantum yield of the dye is affected by the solubility of the sample in the matrix and by its polarity.
Above all the properties of the matrix, a specific refractive index is needed, since it influences the surface reflection contribution to losses (R) and the trapping efficiency (η_{opt}) of the device. For this reason the n value for the best host material should balance the two contributions required for the maximization of the $(1 - R)\eta_{opt}$ factor (index value of 2.0) [55].
Another fundamental property of the matrix is a high transmittance in the visible and near-infrared range, as not to cover the absorption of the luminophore. Furthermore, an ideal host material should present easy processability for waveguide or thin-film fabrication.
Nowadays, polymers are the most used materials for LSCs matrices, thanks to their high transparency and easy processability. Polyacrylates, polysiloxanes, and polycarbonates are the most popular examples.
PMMA (poly(methyl methacrylate)) is a traditional inexpensive host waveguide material. It is a synthetic polymer characterized by a relatively low cost, high

transparency (92% for visible light), high refractive index, good photostability and chemical resistance, and excellent performance in all-weather conditions. Due to the C-H bond vibrations, this polymer begins to absorb at 730-800 nm, partially affecting the optical efficiency of luminophores emitting further into the red-infrared region. However, to overcome this problem the alkyl group can be deuterated. Instead of glass, PMMA does not break upon rupture and it has a high scratch resistance. Due to the acrylate groups it can be considered as a relatively polar polymer, able to solubilize most of the organic dyes [55].
Despite many benefits, the good but limited photostability of PMMA, together with the poor solubility of some efficient luminophores in its matrix, determine the necessity of finding new materials. For example, alternative polymeric matrices are based on PCMA (poly(cyclohexylmethacrylate)), whose minor polarity promotes the solubility and dispersion of many fluorophores. [56].
Together with purely polymeric materials, also organic-inorganic systems have been tested, characterized by a high refractive index and enhanced stability. Among them an important sol-gel-hybrid is the ureasil system, mostly used for the fabrication of new structural devices with cylindrical geometry.

4.1.2 Organic dyes

As previously mentioned, an important requirement for an efficient light collection is the separation between the fluorophore absorption and its emission spectral range, as well as a high fluorescence quantum yield. Numerous dyes are known for having very good fluorescence efficiency, even up to 100%, while having good Stokes shifts is not so common [57]. Organic chromophores used for LSCs applications generally present extended conjugated π frameworks with the addition of functional groups to modify the absorption and emission spectra.
An optimal dye should absorb in an extended region, covering a major part of the solar spectrum (figure 4.3), and it should emit in a region matching the absorption of solar cells (figure 4.4) [58].

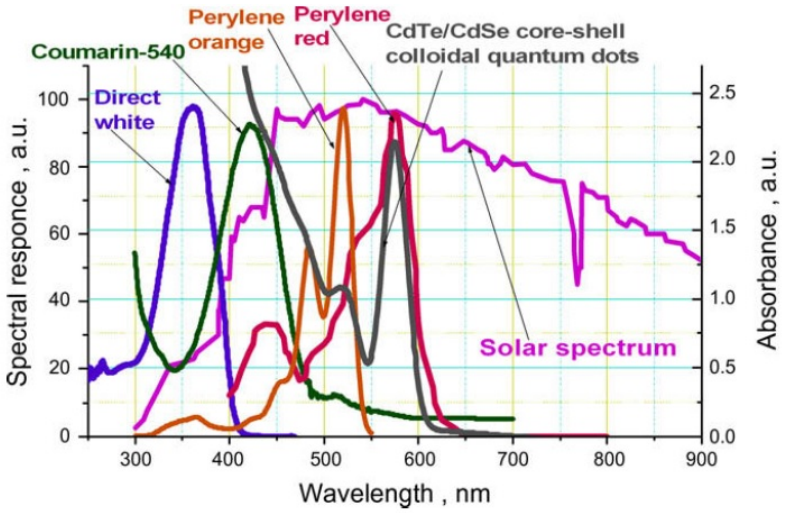

Figure 4.3: Comparison between the spectrum of the solar radiation and the absorption spectra of several organic dyes (and one quantum dot) that can be used in LSCs devices [58].

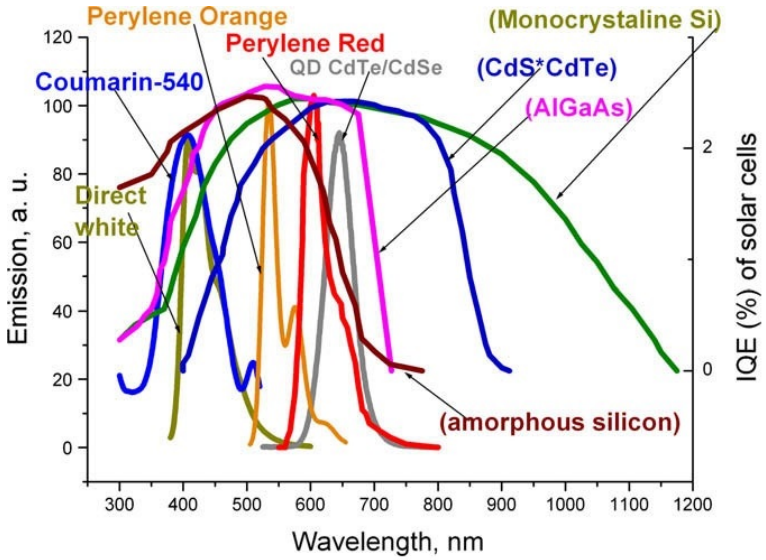

Figure 4.4: Comparison between the absorption spectrum of the silica cell and the emission spectra of the organic dyes presented above (and one quantum dot) that can be used in LSCs devices [58].

As shown in figure 4.4, not only organic dyes have been considered as fluorescent emitters for LSCs. One of the most promising alternatives are semiconducting nanocrystals also called Quantum Dots. They are crystals whose size is smaller than the Bohr radius of the bulk material, characterized by unique size-tunable optical properties that can vary over all the spectral range from visible to infrared. Other types of luminophores have been studied for the purpose, including metal oxides [59], metal complexes [60] and even protein complexes [61].
Organic dyes are among the most used chromophores. They usually present broad spectra and their absorption and emission properties are not only dependent to the structure of the molecule but also on the solvent and its polarity. Among the most used organic dyes, perylene compounds were deeply studied because of their high efficiency [62]. Particularly, Lumogen F Red 305 is now considered as the state of the art among the fluorophores used in LSCs.

Lumogen Red 305 is characterized by a very high photoluminescence quantum yield (97% in polymethylmethacrylate), a high photostability and a red emission that is well matched with the band gap of silicon cells [63].

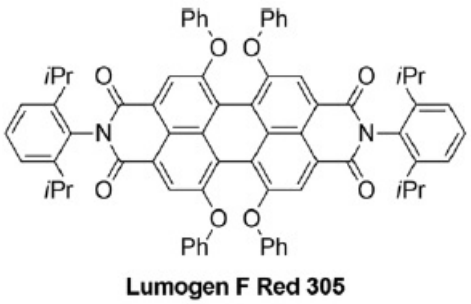

Figure 4.5: Structure of Lumogen F Red 305.

One of the major drawbacks of this dye is its strong tendency to aggregate via $\pi - \pi$-stacking interactions, leading to the formation of non-emissive absorption centers. Moreover, Lumogen F Red 305 has a very small Stokes-shift that determines a high probability of self-quenching. For these reasons, the search of new chromophores with improved performances is a very active research field.
In collaboration with the group of Prof. Reginato at ICCOM-CNR in Florence, we used transient absorption spectroscopy to analyze some newly synthesized promising dyes for LSC applications [64]. Initially, we considered two compounds belonging to the family of benzobisthiazole derivatives (BBT), whose structure is reported in Figure 4.6.

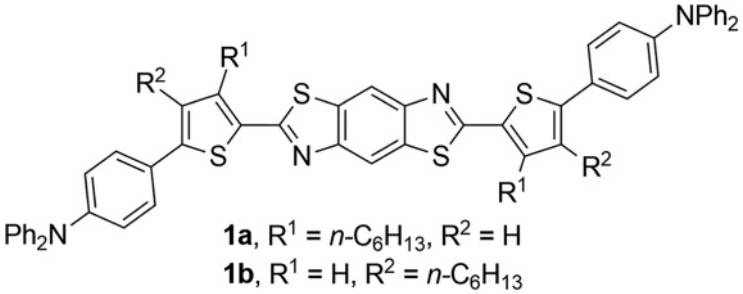

Figure 4.6: Structures of two benzobisthiazole derivatives

The two compounds are characterized by a benzobisthiazole heterocyclic core connected with the triphenylamine electron donating group through a thiophene ring as linker. The two samples differ in the alkyl chain position, which influences the solubility and conformation of the systems.
The two benzobisthiazole derivatives show a relatively high fluorescence quantum yield in solution (0.68 for 1a and 0.42 for 1b). The results obtained with the sample 1a were quite relevant. In fact, even if it is demonstrated that PMMA films with 1a dispersed at high concentration ($1.4 wt\%$) present red-emitting aggregates, they showed a very good optical efficiency with a maximum of 6.42%.
Although this efficiency is lower if compared to Lumogen R305, and the problem of aggregation remains a limit, our results [65] indicate that benzobisthiazole compounds are promising dyes, worth of further investigations and improvements.
In the following we will report with more details the characterization of a different, but promising as well, family of dyes based on a quinoxaline core, scarcely used before for such applications.

4.2 Photophysical properties of Quinoxaline fluorophores

This section is based on the publication on Journal of Materials Chemistry C, authors Costanza Papucci, Rima Charaf, Carmen Coppola, Adalgisa Sinicropi, Mariangela di Donato, Maria Taddei, Paolo Foggi, Antonella Battisti, Bastiaan de Jong, Lorenzo Zani, Alessandro Mordini, Andrea Pucci, Massimo Calamante and Gianna Reginato [71].

Thanks to the collaboration with the group of Prof. Reginato at ICCOM-CNR

in Florence, we analyzed a different family of compounds based on the functionalization of a quinoxaline core with different donor groups. Similar molecules have been already used in different optoelectronics devices, because of their advantageous properties such as good photon harvesting capacity, high Stokes shifts, high fluorescence quantum yield, and easy functionalization [66]. However, applications in LSC have not been previously reported.
It is also well-known that the quinoxaline structure is an ideal electron-withdrawing unit, used for the design of D-π-A organic sensitizers thanks to its intrinsic high electron affinity and easy diverse structural modifications [67].
In total, five quinoxaline derivatives were designed and synthesized. Their structures are reported in figure 4.7.

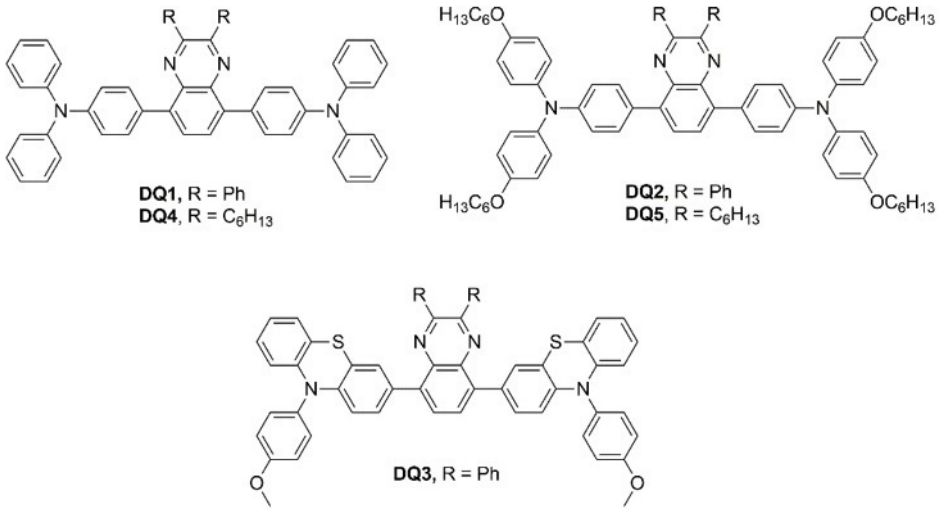

Figure 4.7: Structures of five quinoxaline derivatives with a similar central core of 2,3-diphenyl-quinoxaline (DQ1 and DQ3) and 2,3-dihexyl-quinoxaline (DQ4 and DQ5) .

Both DQ1 and DQ4 present two triphenylamine donor moieties at the 5 and 8 positions of the quinoxaline core, differing for the substituents in position 2,3: two phenyl groups for DQ1 and two alkyl chains for DQ4.
DQ2 and DQ5 have hexyloxy substituted triphenilamines as donor groups in position 5,8 of quinoxaline.
DQ3 presents two symmetric phenothiazines groups attached to the central core of the 2,3-diphenyl-quinoxaline in 5,8 positions.
The addition of different electron donating systems on the central core of the quinoxaline derivatives shifts the absorption maximum in the visible spectrum, because it influences the HOMO-LUMO energy difference. The presence of different chains on the acceptor and donor moieties varies the solubility of the molecule, while the the π-conjugated substituents in position 2,3 stabilize the LUMO energy of the core and influence its electron-accepting capabilities.
The optical properties of these compounds have been studied both in solution and in two different polymer matrices, PMMA and PCMA. The solvent used for all the samples is toluene, chosen because its refractive index (n= 1.496) is similar to that of PMMA (n= 1.491).
Each sample was dispersed in the polymers at different concentrations (0.2-2.2

wt%) and films were created with thickness of $25\mu m \pm 5\mu m$. All the films appeared homogeneous and with negligible macroscopic phase separation even at the highest fluorophore concentration, see figure 4.8.

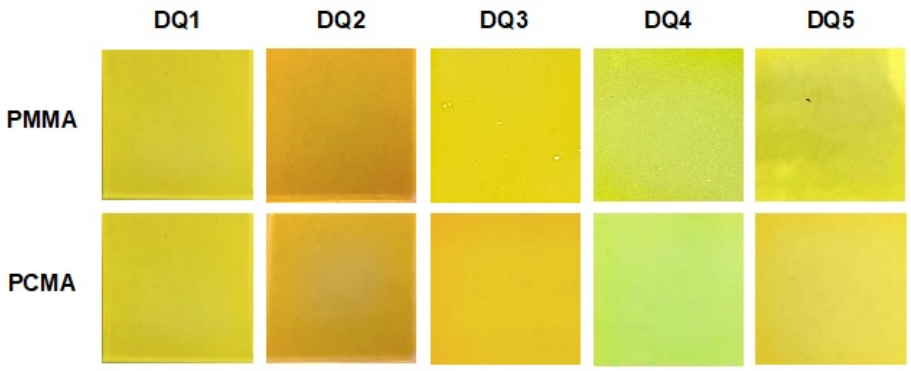

Figure 4.8: PMMA an PCMA films doped with DQ1-5 at $1.4wt.\%$ concentration under visible light illumination.

The parameters that we consider to classify a sample as suitable organic luminophores for LSCs are the fluorescence quantum yield in the specific medium, the Stokeses-shift value between absorption and emission peaks and the final optical efficiency η_{opt} calculated for the device.

4.2.1 Steady-state characterization

The absorption spectra of the compounds measured in toluene are reported in the left panel of figure 4.9. All the samples show a broad absorption band peaked between 400 to 460 nm.

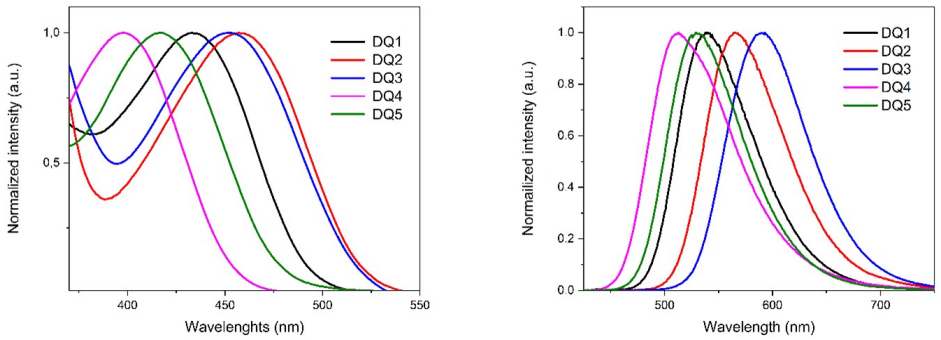

Figure 4.9: Left panel: normalized absorption spectra of DQ1-5 in toluene solution (0.01 mM) ; right panel: normalized fluorescence spectra of DQ1-5 in toluene (0.01 mM) respectively at 433, 457, 452, 398, and 416 nm excitation wavelength.

Comparing the different compounds, the 2,3-diphenyl-quinoxaline acceptor core of DQ1-3 determines an absorption band with central wavelength more red-shifted, because of the major conjugation induced by the presence of the additional phenyl rings. The electron donating effect of the subtituents on the 5,8 positions

is remarked by the observed progressive red-shift when moving from DQ1 (433 nm), where there are no substituents on the two symmetric triphenilammine, to DQ3 (452 nm), with two phenothiazine donors, to DQ2 (457 nm), with dihexyloxy substituted triphenilamines. The shape of the absorption band seems not to be influenced by the different molecular structures.
The emission spectra recorded for each sample in toluene are reported in the right panel of figure 4.9. The Stokes-shift values for all molecules is >100 nm, ensuring a limited overlap with the absorption band. All the emission maxima are in the range from 512 to 600 nm, with an intense peak similar for all the samples. Absolute fluorescence quantum yields were determined at room temperature through the integrating sphere method.
The spectroscopic parameters of all samples are summarized in Table 4.1.

Compound	λ_{abs} (nm)	λ_{em} (nm)	Stokes-shift (nm/cm^{-1})	Φ_f(%)
DQ1	433	538	105/95238	74
DQ2	457	567	110/90909	66
DQ3	452	601	149/67144	46
DQ4	398	512	117/85470	44
DQ5	416	529	112/89286	67
Lumogen FR305	575	610	35/285714	90

Table 4.1: Spectroscopic properties of all the compounds in toluene compared to Lumogen F Red 305 as reference.

DFT calculations have been performed for all the compounds at the B3LYP/6-31G* level. Energy and shape of the frontier orbitals were evaluated, revealing in each case a clear charge transfer character of the excitation from HOMO to LUMO. As shown for DQ1 in figure 4.10, the representation of molecular orbitals demonstrates that the electron density is delocalized on both acceptor and donor groups at the ground state, while it is localized on the acceptor moiety in the first excited state.

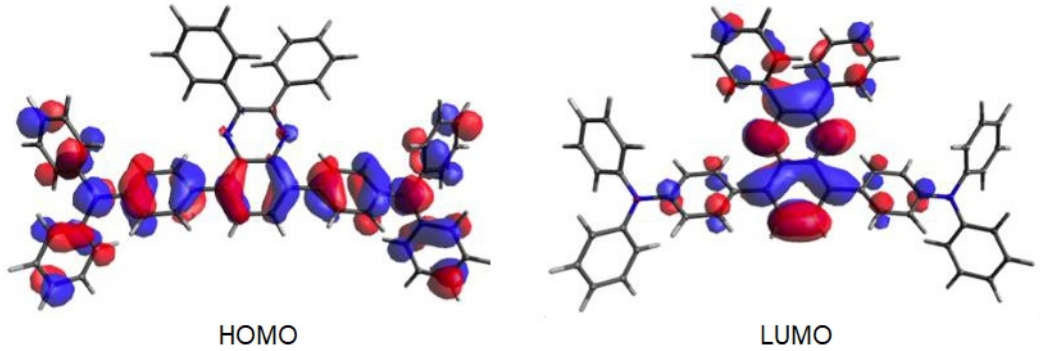

Figure 4.10: DQ1 ground-state frontier molecular orbitals (HOMO and LUMO) computed at the B3LYP/6-31G* level.

A similar HOMO-LUMO electron density was found for all the samples.

The absorption and emission properties of the samples dispersed in the polymer matrices were also analyzed.
The absorption spectra recorded in PMMA films are similar to those measured in toluene. In this case each sample has been studied with absorption and fluorescence spectroscopy at different concentrations in the matrix. For all the molecules, even in the highly doped films, no clear absorption band due to aggregates were evidenced (left panel figure 4.11).

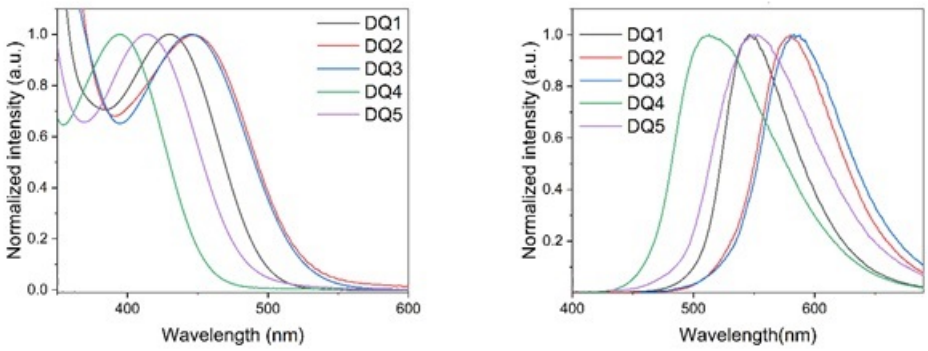

Figure 4.11: Left panel: absorption spectra of DQ1 to DQ5 in PMMA films at concentration 1.0 wt.% ;right panel: fluorescence spectra of the same films upon excitation at 430 nm.

Comparing the fluorescence spectra of each sample at different concentrations, a progressive red-shift at higher wt. % values is evident, and it can be associated to weak auto-absorption phenomena in the matrix.
The measured Stokes-shift values exceed 100 nm also in PMMA, as reported in table 4.2.

Compound	λ_{abs} (nm)	λ_{em} (nm)	Stokes-shift (nm/cm^{-1})
DQ1	430	546	116/86207
DQ2	447	580	133/75188
DQ3	446	583	137/72993
DQ4	406	512	107/93458
DQ5	414	553	139/71942

Table 4.2: Spectroscopic properties of compounds in PMMA.

Fluorescence quantum yield were measured for all the dispersed samples at each concentration. High values were recorded, particularly for sample DQ1, see figure 4.12.

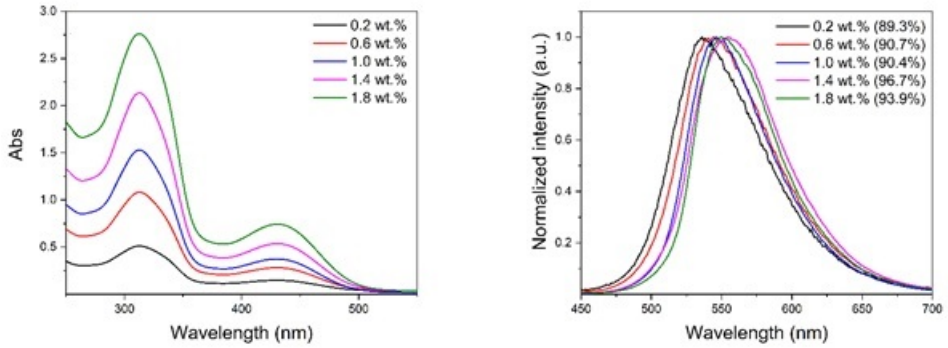

Figure 4.12: Left panel: absorption spectra of DQ1 in PMMA films at all the different concentrations tested (wt.%) ; Right panel: fluorescence spectra of the same films with excitation at 430 nm. Fluorescence quantum yield are reported in parenthesis.

DQ1 in PMMA has an higher fluorescence quantum yield than in solution (table 4.3), with values of quantum efficiency that rises with the increasing of sample concentration. Only at 1.8 wt.%, the formation of a fraction of microscopic fluorophore aggregates in the matrix determines quenching effects and a slight decrease of fluorescence. Some aggregates are already present at 1.4 wt%, but they do not affect the brilliant emission of DQ1 films (figure 4.13).

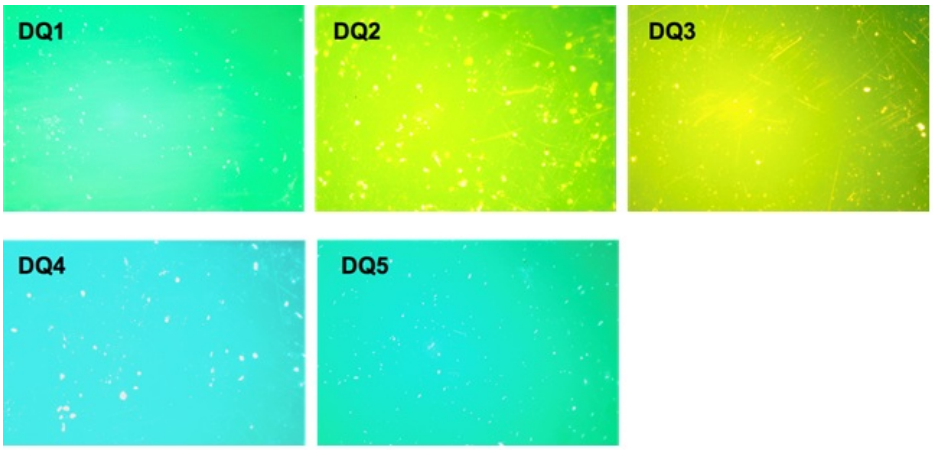

Figure 4.13: Fluorescent microscopy images of 1.4 wt.% DQ1-5 in PMMA films.

On the contrary, aggregates are clearly present for nearly all the other samples at high concentrations in the polymer. For DQ5 at 1.4 wt% no aggregates are observed and quantum efficiency values are in the range of 50-60%.

Concentration	DQ1 $\Phi_{ef}(\%)$	DQ2 $\Phi_{ef}(\%)$	DQ3 $\Phi_{ef}(\%)$	DQ4 $\Phi_{ef}(\%)$	DQ5 $\Phi_{ef}(\%)$
0.2 wt.%	89	30	56	81	55
0.6 wt.%	91	41	50	76	61
1.0 wt.%	90	/	47	75	53
1.4 wt.%	96	35	32	64	50
1.8 wt.%	94	35	35	68	52

Table 4.3: Quantum efficiencies of samples DQ1-5 in PMMA.

The results obtained when the samples are dispersed in PCMA are similar to those in PMMA. Stokes-shift values are in range of 90-120 nm and quantum efficiencies are similar to those recorded in the other matrix or in some case evenly higher. This is related to the less polar character of PCMA that increases the compatibility between polymer and fluorophores. For DQ5, quantum efficiency decreases with increasing concentration, passing from 80% at 0.2 wt.% to 53% at 1.8 wt.%. A second emission band is observed in the fluorescence spectrum of DQ5, attributed to the formation of emissive aggregates (purple line in figure 4.14).

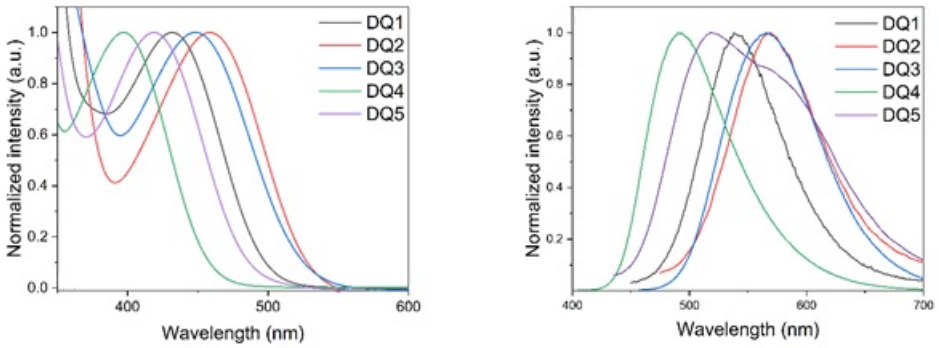

Figure 4.14: Left panel: absorption spectra of DQ1 to DQ5 in PCMA films at concentration 1.0 wt.% ; right panel: fluorescence spectra of the same films upon excitation at 430 nm.

This particular behavior of DQ5 can be ascribed to an excess of hydrophobic substituents on the D-A-D structure that decreases the solubility in the matrix in spite of its minor polarity.
All the spectroscopic results reported above demonstrate promising properties of these compounds for applications in LSCs devices. Particularly, DQ1 evidences a good stability and solubility in both the tested polymer matrices and very high fluorescence quantum yields.

4.2.2 Transient absorption spectroscopy

In order to characterize the excited states of these samples and their relaxation processes in toluene, transient absorption spectra have been recorded in the time

interval from -5 ps to 1.5 ns and they have been analyzed with a global fit based on sequential decay scheme. The transient absorption spectra of DQ1, DQ2 and DQ3 are reported in Figure 4.15, together with their Evolution Associated Difference Spectra (EADS) obtained from global analysis.

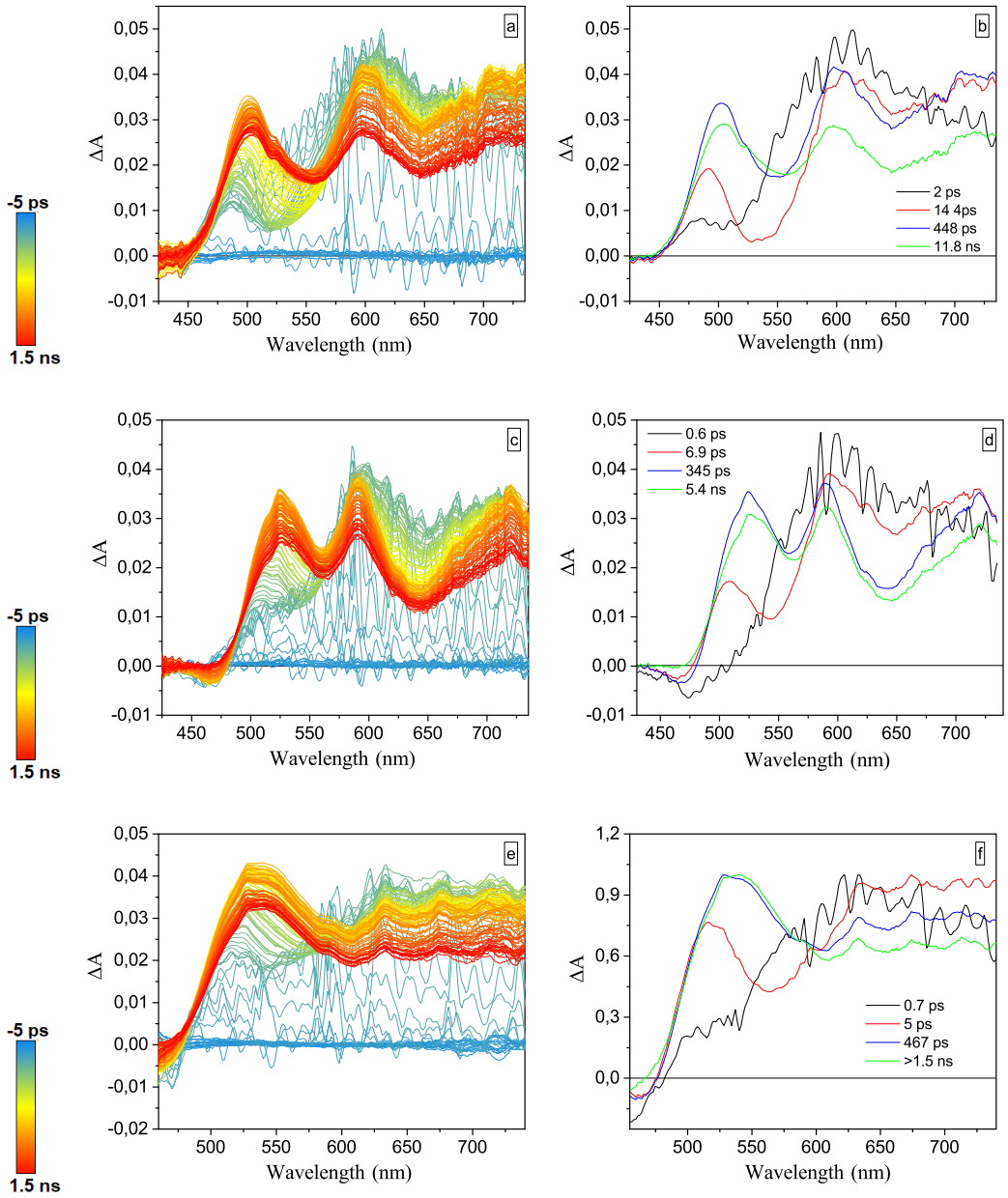

Figure 4.15: Transient absorption spectra recorded for DQ1 (a), DQ2 (c) and DQ3 (d) in toluene with excitation at 400 nm and relative EADS (b, d, f) obtained with global analysis.

Compounds DQ1 and DQ2

Transient spectra of the first two samples are very similar (figure 4.15 panel a,c). Spectra of DQ1 present a positive broad band (excited state absorption, ESA) covering the entire probed spectral range. This band overlaps with negative contributions coming from both bleaching signal (GSB) at 440 nm, and the stimulated

emission band (SE) that is centered at 532 nm at early times and red-shifts at 560 nm at longer time delay. sAlthough spectral superposition, the overall signal is positive in the entire spectral range. The transient spectra of DQ2 also show a broad positive band ranging from 450 nm to 750 nm, with the overlapping contribution of the negative bleaching band at 460 nm and the negative stimulated emission band that shifts in time from 542 to 562 nm.
The global analysis extrapolates four different spectral components (EADS, bottom panels in Figure 4.15). The first component (black line) appears as a broad positive band peaked at 600 nm that in the case of DQ1 lives until 2 ps, while in DQ2 evolves towards the following component (red line) in 600 fs.
The evolution among the two initial EADS can be interpreted in terms of a fast electronic relaxation of the molecule, as evidenced by the red shift of the stimulated emission signal. DFT calculations predict that the low lying excited state, to which the sample is promoted upon light absorption, has a charge transfer character. The second spectral component (red line in panels b,c) presents a positive peak at 700 nm, which, according to previous literature [69], can be assigned to the quinoxaline anion.
After 14.4 ps in DQ1 and 6.9 ps in DQ2, the red component evolves to the blue one, where the spectral shape does not change very much, but the stimulated emission signal further red-shifts of about 30 nm and partially recovers. The dynamic Stokes-shift observed for the emission band is indicative for an excited state relaxation promoted by solvent reorganization.
For both samples the final EADS lives beyond the time interval of the measurement (1.5 ns) in agreement with their high fluorescence quantum yield.

Compound DQ3

The transient spectra of DQ3 are slightly different from the previous ones, reflecting the presence of a different donor. An electronic relaxation process can be associated to the evolution between the two initial EADS, appearing quite fast (700 fs). It is accompanied by the partial recovery of the ground state bleaching band below 450 nm and by the red-shift of the stimulated emission band.
An additional dynamic Stokes-shift is observed in the evolution from the red to the blue component (40 nm) occurring in 5 ps. In the following evolution occurring in about 470 ps, the intensity of the ESA peak at 550 nm significantly increases. This band is possibly attributed to the phenothiazine cation. The evolution towards final green EADS is not associated to significant spectral changes.

Compounds DQ4 and DQ5

Transient absorption spectra have been recorded also for DQ4 and DQ5, the two samples characterized by a D-A-D structure with a 2,3-diexilquinoxaline as acceptor core and two triphenylamine as donor moieties. The donor system of DQ5 presents two hexyloxy groups that determine a red-shift of its absorption spectrum. Both these samples present large Stokes-shifts between absorption and emission (117 nm for DQ4, 112 nm for DQ5).

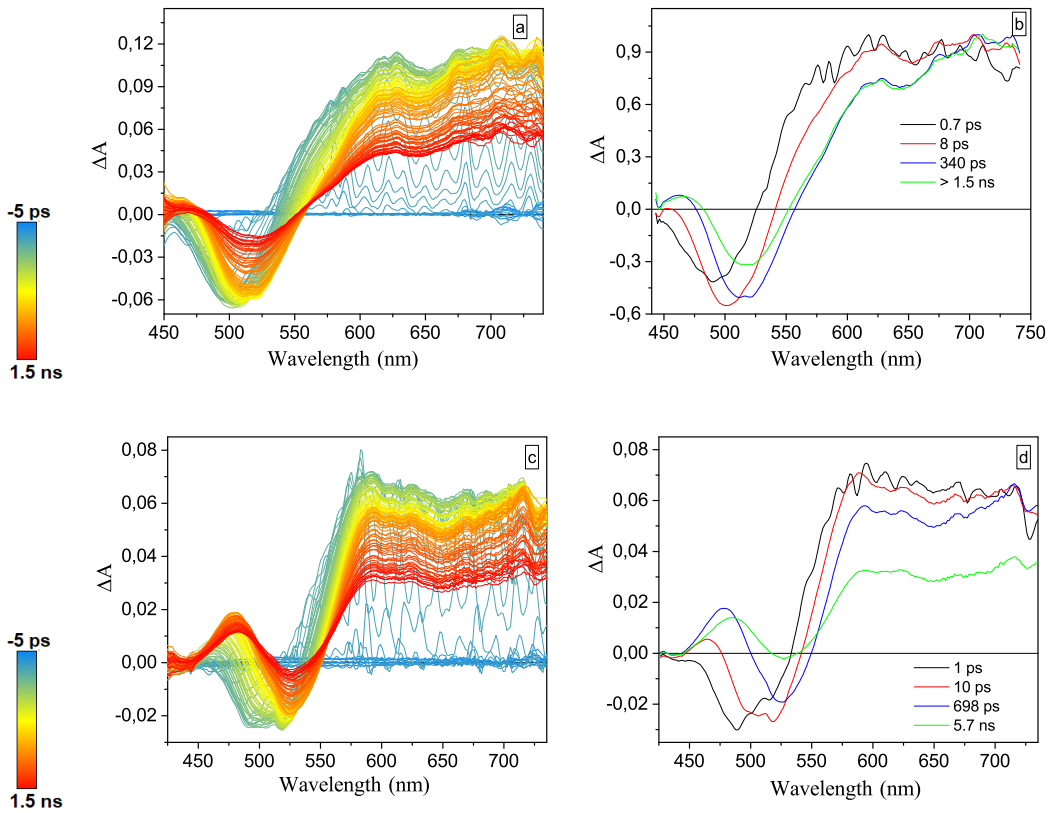

Figure 4.16: Transient absorption spectra recorded for DQ4 (a) and DQ5 (c) in toluene with excitation at 400 nm and relative EADS (b, f) obtained with global analysis.

In the transient spectra of DQ4 the negative bleaching band is not visible because it is particularly blue-shifted compared to the other samples. Transient spectra present a negative band centered at about 510 nm, and a broad positive ESA band extending up to the red-edge of the investigated spectral window. The EADS of DQ4, reported in panel b of figure 4.16, show that at early times the stimulated emission band is centered at 489 nm. The emission intensity increases in about 0.7 ps and it red-shifts within 7.8 ps peaking at 517 nm (red trace) . Besides a red shift of the entire spectrum, no significant spectral evolution in observed within the investigated time interval.
In case of DQ5, the GSB band is partially visible and centered at 417 nm. Also in this case, the stimulated emission band undergoes an important red-shift. Initially peaked at 480 nm, it shifts during the initial 10 ps of about 100 nm because of the excited state vibrational and solvent induced relaxation. A broad positive ESA is observed ranging from 550 to >700 nm also in this case. The evolution from the red to blue EADS is furthermore accompanied by the rise of a positive signal at about 480 nm. The signal intensity decays to about one half within 690 ps and the final spectral component (green EADS) lives beyond 1.5 ns.
For all the sample, no dark states seems to be involved in the photodynamics. In fact the evolution of the transient signal only evidences the progressive decay of the excited state initially populated by light absorption which mainly decays in a radiative way.

Considering the promising behaviour of these samples, we further evaluated their excited state properties when dispersed in the polymer matrix. The following figure reports the transient spectra of DQ1 DQ2 and DQ3 in PMMA.

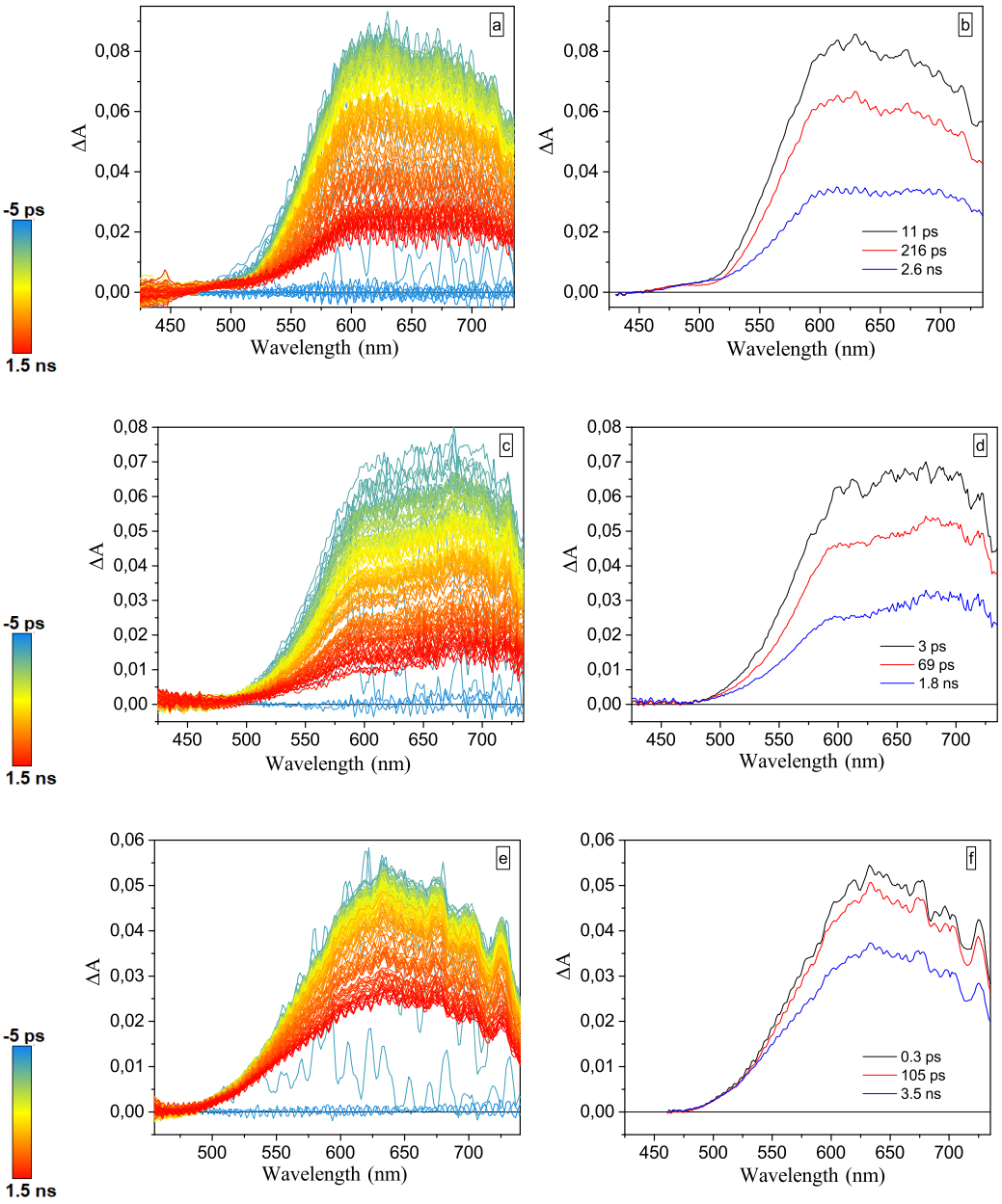

Figure 4.17: Transient absorption spectra recorded for DQ1 (a), DQ2 (c) and DQ3 (d) in PMMA with excitation at 400 nm and relative EADS (b, d, f) obtained with global analysis.

Compounds DQ1, DQ2, DQ3 in PMMA

For all the three samples, the transient absorption spectra are very similar in shape and time evolution (panel a, c and e figure 4.17). A broad positive band due to the excited state absorption covers most of the spectrum, while in the bluest region the decreased intensity is due to the overlapping contribution of the

negative bleaching/ stimulated emission signals.Although progressively decaying in time, transient spectra do sot show significant evolution. This behaviour is probably due to the rigidity of the PMMA matrix compared to the solvent that partially prevents vibrational and structural relaxation processes.
Looking at the EADS reported in panel b, d, f of figure 4.17, the excited state of all the samples lives behind 1.5 ns. Comparing the residual intensity of the signal in the three samples, it seems that the relative larger decrease observed for DQ1 does not agree with the higher fluorescence quantum yield measured for its 1%wt dispersion in matrix.

Compounds DQ4 and DQ5 in PMMA
The transient spectra of DQ4 and DQ5 in PMMA with the respective analysis are reported in figure 4.18.

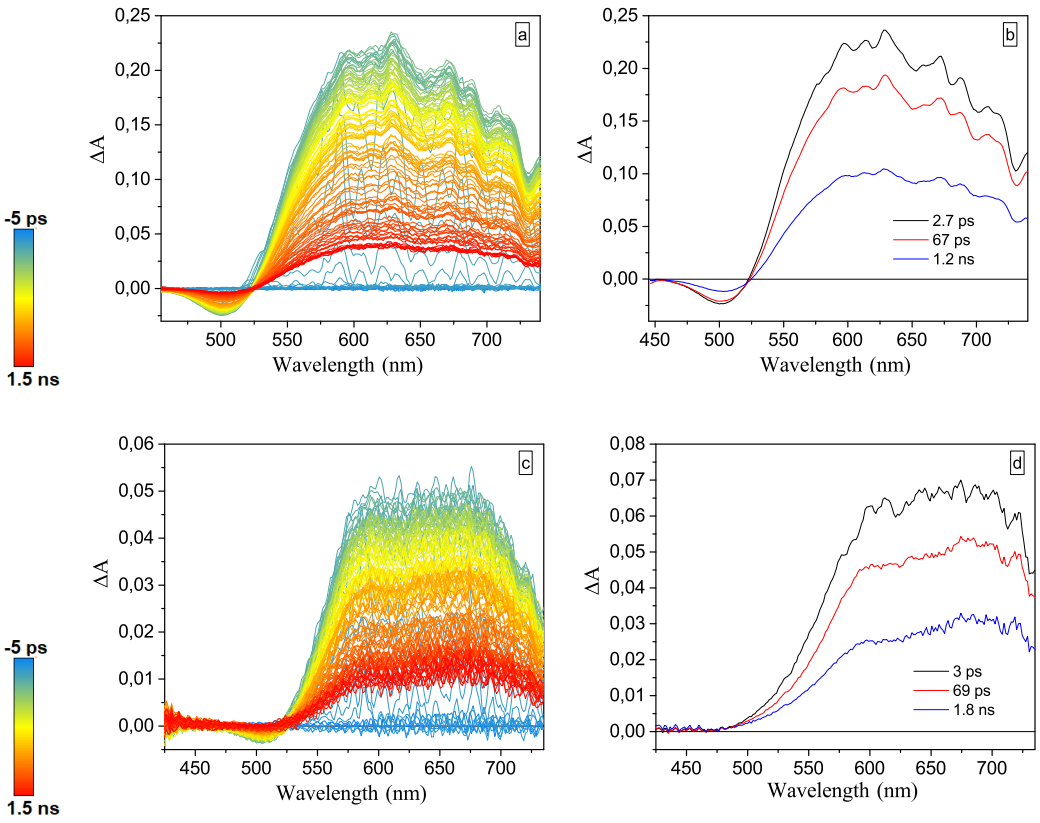

Figure 4.18: Transient absorption spectra recorded for DQ4 (a) and DQ5 (c) in PMMA with excitation at 400 nm and relative EADS (b, f) obtained with global analysis.

Results of the two samples are very similar. The spectra are characterized by a negative band centered at 500 nm and a broad positive band ranging from 550 to 750 nm, respectively due to the stimulated emission and absorption from an excited state of the molecule. Looking at the evolution of the transient signal, it appears that the excited state of DQ4 decays faster than that of DQ5, as aslo shown by the comparison of the kinetic traces recorded on the ESA band reported in figure 4.19.

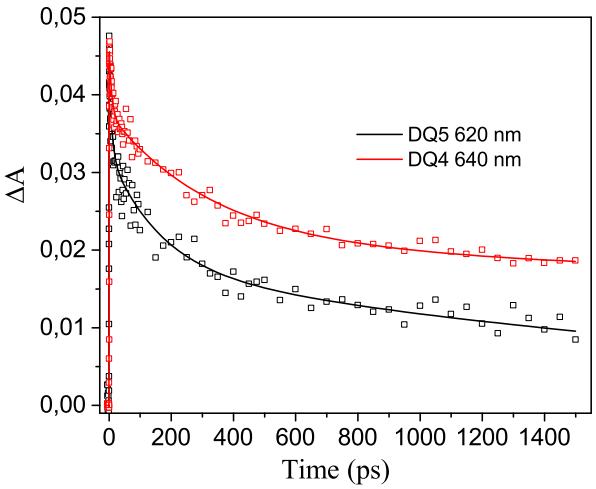

Figure 4.19: Comparison between DQ4 kinetic trace at 640 nm (red trace) and DQ5 kinetic trace at 620 nm (black trace). .

Also in this case the spectral evolution appears limited by the effect of the matrix. The intensity of the residual signal agrees with the higher quantum yield measured for DQ4 sample in PMMA with dispertion at 1%wt.
Some of the samples have been studied also in PCMA. In all the cases the results are very similar to those in PMMA. As an example in figure 4.20 the transient spectra and associated EADS of DQ5 in PCMA are showed.

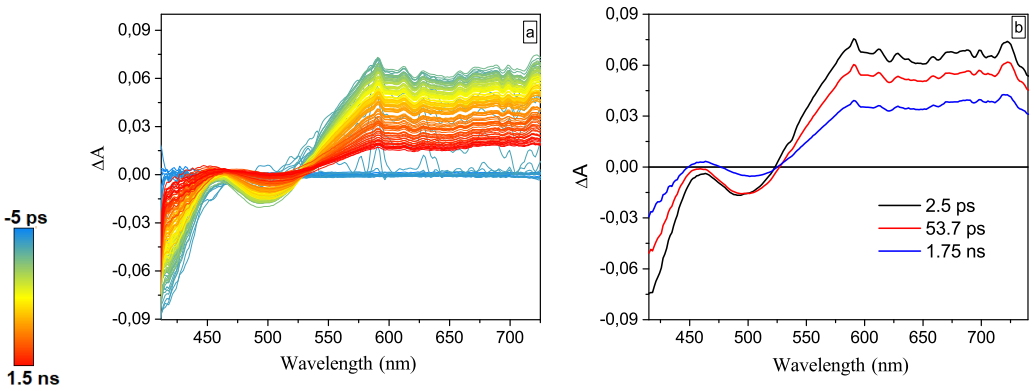

Figure 4.20: Transient absorption spectra recorded for DQ5 in PCMA (a) with excitation at 400 nm and relative EADS (b) obtained with global analysis.

The decay of the ESA band of DQ5 in PCMA is comparable to that recorded in PMMA and it is faster than in toluene. A comparison of the three different kinetic traces recorded on the ESA band is reported in figure 4.21.

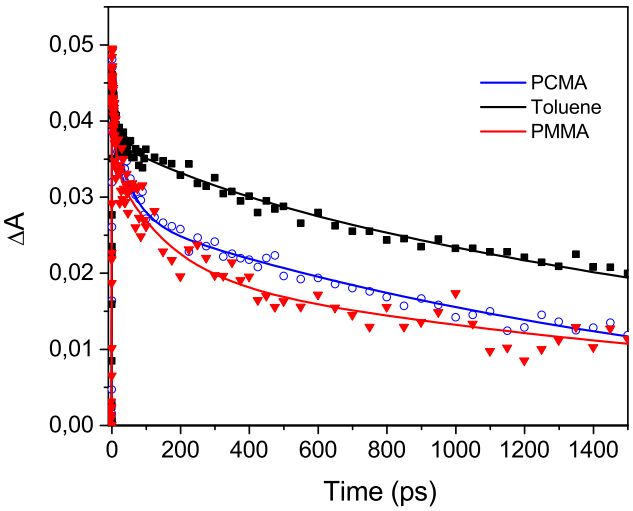

Figure 4.21: Comparison of the kinetic trace at 640 nm measured for DQ5 in toluene (black squares); PCMA (blue open circles); PMMA (red filled triangles).

In both polymers an initial fast decay contribution is observed compared to toluene, in agreement with the higher fluorescence quantum yield measured in solution. A possible explanation for the faster excited state decay observed in the matrix is the prevention of structural rearrangements operated by the rigid environment. This behavior slightly affects the very high fluorescence quantum yields obtained in solution, but in any case the optical efficiency of the sample is good, as shown in the following section.

4.2.3 Optical efficiency results

The transient absorption measurements of all the dyes in the PMMA matrices, show that the excited state relaxation is dominated by the radiative channel, a very beneficial feature for compounds to be employed as LSC emitters. In this way, transient spectroscopy suggest and support the good employment of these compounds as Luminescence Concentrators. The LSC performances of LR305, DQ1 and DQ4 prototype devices were evaluated following a recent protocol [70], for which we use a commercially available system described in ref. [71]. Particularly, we evaluated the ratio of the photons collected at the LSC edges to the number of absorbed photons by the embedded fluorophores (ηint), and the ratio of photons collected at the LSC edges to the number of total incident photons (ηext).
Comparing the efficiencies of the dyes with that of the commercial reference LR305, results are really impressive and promising, as reported in table 5.1.

Luminophore	Matrix	Concentration (wt%)	η_{int}(%)	η_{ext}(%)
LR305	PMMA	1.0	16.6	4.7
DQ1	PMMA	1.4	42.9	6.2
DQ4	PMMA	1.8	27.9	3.6

Table 4.4: Optical efficiency results for samples DQ1 and DQ4 in PMMA matrices.

DQ1 demonstrates a very high efficiency, a result that reflects its high fluorescence quantum yield. The ηint of the LSC based on LR305 resulted the lowest (16.6%). According to the ηint determination, the broader absorption band of LR305 probably affects this parameter with a great extent.

4.2.4 Conclusions

A new family of organic fluorophores has been spectroscopically characterized for applications in LSC devices. These molecules are characterized by a D-A-D structure with a quinoxaline central core symmetrically linked to two donor moieties, triarylamines in DQ1,2,4,5 and phenotiazine in DQ3. PMMA and PCMA thin films were prepared with rising concentration of each sample and tested as LSC devices.
DFT calculations and transient spectroscopy measurements showed that the D-A-D structure determines the formation of an excited state with charge transfer character (CT). Particularly, results demonstrated that the radiative deactivation from this CT state is the main relaxation channel. High quantum yields were recorded in the 550-650 nm spectral range most of all for DQ1 and high Stokes shifts permitted a reduction of autoabsorption phenomena.
Optical efficiencies were evaluated for LR305, DQ1 and DQ4. In particular DQ1 in PMMA demonstrated outstanding performances ($\eta_{int} = 42.9\%$ and $\eta_{ext} = 6.2\%$). This result was associated to the high phase compatibility between molecule and matrix and to the excellent quantum yields demonstrated also in the polymer structures.

Chapter 5

Photoswitching mechanism of bistable Hydrazones

Photoswitches are commonly defined as chromophores that can *reversibly* be converted from one state, or isomer, into another by the absorption of a photon [76]. Light absorption by a molecular photoswitch often implies not only a change in the absorption spectrum of the molecule, but also the possibility of a reversible change in geometry, polarity, refractive index or charge distributions.
Because of their properties, photoswitches can act as trigger elements in different materials, ranging from biological systems to optical waveguides.

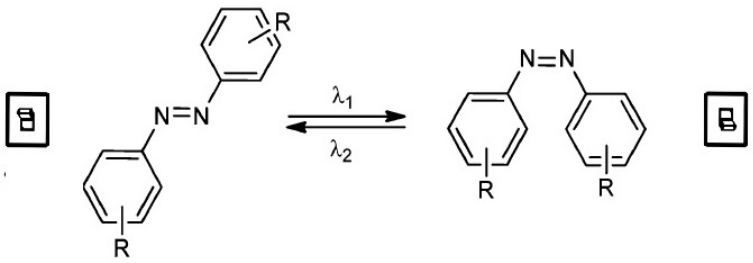

Figure 5.1: Azobenzenes molecular structure as an example of photoswitch.

Many functions and properties of different materials, biomolecules and devices are regulated by *switching* operations, themselves controlled by specific external input. For this reason, molecular photoswitches find numerous targets of applications among different fields such as computer chips, optical recording systems, cellular activities etc.
Compared to other external inputs, light has attractive properties in the remote control of the switching event, being non-invasive, devoid of contamination for the interactive system, and orthogonal toward most processes. Furthermore, its wavelength can be precisely regulated to obtain a high spatial and temporal resolution.
Since their initial applications, molecular photoswitches have been used in many fields of chemistry and material science, such as fluorescence imaging [73], optical recording [74], production of materials with optoelectronic and/or optomechanical properties [75] [72] or photocontrol of biological systems [76]. Above all, the particular application in molecular machines recently received the recognition of a Nobel Prize, main evidence of the outstanding promises of this field.

To date, a great number of photoswitches have been synthesized and characterized. Among the light induced structural variations, the most common photoinduced processes are cis-trans isomerization (occurring for instance for azobenzenes, stilbenes, and hemithioindigos) and photoinduced ring opening/closure reaction (spiropyrans, diarylethenes, and fulgides) [76].
Azobenzenes are among the most commonly applied photochromic molecules reported in literature (figure 5.1), because of their easy synthesis, high yield of photostationary states, fast photoisomerization (within a few picoseconds) and low photobleaching rate. Furthermore, reverse cis to trans process can take place with both thermal isomerization or absorption of visible light. The most important limit of these chromophores is the high influence of solvent and substituents on the activation barrier for thermally induced back-isomerization.
Diarylethenes are also among the most used photoswitches. Their open/closed ring isomerization (few picoseconds) maintains good performances over 10^4 times of cycles. Their synthesis is easy and short and their isomerization determine the change of different geometrical, electronic, refractive and chiral properties. One of the main properties of these chromophores is the absence of thermochromism.
In the past few years, several new promising photochromic molecules have been designed including hydrazones [77], imidazole dimers [78] and donor-acceptor Stenhouse adducts. [79].

5.1 Properties of a molecular photoswitch

Each molecular photoswitch is characterized by a specific set of properties, ideally tunable according to the desired application. Among them, what is generally valued is an high isomerization quantum yield, high extinction coefficients (possibly at visible to near-infrared wavelengths in case of biological applications), high equilibrium composition (photostationary states), high control over switching rate and good resistance against photodegradation (fatigue). In the special case of *in vivo* applications, light-mediated reversibility is also desired.
In a generic photochromic reaction, the two isomers A and B are most often characterized by different absorption spectra.

$$\mathrm{A} \underset{\lambda_\mathrm{B},\Phi_{B\to A}}{\overset{\lambda_\mathrm{A},\Phi_{A\to B}}{\rightleftharpoons}} \mathrm{B} \tag{5.1}$$

Upon prolonged illumination, the system reaches the photostationary state, which contains mostly one of the two isomers. Even though the definition of what constitutes an ideal photoswitch mostly depends on its application, four main parameters affect the *performance* of a molecular photoswitch [79]:

1. *Addressability*: this parameter is related to the absorption features of the two isomers. It is influenced by how strong the photoswitch absorbs light at a given wavelength (σ) and by the difference in the absorption wavelength of the two isomers.

2. *Efficiency*: this parameter is related to the photoisomerization reaction and its rate. It depends on the quantum yield of the reaction, that quantifies how many absorbed photons are used to induce the photoreaction. Moreover, the efficiency is affected by the degree of photoconversion in the photostationary state.

3. *Thermal stability*: this parameter is associated with the thermal half-life factor ($\tau_{1/2}$) that quantifies the time needed for half of the molecules to undergo back-isomerization at a given temperature. One of the two isomers is less thermally stable with respect to the other and thermal stability defines how much time the unstable isomer lives before being transformed back to the stable one.

4. *Reliability*: this final factor expresses the fatigue resistance, that to say how many times the back and forward photoreactions can proceed without a degradation of the photoswitch.

Depending on the relative *thermal stability* of the isomers, two categories of photochromic chromophores can be classified.
A photoswitch is defined as *T-type* (thermally reversible type) if it thermally reverts to the more stable isomer without absorption of light, within a timescale ranging from milliseconds to few minutes [80].
The photoswitch is instead defined as *P-type* (photochemically reversible type) if the molecule shows an extremely slow thermal back isomerization, but can be reverted to the initial form upon absorption of light.
T-type photoswitches are generally more common, but for most applications, bistable switches are required such that deactivation could be triggered in a controlled way by a second irradiation step. In many cases, photogenerated colored isomers of organic molecules are thermally unstable and undergo back isomerization in the dark. Dispersion in a polymer matrix or aggregate formation are only two of the numerous attempts to stabilize the photogenerated unstable isomers.
Concerning *fatigue resistance*, it must be reminded that this property is greatly influenced by the possible side reactions that remove population from the main isomerization [81].

$$B' \xleftarrow{\Phi_s} A \underset{\lambda_B,\Phi_{B\to A}}{\overset{\lambda_A,\Phi_{A\to B}}{\rightleftharpoons}} B \tag{5.2}$$

Even if the quantum yield (Φ_s) of the side reaction is small, the numerous cycles requested for the operation of the photoswitch determine a rapid decomposition of the initial isomer. Organic molecules are considered as some of the most promising candidates for the realization of most applications, but unfortunately they often undergo photo-induced degradation.
All the above mentioned properties of an ideal photoswitch must be studied and related to the potential energy profiles of the ground and low-lying electronically excited state of the two species (figure 5.2). The photo-induced isomerization is generally promoted by a nonadiabatic relaxation from the excited to the ground state through a conical intersection (CI). This deactivation channel determines the ultrafast sub-picosecond kinetic of the switching process.

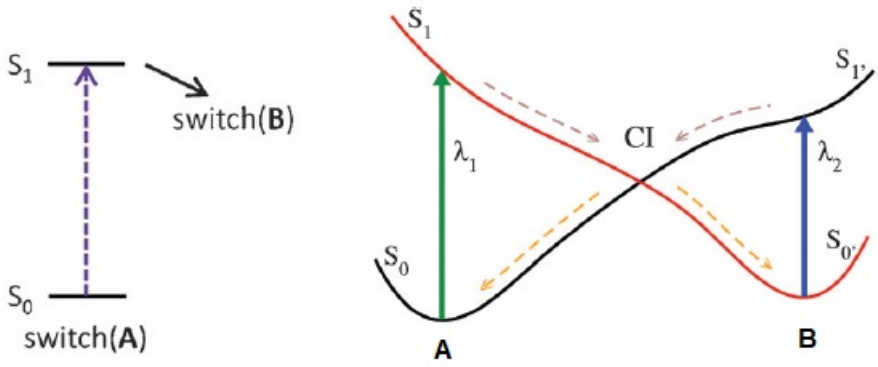

Figure 5.2: Representation of the switching isomerization process through single potential energy surfaces .

For an ideal P-type photoswitch, the two isomeric forms (A and B in figure 5.2) should absorb at different wavelengths, such as to make the forward and back reactions independently addressable. Optimal bistability of P-type photoswitches further requires that the two isomers are both stable in the ground state and separated by a large energy barrier (>1.0 eV) that obstacles the thermal interconversion [83].

After all these considerations, it becomes clear that the performance of each molecular photoswitch is strongly related to the microscopic processes leading the system from one isomer to the other. Therefore a clear understanding of the photoswitching mechanism, which possibly implies the characterization of all the reaction intermediates, is of fundamental importance. In many cases, the transient species involved in the reaction can be detected with ultrafast transient spectroscopy. The transient spectra may indeed provide quantitative and qualitative information about the chemical nature of the reaction intermediates, and about their formation and decay rate.
In our laboratories, we have studied the photoswitching mechanism of a family of hydrazone derivates that showed promising properties like high photochemical stability and excellent fatigue resistance. For the purpose we used transient absorption spectroscopy, both in the visible and infrared spectral regions.

5.2 Photophysical properties of photochromic hydrazones

The molecular structure of a generic hydrazone and the associated photoisomerization process is reported in Figure 5.3.

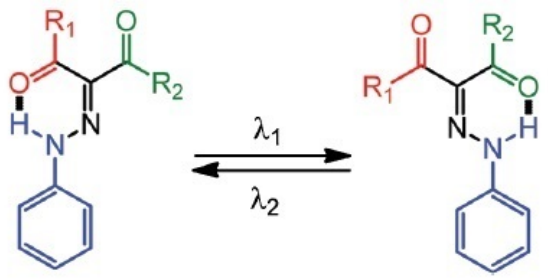

Figure 5.3: Photoisomerization of hydrazone derivatives following absorption of light.

Photochromic hydrazones present interesting properties, such as a simple and versatile synthesis, high quantum yields and high photostability. One of the main advantage of these molecules is the possibility of introducing substituents in different positions of the structure, greatly affecting their photoswitching properties. Recently, Shao et all. synthesized a series of bistable hydrazones and they characterized them using absorption and fluorescence spectroscopy [84]. Most of these molecules showed very good isomerization quantum yield and long thermal half-life, but some huge difference was observed among similar systems with different substituents. In the article [84], they reported the spectroscopic analysis of ten hydrazones switches, whose structure is presented in the top section of figure 5.4.

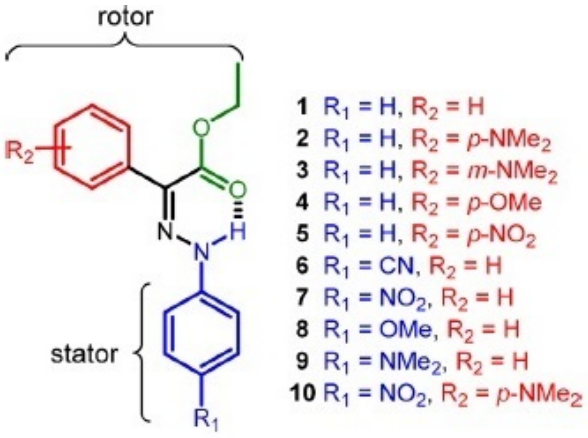

Figure 5.4: Scheme of all the photochromic hydrazone switches previously analysed [84].

The ten chromophores were designed starting from the general hydrazone structure reported in figure 5.3. In spite of a carbonyl group, these samples presents a phenyl ring linked to the CN double bond. This phenyl group is generally named as rotor, while the other phenyl ring linked to the N-N group is classified as stator. The rotorphenyl ring was chosen to avoid an hydrogen bond with the β N atom. That bond would have strongly stabilized the Z form, preventing easy conditions for the tans-cis transformation.
Different subtituents were applied on the rotor and stator phenyl groups in order to analyze their effects on photostationary state and quantum yield. Thanks to these structural modifications, this new family of hydrazones showed outstanding photochromic properties, first of all the slowest thermal half-lives among all con-

figurational photoswitches (2700 years) [85].
Among the most promising species of these ten hydrazones, in our laboratories we have applied static and transient spectroscopy to three of the ten substituted samples (figure 5.5), and we have analyzed the isomerization mechanism to uncover the structural origin of the observed properties.

Figure 5.5: Scheme of all the photochromic hydrazone switches previously analysed [84].

The three molecules we considered are:

1. *compound 7*, presenting a nitro group (NO_2) on the stator phenyl ring;
2. *compound 8*, with a methoxy group (OMe) attached to the stator phenyl ring;
3. the push- pull *compound 10*, characterized by the same nitro group as 7 but with a para-dimethyl amine (NMe_2) group as substituent on the rotophenyl moiety.

The spectroscopic characterization of these three systems was further extended trying to understand the influence of the solvent polarity on the deactivation pathway after the visible excitation. Recent TD-DFT calculations on similar hydrazone molecules [86] [87], highlighted that the out-of-plane C=N bond torsion leading to the formation of the E isomer is related to an N-N single bond rotation that assists the $Z \rightarrow E$ interconversion.We thus expect that the photo-product of this process is a mixture of different rotamers around the single bonds of the molecule. For this reason, we must specify that the assignments presented in the following descriptions assume that different rotamers of the E photo-product have similar spectral features and that the spectrum assigned to the single E-isomer is actually related to a mixture of rotamers.

5.2.1 Steady-state characterization

Shao et all. performed the static spectroscopic characterization of this new family of hydrazones (figure 5.4), but their analysis was limited to toluene as solvent [88]. In the following table 5.1, we report the photochemical properties already recorded of compound 7,8 and 10 in toluene [84].

Hydrazone	$\lambda_{abs}(nm)$		$\Phi(\%)$	$\Phi(\%)$	$PSS(\%)@\lambda_{irr}(nm)$		$\tau_{1/2}(year)$
	Z	E	$Z \rightarrow E$	$E \rightarrow Z$	E	Z	
7	391	366	35.3	11.4	98@442	82@365	1286
8	383	351	5.3	9.5	93@442	88@340	0.039
10	435	384	46.2	7.4	>99@480	96@375	126

Table 5.1: Photochemical properties of compounds 7,8 and 10 in toluene [84]

According to the results reported in table 5.1, some important and preliminary considerations can be made.
Compound 7 is characterized by very high photostationary states of the direct (98%) and reverse process (83%), probably due to the difference of about 25 nm between the maximum absorption wavelength of the two isomers Z and E. The quantum yield of the $Z \rightarrow E$ isomerization in toluene is also particularly high and the thermal half live ($\tau_{1/2}$) amounts to 1286 years.
Good PSSs values but moderate quantum yields and very low $\tau_{1/2}$ characterize compound 8. The addition of an electron donating group on the stator phenyl ring enhances the conjugation between the two sides of the molecule, reducing the double bond character of C=N bond together with the thermal back energy barrier.
The best performances were recorded for compound 10, which is the only push-pull molecule among the three systems. Visible light can be used to switch the Z form to the E form with an high quantum yield (46.2%). The Uv-visible absorption spectra of the E and Z isomers of hydrazone 10 in toluene are reported in Figure 5.6, together with the relative fluorescence spectra (figure 5.6).

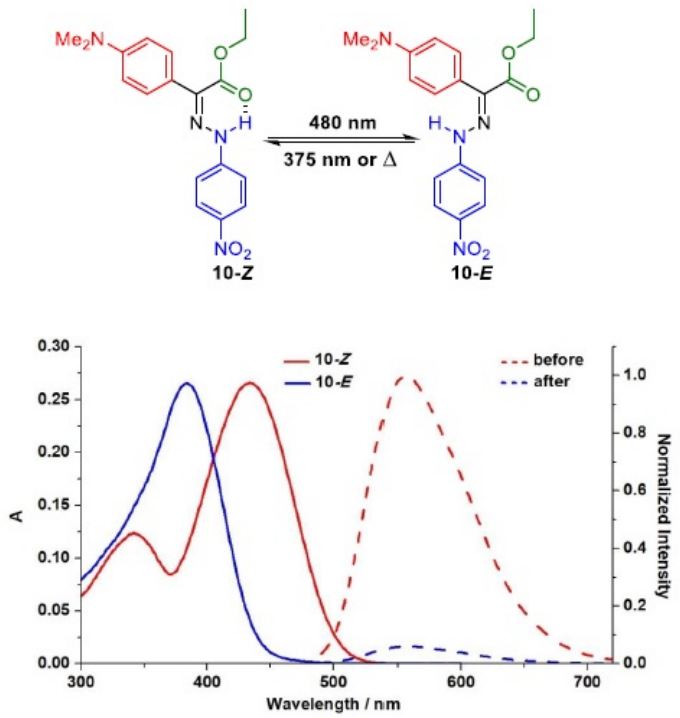

Figure 5.6: Solid lines: UV-Vis absorption spectra of 10-Z and 10-E in toluene; dashed lines: fluorescence emission spectra of 10 in toluene, before (red) and after (blue) switching at 480 nm [84].

Comparing the two dashed lines in figure 5.6, a huge reduction of fluorescence intensity upon isomerization is evident.

Considering all the results obtained in toluene, in this thesis we report all the emission and absorption spectra of samples 7,8 and 10 in toluene but also in other solvents of different polarity.
The following figure shows the absorption (panel a) and emission spectra (panel b) of compound 7 in toluene, dichloromethane and acetonitrile.

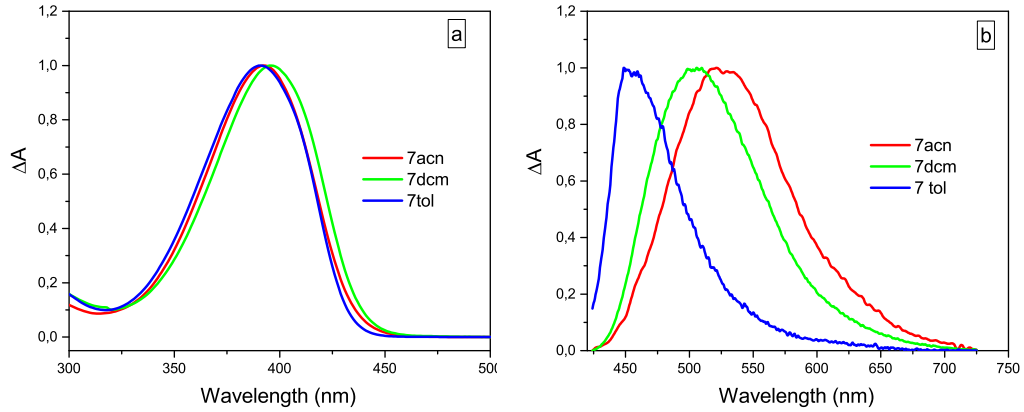

Figure 5.7: Absorption (panel a) and emission spectra (panel b) of compound 7 in acetonitrile (red line), dichloromethane (green line) and toluene (blue line).

The absorption spectra of compound 7 in the three used solvents are very similar. They are characterized by an intense band peaked at 390 nm, which only slightly red-shifts in dichloromethane. This solvent is not the most polar among the three solvents chosen for the study, but it is the most polarizable. The emission spectra of 7 reported in panel b are instead more influenced by polarity. The fluorescence band in toluene is peaked at 453 nm, in dichloromethane the band is red-shifted by 52 nm and peaked at 505 nm, and in acetonitrile it is red-shifted with respect to toluene by 72 nm and peaked at 525 nm. This strong influence of solvent polarity can suggest the presence of a CT emissive state.

Absorption and emission spectra of compound 8 are reported in figure 5.8.

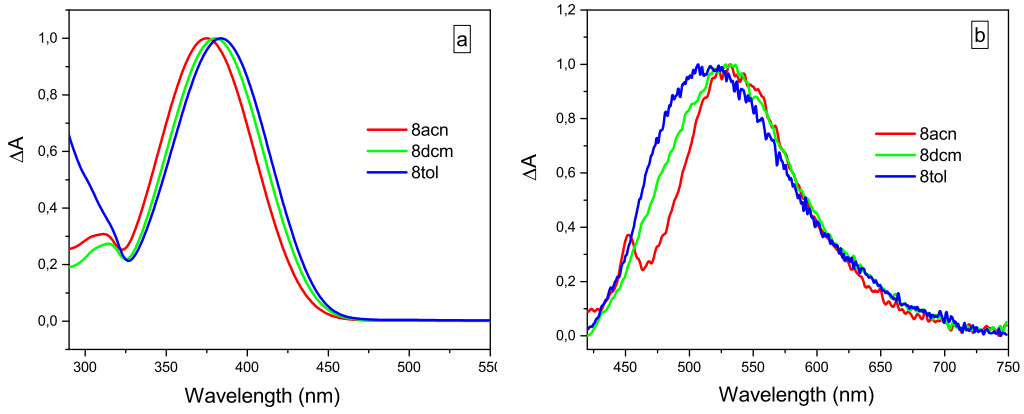

Figure 5.8: Absorption (panel a) and emission spectra (panel b) of compound 8 in acetonitrile (red line), dichloromethane (green line) and toluene (blue line).

The absorption spectra of compound 8 (panel a) are characterized by an intense band peaked around 380 nm and they show a progressively limited blue-shift with the increasing of solvent polarity. In the polar acetonitrile, the band is centered at 376 nm, while in dichloromethane it is red-shifted by 4 nm (380 nm) and

in nonpolar toluene by 8 nm (384 nm). The polarity effect on the fluorescence bands of compound 8 (panel b) is less pronounced than for compound 7, but in both dichloromethane and acetonitrile fluorescence appears red-shifted with respect to toluene (514 nm) of nearly 20 nm (peaked at 531 nm).

Finally, Figure 5.9 reports the absorption and fluorescence spectra of compound 10. Considering the strong effect of solvent polarity and polarizability on the emission spectra, we decided to extend the study of this compound to five different solvents.

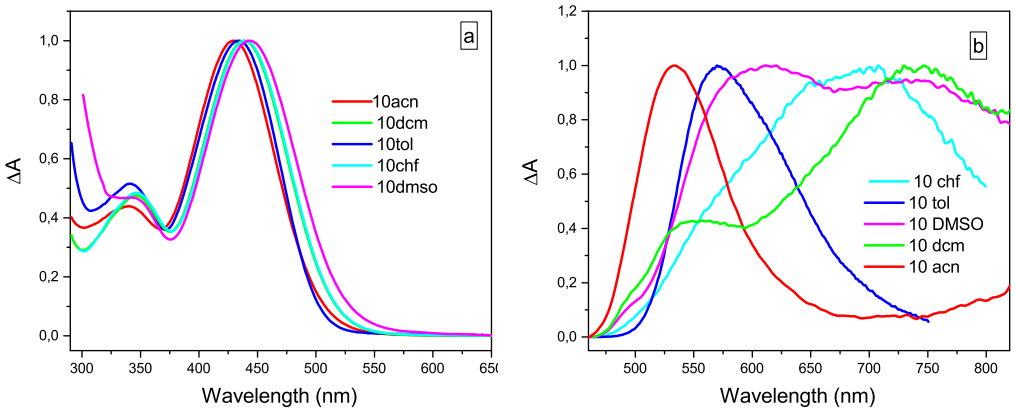

Figure 5.9: Absorption (panel a) and emission spectra (panel b) of compound 10 in acetonitrile (red line), dichloromethane (green line), toluene (blue line), chloroform (cyano line) and dimethyl sulfoxide (violet line).

The absorption spectra of compound 10, reported in panel a, show a little dependence on solvent polarity/polarizability with a slight red-shift of the absorption maximum in dimethyl sulfoxide and chloroform (the two more polarizable solvents). The effect on the emission bands instead appears very important. DMSO, dichloromethane and chloroform are the most polarizable solvents and they highly influence not only the central wavelength of the emission band but also its shape. In fact, looking at the spectra reported in Figure 5.9, it appears that two separated bands contribute to the emission of the molecule, whose relative intensity and peak position highly depend on the solvent. The observation of a second band seems to correlate with both the polarity and polarizability of the solvent. Indeed in toluene, the less polar among the analyzed solvents, a single emission band is observed peaked at 571 nm. In acetonitrile, a polar but not polarizable solvent, a main emission band is observed peaked at 533 nm and blue shifted compared to that recorded in toluene, but a second less intense peak very red shifted ($>$ 750 nm) is also noticed. In dichloromethane a double peak is clearly observed, with a less intense band in the blue part of the spectrum (peaked at 550 nm) and a more intense band at 740 nm. Two bands with similar intensities are also observed in DMSO, peaked at 616 nm and 745 nm. Finally, only one very broad band is observed in chloroform, peaked at 681 nm.

All the three samples were studied also with static infrared spectroscopy. Figure 5.10 shows the FTIR spectra of compound 7 and 10 in both acetonitrile and

dichloromethane . In order to assign the observed bands to specific vibrational modes, FTIR spectra were also simulated with density functional theory. The group of professor M. D. Liptak of the University of Vermont performed the DFT calculations in the gas phase. Actually, they also performed the same calculation adding dichloromethane solvent contribution but differences between the computed and experimental IR spectra seemed to increase. This was much evident in the vibrational frequency of the NO_2 stretching mode that shifted to even lower frequencies. Reasons for this are often related to a combination of temperature effects in the experimental data and limitations of the harmonic oscillator model. A comparison between the computed and experimental FTIR spectra of compound 10 is reported in panel c, with frequency assignments made by visualizing the normal modes using the chemcraft software.

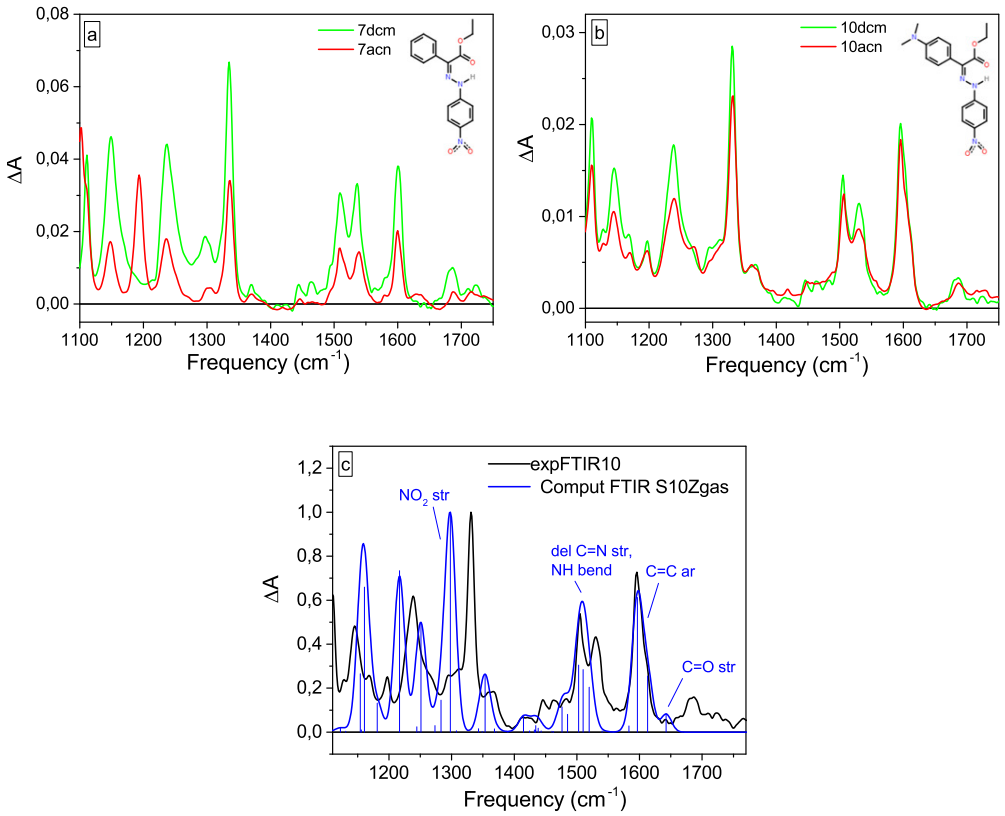

Figure 5.10: FT-IR spectra of compound 7 (panel a) and 10 (panel b) in dichloromethane (green line) and acetonitrile (red line). Panel c shows the comparison between the DFT computed FTIR spectra of compound 10 in the gas phase and the experimental one in dichloromethane with the assignment of the principal vibrational normal modes.

The spectra of compounds 7 and 10 in the 1200-1800 cm^{-1} region are very similar and the assignment of their active vibrational normal modes can be referred to the computed FTIR reported in panel c (blue trace). The characteristic C=O stretching mode of both the samples appears experimentally centered at 1680-1700 cm^{-1}, even though computed frequencies for this mode results underestimated, locating it at about 1650 cm^{-1}. The band at 1600 cm^{-1} is assigned

to the aromatic C=C stretching, while the double peak around 1520 cm^{-1} is assigned to a delocalized mode involving the C=N, N-N, NH bonds. According to calculations, for compound 10 the most intense contribution from C=N stretching is at 1502 cm^{-1}. The band at 1340 cm^{-1} can be ascribed to the NO_2 stretching that DFT calculates at lower frequencies (1300 cm^{-1}). The intense band below 1200 cm^{-1} is probably due to the C-O stretching conjugated with the C=O double bond.
The assignments for compound 8 are similar, but obviously the NO_2 stretching band is not present. Panel a of figure 5.11 reports the comparison between the experimental spectrum of compound 8 in acetonitrile and dichloromethane, while panel b shows the comparison between the FTIR computed spectrum and the spectrum recorded in dichloromethane.

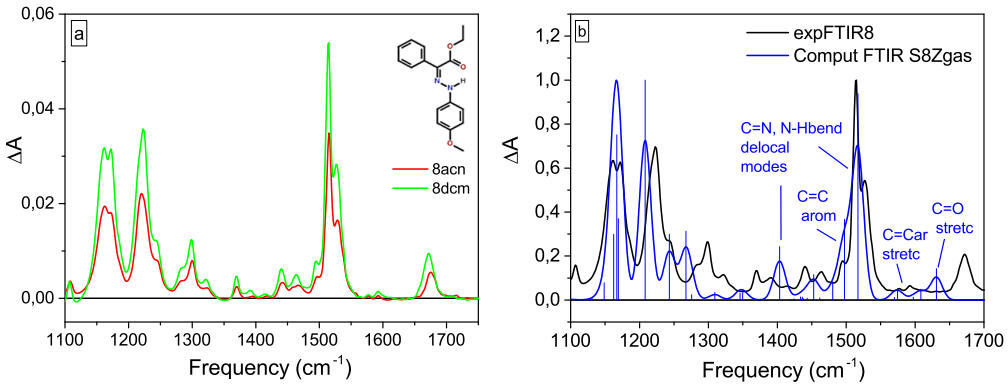

Figure 5.11: FT-IR spectra of compound 8 (panel a) in dichloromethane (green line) and acetonitrile (red line). Panel b shows the comparison between the DFT computed FTIR spectra of compound 8 in gas phase and the experimental one in dichloromethane with the assignment of the principal vibrational normal modes.

It is evident that, also in this case, the C=O stretching band computed in the gas phase is underestimated at 1640 cm^{-1}, in contrast with the experimentally measured centered at 1680 cm^{-1} (panel b). In the infrared spectra, aromatic C=C stretching generally shows two couples of bands at 1600 cm^{-1} and 1450 cm^{-1}. In this case, differently from compound 7 and 10, the more intense band assigned to C=C stretching of compound 8 is that at 1490 cm^{-1}, closed in frequency to the C=N stretching mode. Indeed these two modes contribute to the intense double peaked band around 1510 cm^{-1}.

5.2.2 Uv-visible transient characterization

All the transient absorption spectra have been recorded upon excitation of the sample at 400 nm. Compound 10 has been studied also with excitation at 450 nm to avoid the excitation of the E isomer. All measurements have been performed in acetonitrile, dichloromethane and toluene with the aim of understanding the influence of solvent polarity on the isomerization process.
The global analysis software Glotaran was used to analyze the dynamic evolution of the excited states of the molecules. Evolution Associated Difference Spectra were extrapolated using a sequential scheme to outline the deactivation pathway.

Compound 7

The transient spectra and relative EADS for compound 7 in the three solvents are reported in Figure 5.12.

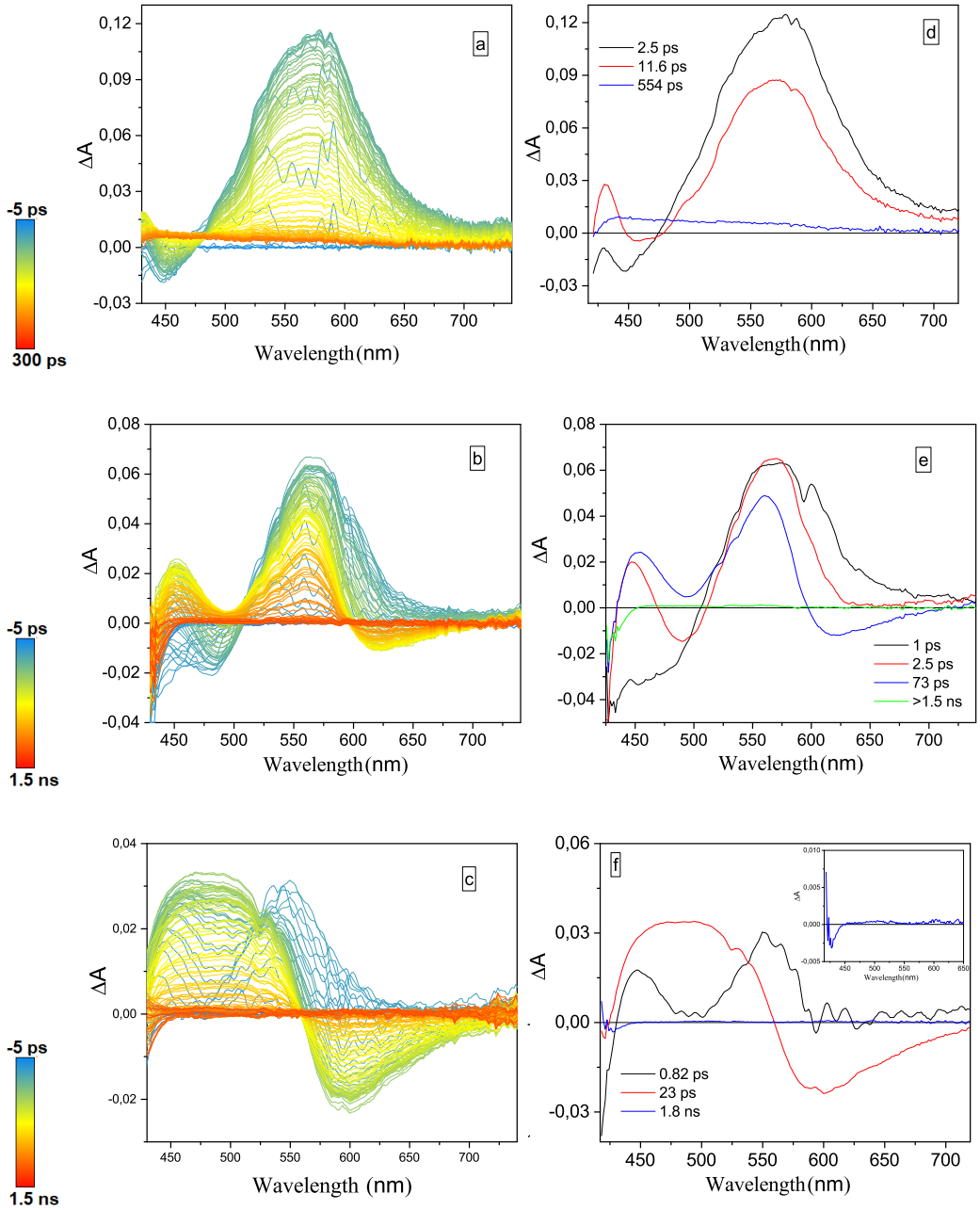

Figure 5.12: Transient absorption spectra and Evolution Associate Difference Spectra of compound 7 excited at 400 nm in toluene (panel a and d), dichloromethane (panel b and e) and acetonitrile (panel c and f); panel f reports the inset of the final EADS.

Transient spectra of compound 7 in toluene are characterized by an intense positive broad ESA band centered at 570 nm. A stimulated emission band (SE) is

also observed, peaked at 450 nm, in agreement with the steady state fluorescence recorded for the Z form (figure 5.7). The ground state bleaching band is not visible because it is covered by the scattering of the pump at 400 nm. All the spectrum decays very fast, with a broad weak residual band peaked at 450 nm observed at long pump-probe delays.
The EADS retrieved from the global analysis are reported in panel d. In about 2.5 ps (evolution from the black to red EADS in panel d) the stimulated emission signal mostly recovers, and the residual emission undergoes a red-shift of about 20 nm, while the ESA intensity at 570 nm slightly decreases. The partial recovery of the emission band could signal the occurrence of isomerization, however the persistence of an intense ESA band indicates that most of the population still resides on the excited state of the Z form at this timescale. In the following evolution towards the final EADS (11.6 ps, from red to blue line in panel d), the ESA band peaked at 570 nm completely recovers and it is replaced by a very broad band with small residual intensity. This band decays on a longer timescale than that of our measurement (300 ps), as noticed by plotting the kinetic trace at 440 nm (Figure 5.13).

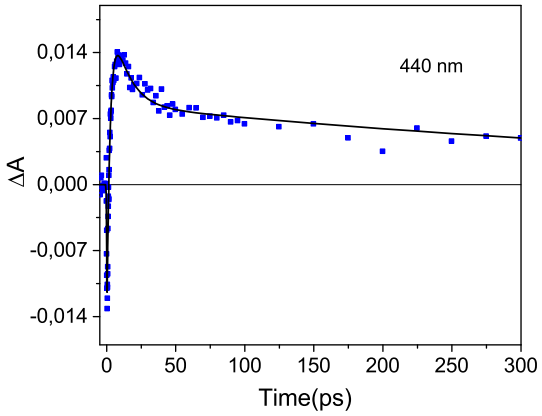

Figure 5.13: Kinetic trace at 439 nm of compound 7 in toluene.

This band could result from the absorption of the E photoproduct which reaches the ground state with an excess of energy. The small intensity of the residual signal could suggest a lower isomerization QY with respect to that measured ($Z \rightarrow E$ of 35%), indicating that most of the population comes back to the Z ground state by internal conversion. Information about isomerization QY however is not directly accessible from this measurement, being the bleaching region of both the Z and E isomers not directly observable and being the absorption cross section of the hot isomers unknown. Figure 5.14 reports a simplified representation of the excited states of compound 7 in toluene, depicted thanks to the information collected with transient spectroscopy.

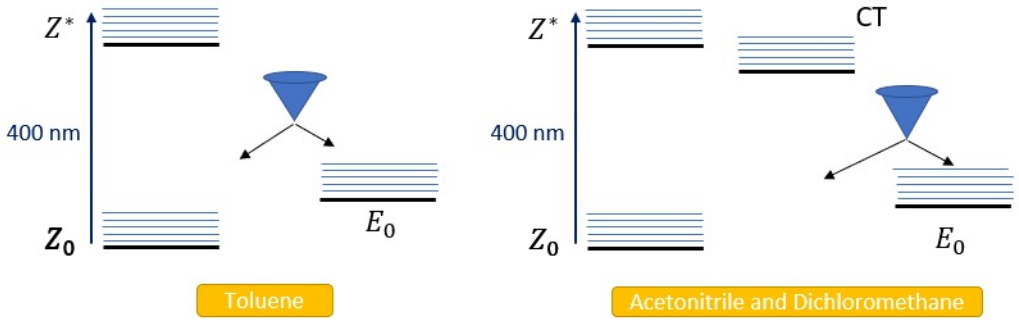

Figure 5.14: Simplified Jablosky diagram of compound 7 in toluene, acetonitrile and dichloromethane.

At short time delays, the transient spectra in acetonitrile (panel c) present a broad intense ESA band spanning from 430 to 600 nm, with a superimposed contribution of the stimulated emission band of the Z form, appearing as a deep peaked at 500 nm. The transient spectrum rapidly evolves: the stimulated emission at 500 nm recovers and it is replaced by a broad red-shifted positive band, with a new stimulated emission rising at 600 nm. This evolution is better visualized looking at the EADS extrapolated by the global analysis (panel f). In the initial EADS (black line) a ground state bleaching band is noticed at the very blue edge of the probed spectral window. It almost recovers in less than 1 ps, being replaced by the positive ESA band peaked at 480 nm (evolution from black to red trace). The evolution of the ESA band, which significantly changes in shape in about 0.8 ps, and the appearance of the stimulated emission band peaked at 600 nm, imply that a different excited state is populated on this fast timescale.
Very recently Mravec et al. reported the transient absorption spectra of hydrazone compounds showing some similarities with those studied in this work [86] and they interpreted their measurements based on DFT computations. One of their compounds presents transient absorption spectra and temporal evolution very similar to that described here for compound 7 in acetonitrile. These authors assign the early time component, which appears very similar to those obtained for compound 7, to the absorption of the Frank-Condon minimum of the S1 state of the Z isomer (FC S1-min state). On the following timescale they observe a spectral evolution again similar to that described for 7, characterized by the development of a new red-shifted stimulated emission band. This evolution has been associated to the relaxation towards a second emissive minimum (Z-S1-min) on the Z potential energy surface, close to the conical intersection leading to isomerization toward the E form (CI). In this minimum the sample assumes a near-perpendicular geometry, presenting an electronic distribution typical for a charge transfer state, which is in agreement with the observed red-shifted emission.
Considering the great similarity of the transient spectra measured for compound 7 in acetonitrile with those reported by Mravec et al., we can interpret the observed evolution in a similar way. The evolution from the black to red EADS (panel c of figure 5.12) can be interpreted in terms of the decay of the localized FC S1-min state populated upon light absorption, towards a charge transfer state Z-S1-min, occurring within 800 fs. In the following evolution towards the blue EADS, most of the ESA and stimulated emission recover, signaling that the majority of the

excited state population returns to the ground state of the Z isomer through internal conversion, on a timescale of 20 ps. The small residual signal in the blue EADS, in analogy to what already observed by Mravec et al., can be associated to the absorption of the E isomer ground state. Its low intensity suggests a strongly reduced isomerization in this solvent and it does not let us acquire the hot state relaxation kinetic described by Mravec. Figure 5.14 reports the simplified energy scheme that can be depicted for the excited states involved.

Compound 7 has also been studied in dichloromethane and its transient spectra are reported in panel b. The spectral shape observed at early time, reminds that recorded in toluene, but the ESA band appears less broad and slightly blue-shifted. Also, a double peaked broad negative band representing the convolution of bleaching and stimulated emission is observed at short delay times. The stimulated emission band is initially peaked at 480 nm, and recovers on a few ps timescale. The Evolution Associated Difference Spectra are reported in panel e. The initial black trace, represents the FC state reached upon excitation. In the evolution towards the second EADS, occurring in about 1 ps, we observe a red shift of the SE band with the development of a positive ESA band that partially superimposes to it. Furthermore the intense ESA peaked at 550 nm narrows and slightly blue shifts. This evolution can be interpreted in terms of a fast excited state relaxation, possibly promoted by the solvent, bringing the system out from the FC region. In the following evolution towards the blue EADS, occurring in 2.5 ps, we observe a partial decay of the ESA bands, a recovery of the stimulated emission band peaked at 480 nm and the development of a new red-shifted stimulated emission peaked at about 620 nm. This evolution is similar to that already observed in acetonitrile, and it can thus be associated to the relaxation towards an excited state with charge transfer character. Differently from acetonitrile however, in this case the decay towards the CT state seems not complete, but only partial. It appears that in this moderately polar solvent an equilibrium is established between the initially populated local excited state and the CT state on a 2.5 ps timescale. The excited state mostly recovers on the following 73 ps timescale (evolution from the blue to the green EADS) leaving a very small residual signal and implying a very low Z to E isomerization quantum yield also in dichloromethane.
The formation of a CT state for compound 7 could be already inferred by considering the dependence of its fluorescence band from the solvent polarity (figure 5.7). Indeed, a red shift of the fluorescence is observed when passing from toluene to dichloromethane and acetonitrile. In the more polar solvents the fluorescence band is very broad and extends up to the red, possibly including the emissive contribution from both the localized and the CT state.

Compound 8

We then studied compound 8 with transient spectroscopy in the three solvents toluene, dichloromethane and acetonitrile. The acquired transient spectra and the EADS obtained with global analysis are reported in Figure 5.15.

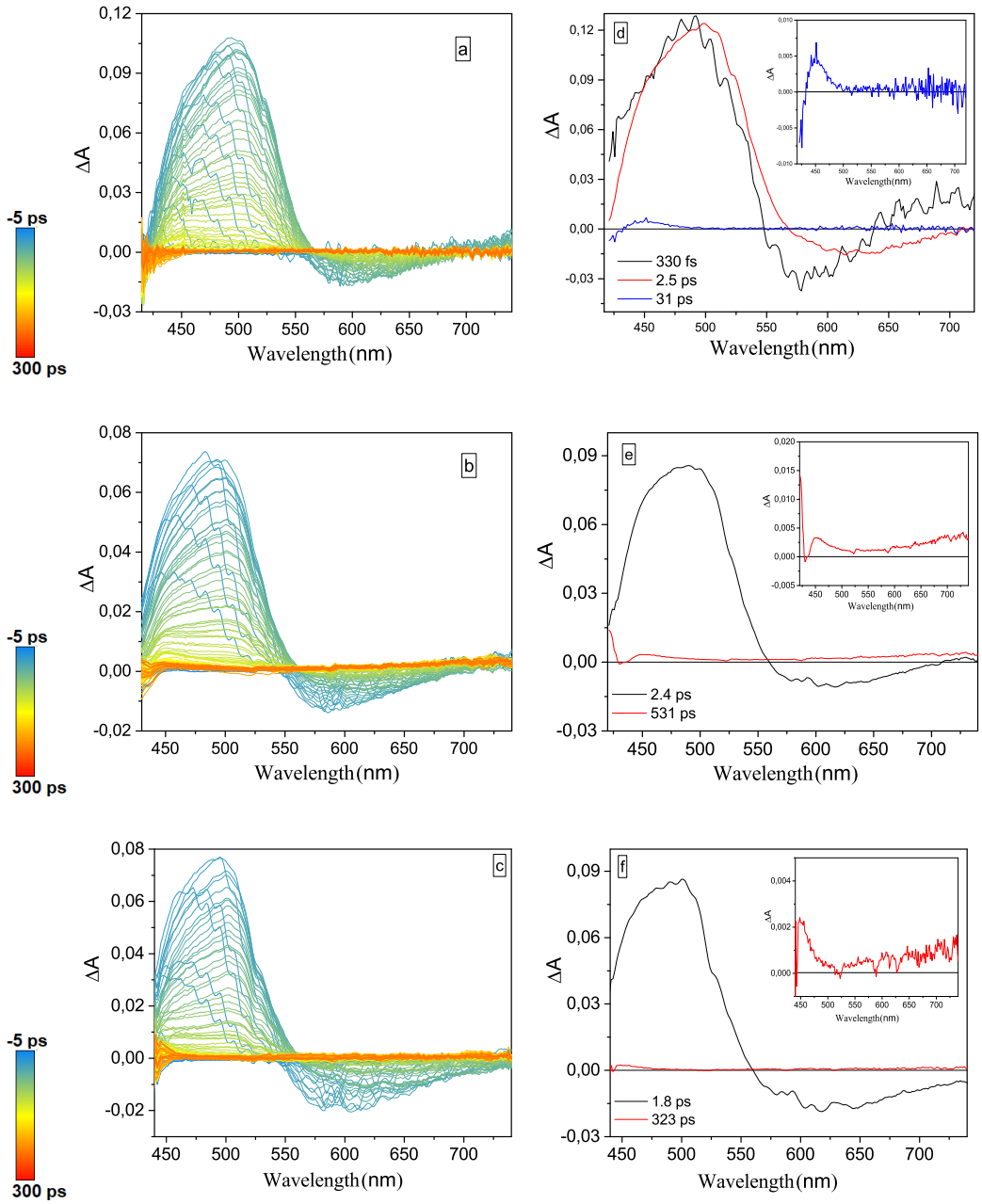

Figure 5.15: Transient absorption spectra and Evolution Associate Difference spectra of compound 8, excited at 400 nm, in toluene (panel a and d), dichloromethane (panel b and e) and acetonitrile (panel c and f); panel d, e and f also reports the inset of the final EADS.

The appearance of the transient spectra is very similar in all the three solvents. In all cases an intense positive band associated to an excited state absorption is observed, peaked around 480 nm, and a negative band of stimulated emission is noticed at 600 nm. In all cases the excited state features (in particular the intense ESA band) recover within a few picosecond, with the faster excited state deactivation in acetonitrile (1.8 ps, compared to about 2.5 ps in the other two solvents). In all the cases the bleaching band is covered by the scattering of the

pump at 400 nm and it is not visible in the spectra.
The spectral shape observed for this compound in all the solvents is very similar to that registered for compound 7 in acetonitrile for pump-probe delays >1 ps. In case of compound 7, both the ESA and stimulated emission bands observed at >1 ps delay were assigned to an excited state with a charge transfer character. In case of compounds 8, it appears that this state is directly populated in all solvents, independently on polarity.
In both acetonitrile and chloroform, the bands associated with the excited state decay in about 2-2.5 ps (evolution from black to red EADS), leaving a very small positive residual signal. This positive signal can be assigned to the ground state absorption of the E isomer, thus signaling the occurrence of isomerization. The red trace decays within 300 ps in acetonitrile and 500 ps in dichloromethane, indicating that the E ground state pertains on this timescale. Also in this case if judged from the intensity of the residual signal, the isomerization QY appears low, implying that most of the population relaxes to the original Z conformation by internal conversion.
Figure 5.16 shows the simplified scheme of the excited states of compound 8 in all the three solvents based on transient absorption results.

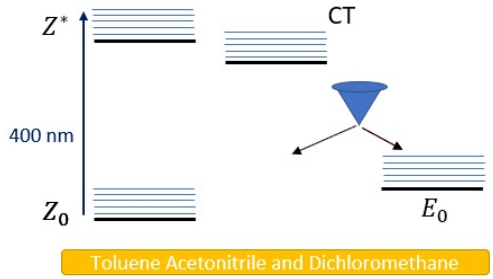

Figure 5.16: Simplified Jablonski diagram of compound 8 in all the three solvents.

In toluene, the excited state evolution is quite similar to that observed in the more polar solvents. Although, an initial fast relaxation of CT state can be observed to occur in about 300 fs. Also in this case the system reaches the conical intersection in 2.5 ps, with most of the population decaying back to the original Z conformation (see diagram in figure 5.16). Only a small part of population deactivates to the the E form, in agreement with the low measured $\Phi_{Z\rightarrow E}$ (5%). In fact, also in this case the final blue EADS has a very low intensity that recovers in about 30 ps, signaling the complete relaxation toward the ground state of Z form.

Compound 10

The transient spectra measured for compound 10 are reported in figure 5.17, and they show a notable dependence from solvent polarity. The excitation wavelength has been set to 450 nm in case of dichloromethane and acetonitrile, while in toluene the sample was excited at 400 nm. We also repeated the measurements in toluene upon excitation at 450 nm, obtaining comparable results in the two cases. Transient spectra and EADS are reported in Figure 5.17.

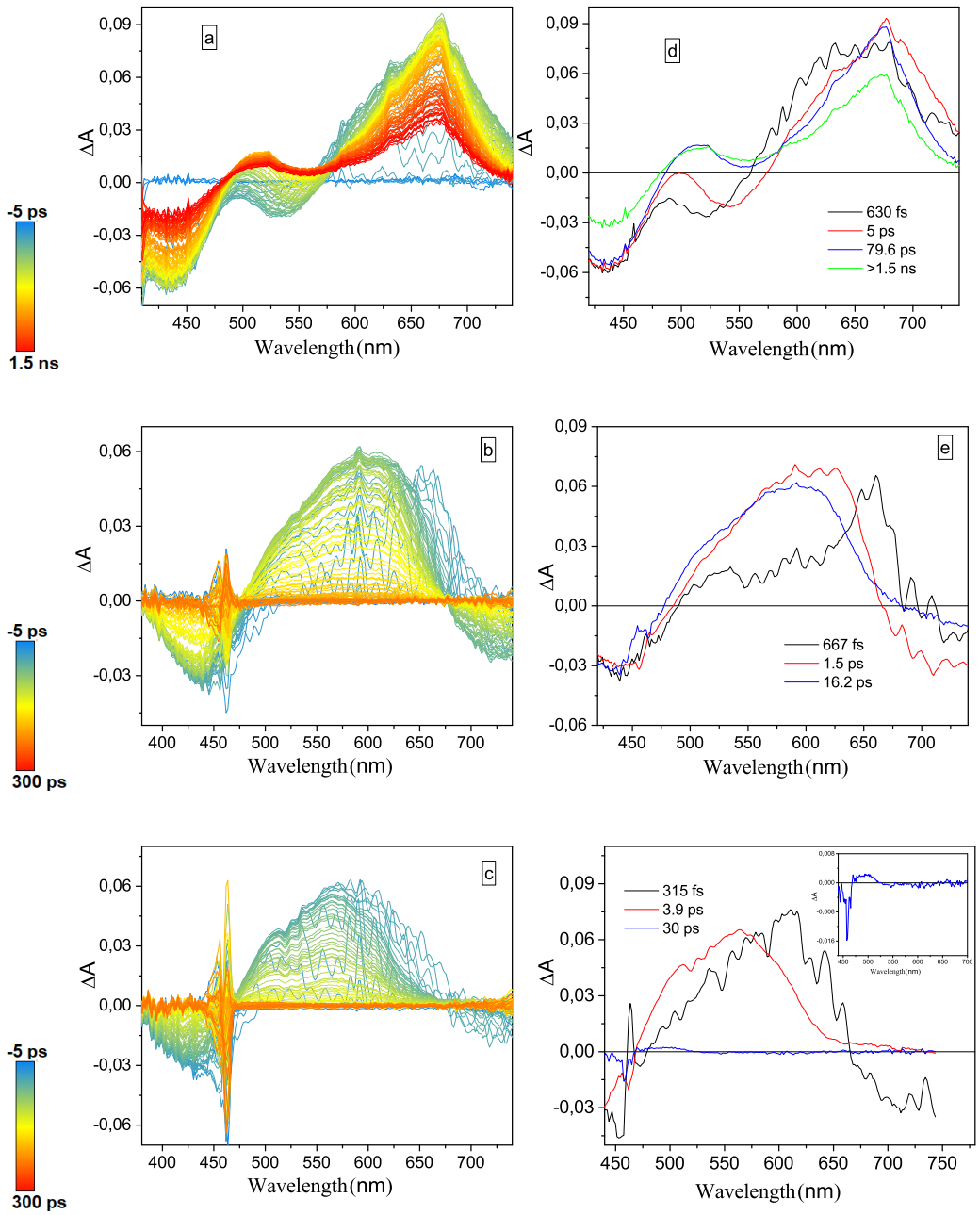

Figure 5.17: Transient absorption spectra and relative Evolution Associate Difference spectra of compound 10 respectively in toluene with excitation at 400 nm (panel a and d), dichloromethane (panel b and e) and acetonitrile (panel c and f) both excited at 450 nm; panel f also reports the inset of the final EADS.

The transient spectrum of compound 10 recorded in toluene and reported in panel a shows a ground state bleaching band clearly visible for this sample. Its absorption is substantially red shifted compared to the previous ones, because of the presence of substituents on both the rotor and stator moieties conferring it a push-pull character. The spectra furthermore show a stimulated emission band centered at 550 nm and a broad ESA band peaked at about 670 nm. Looking at the EADS reported in panel b it is noticed that the evolution occurring in 630 fs,

(transition from black to red EADS) mostly consists in a red shift of the SE band, that can be associated to a vibrational and/or solvent induced cooling. After 5 ps, the SE band recovers, possibly indicating the occurrence of isomerization. Indeed, the increase of positive signal in the 500-550 nm region could be ascribed to absorption from the E isomer ground state. In the following evolution (blue to green EADS), occurring in 80 ps, part of population returns back to the Z ground state, as noticed from the decrease of the GSB signal of the Z form. We also observe a partial recovery of the ESA band peaked at 670 nm, associated both to excited state decay and isomerizarion. The transient signal does not recover within the timescale of the measurement, signaling that the photoproduct has a lifetime $>$ 1.5 ns and part of the Z form decays by emitting fluorescence ($\Phi_{fl} = 22.6\%$, [84]).

Transient spectra of compound 10 in the two more polar solvents with excitation at 450 nm are very similar. In both cases, the transient spectra are characterized by a broad ESA band peaked at about 550 nm and a negative signal assigned to ground state bleaching peaked at about 450 nm. A red-shifted SE band, also visible in the static fluorescence spectra (figure 5.9), appears at early times at 700 nm, partially covered by the broad ESA band. The transient signal recovers quite fast (about 4 ps in acn and 16 ps in dcm), leaving a very small residual signal on the long timescale.
The EADS retrieved from the data analysis are reported in panel e and f. The first EADS in dichloromethane (black line in panel e) presents a sharp peak at about 650 nm, which reminds the ESA band observed in toluene, and assigned to a localized excited state, with a broad tail extending from 500 to 600 nm. The broad tail of the ESA could results from a contribution of the CT state, implying that at the short timescale both excited states are partially populated, possibly because the transition between the localized and CT states is ultrafast. Observing the second EADS (red line) it appears that in 650 fs all the population decays to the CT state, characterized by a bleaching band at 440 nm, a broad ESA band centered at 600 nm and a SE band visible at wavelengths $>$700 nm. The emission band then recovers within 1.5 ps (evolution towards the blue EADS) possibly because of partial isomerization. However, considering the intensity of the ESA band, most of the population is still in the excited state while its narrowing suggests a relaxation of the excited state. After 16 ps the signal recovers with most of the population returning to the Z-GS.

In acetonitrile the evolution is similar. In this case the formation of the CT state appears even faster, since this state is directly detected upon photoexcitation. Indeed the initial EADS already presents a negative SE band at wavelengths $>$700 nm and a broad ESA peaked at about 600 nm, besides the bleaching band at 430 nm. The SE band recovers in 315 fs, possibly signaling the occurrence of partial isomerization and at the same time the ESA band slightly blue shifts because of vibrational relaxation of the excited state. The residual signal (blue trace) observed in the final component presents a very small absorption band peaked at about 500 nm, assigned to the ground state of the E form. This state relaxes in about 30 ps. Considering the low intensity of the signals assigned to the E form, we conclude that also in this case the isomerization QY is quite low, so that most of the final population reverts directly to the initial ground state of the Z isomer by internal conversion.

The comparison of the kinetic constants describing the relaxation of the three samples in the polar and non polar solvents is useful to compare the influence of the molecular structure and of solvent polarity on the overall deactivation pathway. Table 5.2 reports all the time constants obtained from the analysis of the transient absorption spectra recorded in the UV-Visible range.

Compound	Solvent	τ_1	τ_2	τ_3	τ_4
7	TOL	2.5 ps	11.6 ps	554 ps	
	DCM	1 ps	2.5 ps	73 ps	$>$ 1.5 ns
	ACN	0.82 ps	23 ps	1.8 ns	
8	TOL	330 fs	2.5 ps	31 ps	
	DCM	1.8 ps	323 ps		
	ACN	2.4 ps	531 ps		
10	TOL	630 fs	5 ps	79.6 ps	$>$1.5 ns
	ACN	667 fs	1.5 ps	16.2 ps	
	DCM	315 fs	3.9 ps	30 ps	

Table 5.2: Decay times observed in the UV-Vis transient spectra for all the three compounds 7, 8 and 10 in the different solvents.

Looking at the results reported in table 5.2, one important consideration that must be added is that all the molecules in mainly all the solvents decay before the nanosecond time range. Therefore, even if for these compounds the inter-system crossing cannot be excluded, we can say that the deactivation through a triplet state appears quite unfavoured. The longest constants can be found for compound 7 in dichloromethane and compound 10 in toluene. However, the intensity of the final EADS of compound 7 living beyond the time interval of the measurement appears quite low, so an important contribution of ISC is almost excluded. In case of compound 10 in non polar solvents the involvement of triplet states can't be completely excluded, but the relatively high fluorescence QY of this compound suggests that this deactivation channel has not a prominent role also in this case.

5.2.3 Visible pump-Infrared probe transient spectroscopy

The photophysics of the three hydrazones 7,8 and 10 has been further investigated with Vis-pump/MidIR-probe spectroscopy. The excitation wavelength has been set at 400 nm for samples 7 and 8 and at 450 nm for sample 10, while the IR probe pulse covered the 1200-1800 cm^{-1} region.
Infrared transient spectra are very important to characterize the dynamic evolution of samples during the electronic states deactivation, being the IR region much more sensitive to the structural and conformational modifications of a molecule. The combined information obtained from the analysis of visible and IR time resolved spectra can result in a more detailed picture of the system photodynamics. As already done in case of visible pump-probe spectra, the transient IR (TRIR) data were analyzed using global analysis and a linear sequential decay scheme.

Compound 7

The Evolution Associated Difference Spectra of compound 7 in acetonitrile (panel a) and dichloromethane (panel b) are reported in Figure 5.18.

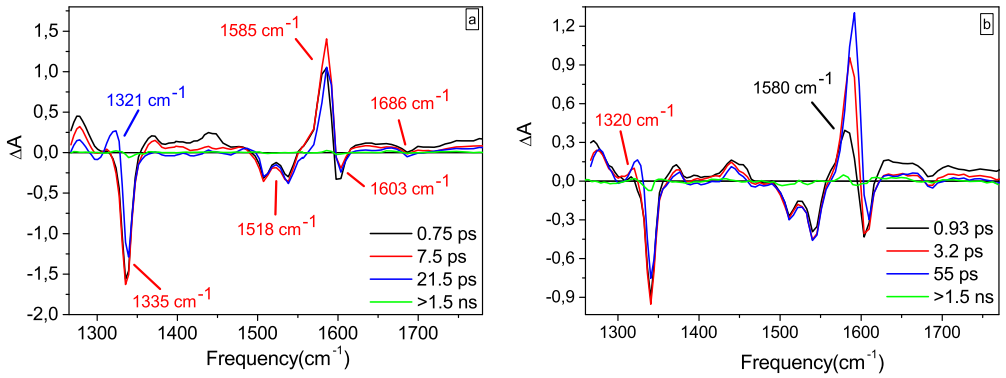

Figure 5.18: EADS obtained from global analysis of the time resolved IR data collected for compound 7 in acetonitrile (panel a) and dichloromethane (panel b).

The initial spectral component obtained by analyzing the data recorded in acetonitrile upon irradiation (black trace, panel a) shows negative bands corresponding to the bleaching signals of the ground state absorption of the Z isomer. Their assignment has been previously presented based on the comparison with DFT computations (see steady state FTIR spectra reported in figure 5.10). Among the bleaching bands, we can distinguish the stretching of NO_2 group at 1335 cm^{-1}, a double peaked band at 1507-1538 cm^{-1}, assigned to a delocalized mode involving C=N, N-N stretching and N-H bending, a band relative to the aromatic C=C stretching at 1603 cm^{-1} and finally a weak band associated with the C=O stretching at 1686 cm^{-1}. Excited state positive absorption bands are instead observed at 1277 cm^{-1}, at 1367 cm^{-1} and 1438 cm^{-1}, together with an intense band at 1585 cm^{-1} and two broad weak bands around 1622 cm^{-1}.
The initial spectral component evolves into the following one (red trace) in 750 fs. A slight intensity decrease is observed for all the absorption bands, that can be associated with a relaxation of the S1 state. However, at the same time the intensity of the absorption band at 1585 cm^{-1} slightly increases and red shifts. On this same timescale, the analysis of visible pump-probe data evidenced the formation of an excited state with CT character (800 fs). In case this state could be classified as a twisted intramolecular charge transfer state (TICT), it would be expected that the molecule would assume a nearly orthogonal geometry with a consequent H-bond breaking. The breaking of this bond would then result in an increase of localization of both the C=O and C=N modes (up-shift). If this is the case, the positive band at 1585 cm^{-1} in panel a could be associated with an upshifted frequency of the C=N bond and the very small positive band at 1698 cm^{-1} to the upshifted C=O bond. Moreover, inspection of the computed DFT IR spectrum of the E isomer, where in a similar way both H-bond breaking and increase of C=N bond length are expected, confirms that following these structural changes the C=N stretching frequency indeed up-shifts. A slight downshift of the aromatic C=C vibrational mode absorption is also expected.

Summing up the experimental evidence obtained from ultrafast measurements in both visible and IR spectral range, it can be so suggested that the state reached 800 fs after excitation has a CT nature and a distorted geometry, characterized by a twisting around the central C=N bond, which is preparatory for isomerization to occur.
In the following evolution in the EADS recorded occurring in 7.5 ps, all the absorption bands slightly decrease in intensity, except for a new positive band at 1321 cm^{-1} which rises, partially superimposing to the nearest bleaching band at 1335 cm^{-1}. The transient spectrum mostly decays in 21.5 ps leaving a very small residual signal (green line), in agreement with what was observed also with visible pump-probe measurements (see panel f figure 5.12). The evolution occurring on the 20 ps timescale can thus be related to the reaching of the conical intersection, leading to both isomerization and relaxation of the unconverted Z fraction to its ground state (see diagram in figure 5.14). The reduced intensity of the E-Z absorption difference spectrum (green EADS) confirms a low quantum yield for the $Z \rightarrow E$ isomerization process.

The EADS extrapolated from the spectra measured in dichloromethane (panel b) are quite similar to those obtained in acetonitrile and the observed peaks can be assigned in a similar way. In the first picosecond after light absorption, the intense positive band peaked at 1580 cm^{-1} increases in intensity and red shifts by 3 cm^{-1}. As previously discussed, this band can be related to the upshift of the C=N stretching mode, following the structural distortion of the molecule. This evolution can be so assigned to a vibrational relaxation of the S1 state, but also to a first partial evolution towards the CT state that is not distinguishable in the visible analysis.
In the following evolution, occurring in 3 ps (evolution from the red to blue EADS) the two bands at 1320 cm^{-1} and 1580 cm^{-1} increase and red-shift, implying a further population of the CT state. The intensity all over the spectrum recovers in 55 ps, leaving a very small residual signal (green line), that lives beyond the time interval of the measurement. Also in this case, excited state relaxation is observed to occur on a similar timescale (50-70 ps) as retrieved from visible pump-probe experiments.
In order to confirm the occurrence of isomerization, we have measured the FTIR spectra of the E form of compound 7 in dichloromethane obtained upon prolonged irradiation of the Z form (few hours). An UV/VIS absorption spectrum has been measured to confirm both photoconversion and the reaching of the PSS. The comparison between the final EADS and the E-Z FTIR spectrum is shown in figure 5.19.

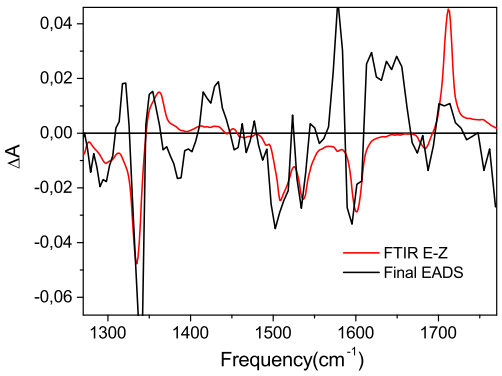

Figure 5.19: Comparison between the E-Z FTIR spectrum (red line) and the final EADS obtained from global analysis of the time resolved IR data collected for compound 7 in dcm.

The comparison reveals a good agreement, even if several positive bands are not observed in the FTIR spectrum. This could be caused by the fact that in the FTIR spectrum the isomerization product is at the equilibrium, which is not the case on the ns timescale. However, the low signal to noise ratio of the final EADS makes very difficult the clear assignment of these bands.

Compound 8

Compound 8 was also studied in both acetonitrile and dichloromethane. The Evolution Associated Difference Spectra obtained by performing a global analysis of the transient data are reported in figure 5.20.

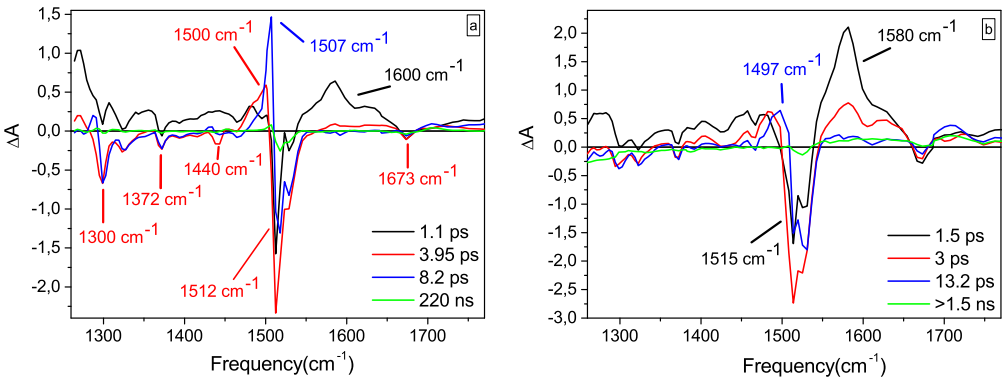

Figure 5.20: EADS obtained from global analysis of the time resolved IR data collected for compound 8 in acetonitrile (panel a) and dichloromethane (panel b).

The initial spectral component obtained from data analysis in acetonitrile (black trace, panel a) presents several broad positive absorption bands in both the 1250 to 1500 and 1530-1650 cm^{-1} spectral intervals, with peaks at 1250 and 1600 cm^{-1}. The negative bleaching signals are partially covered by these absorptions. An intense bleaching band is observed at 1512 cm^{-1}, and a smaller negative band at 1528 cm^{-1}. DFT computations identify two vibrational modes in this

frequency range: an intense band at 1517 cm^{-1}, assigned to the C=N stretching mode, with some NH bending contribution, and a less intense band at 1500 cm^{-1} due to a more delocalized mode, mostly involving the aromatic C=C stretching. The comparison between experimental and computed FTIR spectra of the Z form of compound 8 in acetonitrile is reported in panel a of figure 5.21. In the same figure panel b reports the computed spectra of the Z and E forms of the molecule.

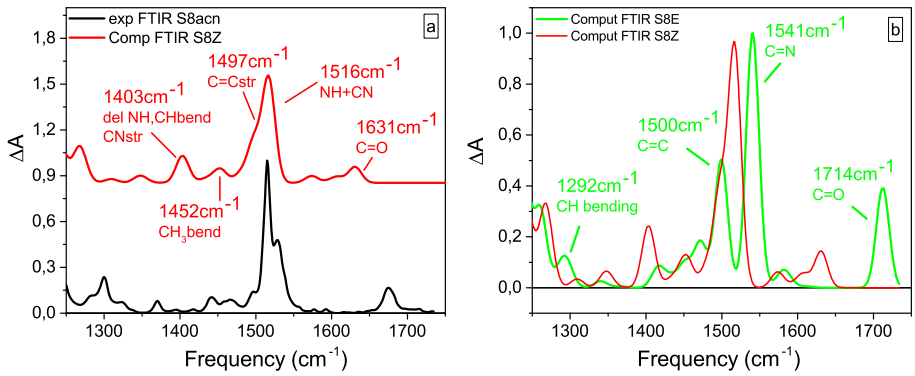

Figure 5.21: a) Comparison between the computed FTIR spectra of the Z form of compound 8 (red trace) and the experimental FTIR spectra recorded in acetonitrile (black trace). b) Computed FTIR spectra of the Z(red line) and E (green line) of compound 8

In the transient IR spectra, the intensity of most of the positive bands observed in the first spectral component decreases in 1.1 ps, revealing further bleaching bands, the most intense being at 1300 cm^{-1}, and some other small negative peaks at 1326 cm^{-1}, 1372 cm^{-1}, 1440 cm^{-1} and 1673 cm^{-1}. According to DFT computations, the bleaching band at 1372 cm^{-1} (calculated at 1403 cm^{-1}) is assignable to a delocalized mode involving C=N stretching, aromatic C=C stretching and NH bending, the weak band at 1440 (calculated at 1452 cm^{-1}) to methoxy bending modes and that at 1673 cm^{-1} to the C=O stretching mode.
Visible pump-probe data have been interpreted assuming that sample 8 reaches a state with CT character, and possibly twisted geometry, on a very short timescale (<150 fs). A positive band peaking at 1600 cm^{-1} is observed on this short timescale, possibly due to the upshifted C=N stretching whose intensity mostly decreases within 1 ps. The observation of this band could thus be indicative of a very fast structural distortion determined by the formation of the TICT state. After 1.1 ps, the almost complete decay of all the ESA bands signals the excited state decay (observed in about 1.8 ps from visible pump-probe). The molecule thus rapidly reverts to the ground state, with excess vibrational energy. A positive band observed at 1500 cm^{-1} in the second EADS (red trace) could signal a slight variation of electron density on one or both the phenyl moieties.
During the following evolution in about 4 ps, we observe the red-shift of the positive band at 1270 cm^{-1} to 1287 cm^{-1} and we observe a significant increase in intensity and red shift of the band at 1500 cm^{-1} (which now moves to 1507 cm^{-1}). The correspondent spectral component (blue trace) can be associated to a partially relaxed hot Z ground state, with some contribution coming from the E form as the result of a low yield photo-isomerization. In fact, the red-shift of

the positive band in the 1270 cm^{-1} region could be assigned to the red-shift of the C-H bending mode predicted by DFT calculations for the Z→E isomerization (see the comparison between the red and green traces in figure 5.21 panel b). In range of the 1500 cm^{-1} band, however, DFT computations predict that upon isomerization the C=N stretching should have been upshifted from 1517 cm^{-1} to 1540 cm^{-1} because of the H-bond breaking, which is not observed in the transient spectra. An explanation can be found considering that only a very small contribution of Z→E isomerization can be inferred from global analysis of both IR and visible pump-probe data.
As a conclusion of the transient analysis, we can say that most of the population of sample 8 in acetonitrile reverts to the ground state through internal conversion and reaches a hot ground state that completely relaxes only after 8 ps (blue to green trace). As already pointed out from visible measurements, isomerization is not very favored for this compound in all solvents. The very small intensity of the difference IR spectrum on the long timescale (see the green trace in Figure 5.20) precludes a final assignment of the vibrational bands pertaining to the E isomer in acetonitrile.

The behavior of the sample in dichloromethane is very similar to that observed in acetonitrile, see panel b of figure 5.20. Both the spectral assignments and the kinetic evolution can be interpreted as already discussed for acetonitrile. The excited state decay seems slightly slower in this solvent and it is complete in about 3 ps, as demonstrated by the recovery of the positive excited state absorption bands. The E ground state reached on this fast timescale then relaxes within 13 ps (evolution from blue to green EADS). As also reported in the visible results, the solvent polarity seems to affect the deactivation pathway at minimal extent. The weak intensity of the two final EADS suggests a very low quantum yield for the isomerization process also in this case.
However, in dichloromethane, the slightly higher intensity of the final spectral component allows comparing the final EADS with the FTIR E-Z spectra. The static E-Z difference spectrum has been obtained by recording the FTIR spectrum of the Z form freshly prepared, and after few hours of irradiation (thus photoaccumulating the E form). The comparison between the FTIR E-Z spectrum and the final EADS is reported in Figure 5.22.

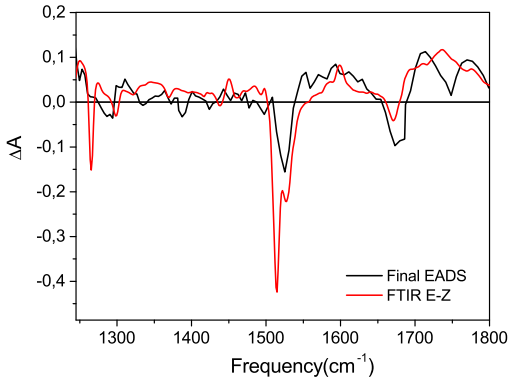

Figure 5.22: Comparison between the E-Z FTIR spectra (red line) and the final EADS obtained from global analysis of the time resolved IR data collected for compound 8 in dichloromethane.

The agreement between the two spectra confirms the presence of a small amount of the E isomer in the long living transient spectra. Most of the population however reverts to the Z ground state within 3 ps.

Compound 10

Compound 10 has both an electron withdrawing and an electron donating substituent on the rotor and stator moieties, thus behaving as a push-pull system. It is also characterized by an absorption wavelength red-shifted with respect to the others two samples (450 nm), appearing as the most interesting for the several applications. Transient data in the Uv-visible range have demonstrated a high influence of solvent polarity on the deactivation pathways of the molecule upon excitation. This sample presents both a high isomerization and fluorescence QY (in its Z form) in toluene, while in acetonitrile and dichloromethane the deactivation through a CT state appears to reduce both the isomerization and fluorescence yield, and to speed up the recovery of the ground state through internal conversion.

Transient infrared measurements have been performed in both cyclohexane and dichloromethane, trying to detect the different structural changes influenced by the polarity of the solvent. We also tried to perform measurements in acetonitrile, but the low solubility of the sample did not allow to record data with sufficient S/N ratio. The EADS obtained from global analysis of the transient data are reported in figure 5.23.

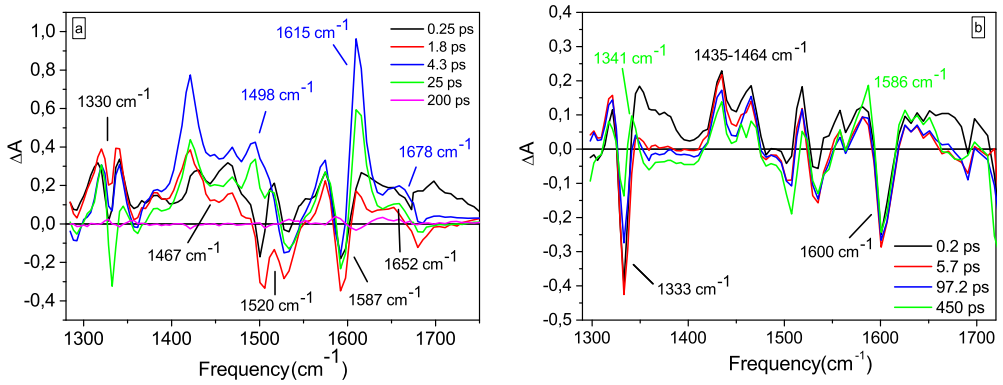

Figure 5.23: EADS obtained from global analysis of the time resolved IR data collected for compound 10 in dichloromethane (panel a) and cyclohexane (panel b).

The spectral changes observed over time in dichloromethane are very notable. In this solvent, the first two spectral traces (black and red line panel a) appears very similar, however the use of the first spectral trace at the limit of the temporal resolution must be considered in the analysis to improve the fitting. These traces both show two bleaching signals at 1520 cm^{-1} and 1587 cm^{-1}, the former associated with a delocalized mode involving the C=N, N-N, N-H stretchings, and the latter associated with the aromatic C=C stretching. Two intense broad ESA bands are visible, peaked at 1330 and 1426 cm^{-1}, besides three more positive bands at 1574 cm^{-1}, 1615 cm^{-1} and 1700 cm^{-1}. Panel a of figure 5.24 shows the comparison between the first EADS and the computed FTIR spectra of sample 10-Z and it allows identifying the correspondence of the bleachings with the ground state modes observed in the static spectrum.

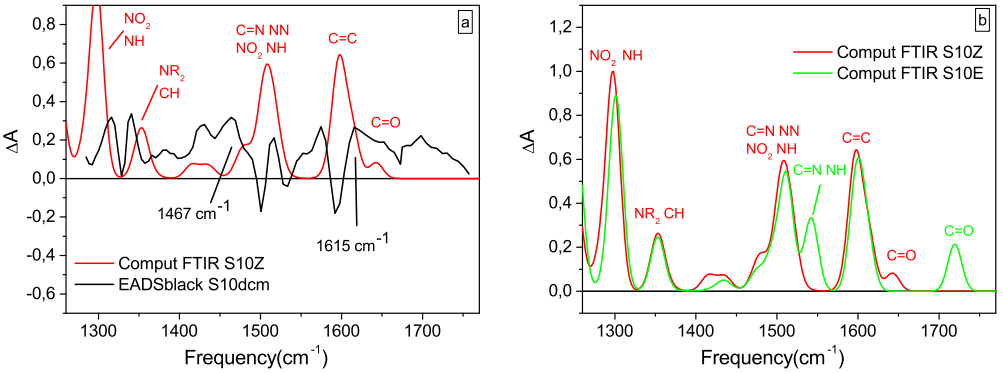

Figure 5.24: Panel b shows the comparison between the computed FTIR spectra of the Z form of compound 10 (red trace) and the first EADS extrapolated from the transient data of compound 10 in dichloromethane (black trace). Panel b shows the computed FTIR spectra of the Z form of compound 10 (red trace) compared to that of the E form (green trace).

Considering the results obtained in Uv-vis TAS, the red EADS extrapolated from data analysis after 250 fs should be assigned to the transient absorption

of both a localized excited state and a charge transfer state. After 1.8 ps, the rise of intensity around 1500 cm^{-1} and 1615 cm^{-1} indicates the occurrence of a structural modification of the excited state. This transition can be probably connected to the population of the TICT state, that in the visible pump-probe experiments was recorded with a quite faster kinetic (667 fs). In fact, the band at 1615 cm^{-1} according to computations can be assigned to an upshift of the phenyl C=C stretching and the band at 1652 cm^{-1} could signal the C=O stretching of the excited state redshifted (more localized) with respect to the ground state (panel b of figure 5.24).
Within 2 ps, the intensity of the excited state absorption bands decreases suggesting a vibrational relaxation of the excited state. The excited state absorption bands mostly decay in 19.3 ps, signaling ground state recovery. Considering the very low intensity of the final spectral component (green line in Figure 5.23), we conclude that most of the population reverts to the initial Z ground state. The intensity of the final EADS is too low to be compared to the difference between the FTIR spectrum of the E and Z forms. Isomerization yield is expected quite low.

The kinetic traces of compound 10 recorded in cyclohexane are quite noisy because of the low solubility in this solvent. The EADS are reported in panel b of Figure 5.23. The data were recorded from -5 ps to 300 ps time delay. We notice that spectral evolution in this time interval is quite limited. After light absorption, the excited state undergoes a fast, possibly electronic, relaxation, occurring in about 200 fs, signaled by the decay of several excited state absorption bands, in particular in the 1350-1400 cm^{-1} region. The excited state absorption bands can be somehow compared to those observed in dichloromethane, although in this case spectral evolution is much less evident. In particular a double peaked ESA band is observed at 1435-1464 cm^{-1}, possibly due to the downshift of the modes delocalized over the central part of the molecule in the excited state. Two more positive peaks are noticed at 1520 and 1582 cm^{-1}. All the ESA bands slightly decrease in intensity in the investigated time interval, except for the band at 1341 cm^{-1} and that at 1582 cm^{-1}. Both bands slightly increase in intensity by about 97 ps (evolution from blue to green-EADS), and that at 1582 cm^{-1} redshifts to 1586 cm^{-1} on this same timescale.
In the Uv-visible range, the isomerization process was assigned to a spectral evolution proceeding in about 5 ps, signaled by the decrease of the stimulated emission band (panel d figure 5.17). In the infrared it is difficult to identify the exact isomerization time scale, because of the limited spectral evolution. Furthermore, since the sample has a good fluorescence quantum yield in non polar solvents, part of the population remains in the excited state on the 300 ps timescale, making it difficult to evidence specific changes associated to isomerization.
The computed Z and E FTIR spectra highlight the expected spectral shifts associated with the isomerization. In particular, it is expected to observe a slight upshift of the band calculated at 1300 cm^{-1} and assigned to NO_2 stretching, a significant upshift of the C=N stretching mode from 1502/1510 cm^{-1} (delocalized modes) to 1542 cm^{-1} (highly localized), a slight upshift of the C=C aromatic stretching in the 1600 cm^{-1} region, and lastly an upshift of the C=O mode calculated at 1642 cm^{-1} for the Z form and 1719 cm^{-1} for the E form. Comparing the difference spectrum of the computed E and Z FTIR spectra with the final EADS (figure 5.25), several positive bands are in reasonable agreement with the up mentioned

changes expected from computations. In particular, the positive band at 1341 $^{-1}$ could be assigned to the upshifted NO_2 symmetric stretching, with the corresponding ground state absorption at 1334 cm^{-1} (observed as a bleaching band). The upshifted C=N mode could be assigned as the positive band at 1586 cm^{-1}, with corresponding bleaching at 1535 cm^{-1}. Finally, the upshift from 1689 cm^{-1} to 1700 cm^{-1} can be related to the changes in the C=O stretching.

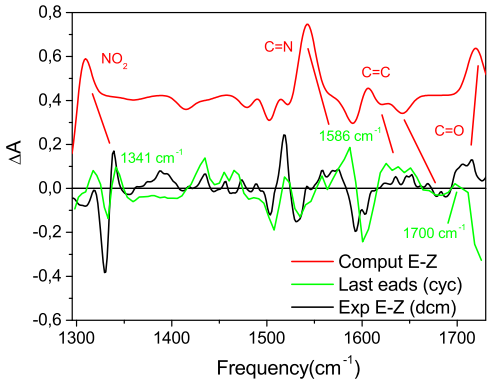

Figure 5.25: Comparison between the E-Z computed FTIR spectra (red line) of compound 10, its E-Z experimental FTIR spectra (black line) in dichloromethane and the final EADS obtained from global analysis of the time resolved IR data collected for compound 10 in cyclohexane.

Contrary to what observed in dichloromethane the signal in cyclohexane does not recover on the measured timescale, which allows a comparison of the long living EADS (green line in figure 5.25) with the experimental E-Z FTIR difference spectrum (black line, it is recorded in dichloromethane for solubility reasons). The agreement between the two traces confirms that isomerization of compound 10 is not a minor decay channel in non polar solvents, in line with the 50% isomerization yield estimated in toluene.

Finally, as already observed from visible pump-probe data, we confirm that solvent polarity has a notable effect on the excited state relaxation pathways and dynamics. In fact, while in dichloromethane the transient signal goes almost to zero in less than 100 ps, in cyclohexane there is still substantial differential signal on a longer timescale, as noticed by comparing selected kinetic traces measured in the two solvents (figure 5.26).

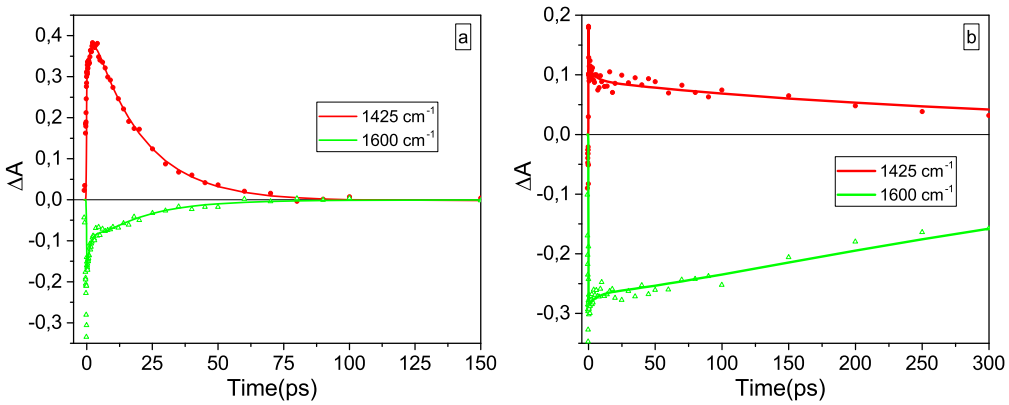

Figure 5.26: Selected kinetic traces registered in dichloromethane (panel a) and cyclohexane (panel b).

Table 5.3 collects the time constants obtained from the analysis of the IR transient absorption spectra.

Compound	Solvent	τ_1	τ_2	τ_3	τ_4
7	ACN	0.75 ps	7.5 ps	21.5 ps	$>$ 1.5 ns
	DCM	0.93 ps	3.2 ps	55 ps	$>$ 1.5 ns
8	ACN	1.1 ps	3.95 ps	8.2 ps	220 ns
	DCM	1.5 ps	3 ps	13.2 ps	$>$ 1.5 ns
10	CHEX	0.2 ps	5.7 ps	97.2 ps	450 ps
	DCM	1.8 ps	2 ps	19.3 ps	256 ps

Table 5.3: Decay times observed in the IR transient spectra for all the three compounds 7, 8 and 10 in the different solvents.

5.2.4 Conclusions

Three bistable photochromic hydrazones have been characterized in solvents of different polarity with static and transient spectroscopy. Upon the excitation in the visible range, visible and infrared spectra of the transient excited species, populated during the deactivation pathway, have been recorded. The aim of this deep spectroscopic characterization was that of depicting the energetic and structural changes of the molecules and identify the excited state relaxation pathway and the photoswitching mechanism. The three hydrazones were previously studied in toluene. Good photoswitching performances were reported for compound 7, an hydrazone with an electron withdrawing nitro group attached to the stator phenyl ring (QY=35%; PSS=98%; $\tau_{1/2}$=1286 years), and compound 10, with a donating dimethyl amine linked to the rotor ring and a NO_2 group linked to the stator phenyl (QY=46%; PSS>99%; $\tau_{1/2}$=126 years). A very low photoswitching efficiency was instead detected for compound 8 (QY=5%; PSS=93%; $\tau_{1/2}$=0.039 years), where the NO_2 group on the stator is replaced by a donating methoxy substituent and no adding groups are attached on the rotor ring.

The spectroscopic analysis we performed in toluene, dichloromethane and acetonitrile has shown a strong decrease of the isomerization efficiency due to solvent polarity. In polar solvents, transient visible and infrared spectroscopy reveal the presence of an excited state characterized by a charge transfer character. This state seems to highly penalize the deactivation channel proceeding through $Z \rightarrow E$ conversion. The very low isomerization QY of compound 8 in toluene can be ascribed to this same CT state that has been detected also in the non polar solvent. For this compound, the charge transfer process favored by the electron donating group on the stator ring appears not influenced by the solvent polarity and it drastically reduces the hydrazone ability of photoswitching in all solvents. Compound 7 and the push-pull compound 10 show a very similar behavior when analyzed in polar solvents, as also expected by the similar photoswitching performances. In toluene, where no evidences of the charge transfer state have been detected, isomerization occurs in less than 10 ps for both compounds (11 ps for compound 7 and about 5 ps for compound 10). The transient signal of compound 10 in non polar solvents does not decay completely on the analyzed timescale, allowing to discuss and assign spectral features pertaining to the E isomer (compound 7 has been studied in toluene only with visible pump-probe.) In acetonitrile and dichloromethane, compound 7 and 10 show transient ESA bands which have been interpreted as arising from an excited state with charge transfer character. The transient spectra almost completely recover within tens of picoseconds, indicating a low isomerization QY.
In summary, our measurements indicate that the presence of an electron withdrawing substituent on the stator phenyl ring increases the charge transfer character of the excited state and determines a stronger dependence of the excited state relaxation on the solvent polarity.

Chapter 6

General conclusions

This thesis collects the theoretical and experimental analyses of three different molecular systems. These molecules are all characterized by the capability of absorbing visible light and undergoing photochemical processes, in some cases structural transitions, which can be exploited for medical, opto-electronic or renewable resources applications.

Chapter one and chapter two describe the characterization of different *Donor-Acceptor* chromophores, designed to enhance their Triplet State quantum yield increasing the rate of Inter System Crossing. The triplet state of a molecule is an extraordinary functional species, whose population can be triggered by absorption of light. Triplet states can be used for inducing very important processes like the disruption *in vivo* of cancer cells (photodynamic therapy) or the up-conversion of energy in solar cells (covering that part of the solar spectrum not absorbed by silicon).
This first section reports two different and innovative methods to obtain high triplet QYs. The first method uses a radical species linked to a chromophore to induce a spin-spin exchange interaction between the moieties, that makes ISC a spin allowed process. This method is called Radical Enhanced ISC and has been presented reporting the transient analysis of a family of Perylene-Oxoverdazyl dyes, where ISC takes place very fast (0.5 ps) and the triplet states obtained are very stable (9.5 μs of lifetime).
The second method is the Spin Orbit Charge Transfer ISC mechanism, that can be obtained in Donor-Acceptor compact dyads with an orthogonal geometry. A photoinduced electron transfer between orbitals located on two moieties arranged perpendicularly to each other determines a large orbital angular momentum change that is compensated by the electron spin flip, determining the population of the triplet state. We report the spectroscopic analysis of two molecular systems undergoing efficient SOCT-ISC mechanism. The design of simple and compact Rhodamine Naphtalimide dyes results in outstanding long lived triplet states with charge transfer character (0.94 μs), never observed before without using heavy atoms or intrinsic ISC abilities. The transient characterization of Carbazole-Anthracene-Bodipy triads demonstrates the favourable outcome of SOCT-ISC mechanism also in distant Donor-Acceptor systems with particular properties. The multistep electron transfer observed in these triads determines very high triplet quantum yields even in non polar solvents ($\Phi_T = 1.00$).
Thanks to the collaboration with the photochemistry group of professor Zhao

in Dalian, the characterization of many other different *Donor-Acceptor* chromophores is still in progress in our laboratories. All these systems represent a fundamental tile in the forthcoming perspective of a direct application of D-A molecules not only in photodynamic therapy, but also in artificial photosynthesis, optoelectronic devices and organic photocatalysis.

Two other molecular systems of great interest have a central role in this thesis and have been the object of a deep characterization with non-linear spectroscopy.

In collaboration with the group of prof. Reginato at CNR in Florence, we performed the transient absorption characterization of different families of organic dyes designed as collectors for Luminescent Solar Concentrators. D-A-D structures with a quinoxaline central core dispersed in PMMA and PCMA film have shown good optical efficiencies. The spectroscopic results reported in chapter four demonstrate the importance of these innovative structures and promote further investigations and improvements for their use as promising LSCs fluorophores.
Not less important results have been obtained in the analysis of a family of bistable photoswitches. Three particular hydrazones differently substituted with electron-withdrawing or -donating groups have been characterized using Visible pump-probe and Visible-Infrared pump-probe spectroscopies. As reported in chapter five, the detection of a charge transfer state uncovers the strong dependence of the photoswitching mechanism of these molecules on the solvent polarity. Moreover, transient analysis also unveil a relationship between a strong reduction of photoswitching performances and the addition of a specific group on the hydrazone structure. One of the molecule we considered shows outstanding performances and also an extremely slow thermal half-lives among all the reported configurational photoswitches (2700 years).

All the presented molecules are important examples of systems having a promising role in different fields. We use pump-probe spectroscopy to uncover the ultrafast structural and energy changes that, induced by light absorption, precede and influence following chemical transformations. Transient excited states, electron and charge transfer processes, conformational changes, all these ultrafast species and changes has been detected and described. Further analysis must be implemented for the concrete application of these molecules in medicine, in energetic and electronic engineering and in molecular photonics, to obtain an effective step forward a better living thanks to science for the everyday life.

Appendices

Appendix A

Photoinduced electron transfer principles

One-electron oxidation and reduction processes are central reactions in organic, biological and inorganic chemistry. The special case of photoinduced Electron Transfer has a central role for reproducing the efficiency of natural light-harvesting systems. The photoexcited state of a molecule is certainly a stronger oxidizing or reducing specie than its own ground state. In this sense this state is able to induce or "sensitize" permanent chemical changes [1] in a neighboring ground-state molecule by what is so called a *photoinduced electron transfer* (PET).
PET is based on the migration of an electron between a photoexcited species and a ground-state species. It can be induced by an intermolecular encounter, or by the interaction between different units of the same system. In both cases, PET can be classified as a quenching pathway, because it competes with any other intra- and inter-molecular deactivation pathway that quenches the luminescence of an excited state.
It is important not to mistake PET process for another important quenching mechanism called *energy transfer* (ET,(A.1)):

$$D^* + A \quad \xrightarrow{k_{ET}} \quad D + A^* \qquad \text{Energy Transfer} \tag{A.1}$$

In both these *transfer* processes, the two interacting species are designated as electron (or energy) Donor (D) and Acceptor (A), and the species in the excited state is identified by a superscripted star. In the *energy transfer process*, the excited state is exclusively an energy donor, while in *electron transfer* it can be both an electron donor or an electron acceptor. For this reason in case of PET we can have two possible reactions:

$$D^m + A^n \quad \xrightarrow{h\nu} \quad [D^n]^* + A^m \quad \xrightarrow{k_{PET}} \quad D^{m+1} + A^{n-1} \tag{A.2}$$

or

$$D^m + A^n \quad \xrightarrow{h\nu} \quad D^m + [A^n]^* \quad \xrightarrow{k_{PET}} \quad D^{m+1} + A^{n-1} \tag{A.3}$$

k_{PET} is the rate constant of the electron transfer process, while m and n represent the original charges of the donor (D) and the acceptor (A).
Energy transfer can proceed throught two different mechanisms: *dipole-dipole mechanism* or *electron exchange mechanism*. If we consider the *electron exchange mechanism* (figure A.1), in some ways Electron transfer and Energy transfer mechanisms are similar. In fact, both are determined by the migration of electrons needing a very closed approach of the interacting systems [91].

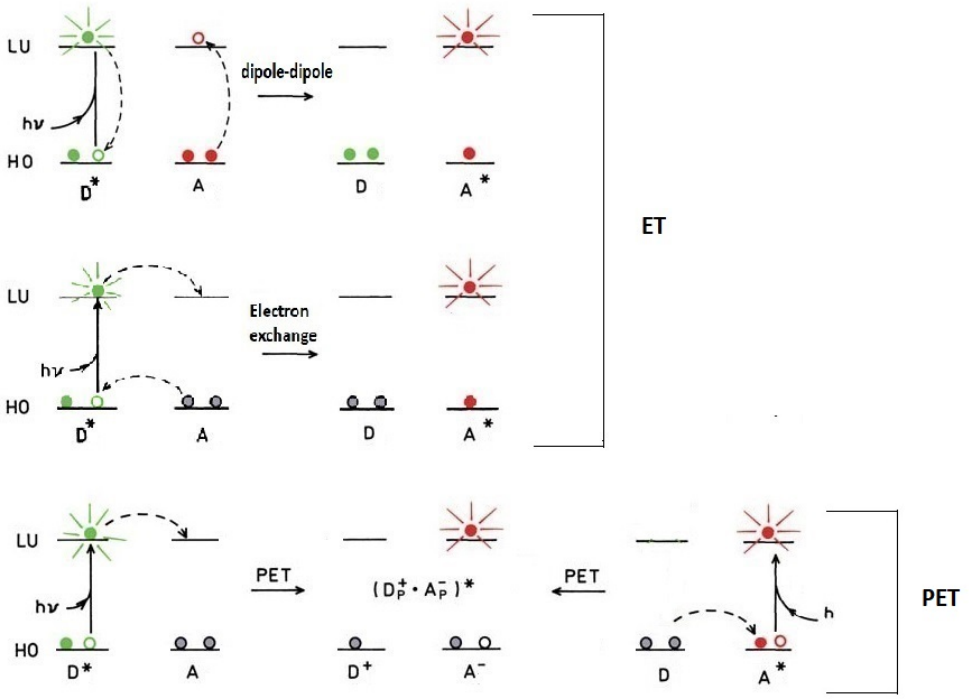

Figure A.1: Comparison between Energy and Electron transfer mechanisms [92].

In the following sections, the theory and the feasibility conditions of photoinduced electron transfer are presented. The theoretical description is reported using the general example of two interacting species that are separated and not linked together. However, it is possible to note that in this thesis, the discussion and application of PET theory is centered on bimolecular systems in which donor and acceptor are connected by a molecular linking group. In these rigid or flexible systems, the absorption of light determines the formation of an excited state not delocalized on the entire molecule, but localized on one of its component units. As a matter of fact, the electronic interaction among the two attached units of a same molecule induces the deactivation process [17].

A.1 Energetics of photoinduced electron transfer

Before the actual event of electron migration from one unit to another, the absorption of light must induce the formation of an equilibrated excited state of the Donor or Acceptor. The energy contained in this state enhances the ability of donating and accepting electrons with respect to the same unit in its own ground state.
The excited state can be designed as a new chemical species with respect to the ground state because of its different energy content and its redistribution of electrons in the molecular orbitals. These two factors influence many properties of the excited state like structure, charge distribution, electron affinity, ionization potential, etc. The excited state energy is generally assigned to the energy difference between the lowest vibrational level of the ground state and the lowest vibrational level of the excited state. This energy is designated with the term E_{00}, because it corresponds to the energy of the electronic transition between the

0-vibrational level of the ground state and the 0-vibrational level of the excited state.
The 0-0 transition energy can be related to the force required to remove from (*ionization potential, IP*) or combine with (*electron affinity, EA*) a new electron to an atom or molecule in the gas phase. In fact, an electron transfer is usually permitted when the electron affinity of one of the two component exceeds the ionization potential of the other (EA>IP). This condition is generally achieved through the absorption of a photon, because the photoinduced excitation of an electron to an orbital with higher energy decreases the IP value (A.4), while increases the EA of the leaving hall (A.5):

$$IP^* = IP - E_{00} \tag{A.4}$$

$$EA^* = EA + E_{00} \tag{A.5}$$

The magnitude of IP and EA is so related to E_{00}, depending on the energies of the highest occupied molecular orbitals (HOMO) from which the electron is abstracted, and the lowest occupied molecular orbitals (LUMO) accepting the new electron. The relative ordering of these molecular orbitals is so essential for the feasibility of the electron transfer process (figure A.2).

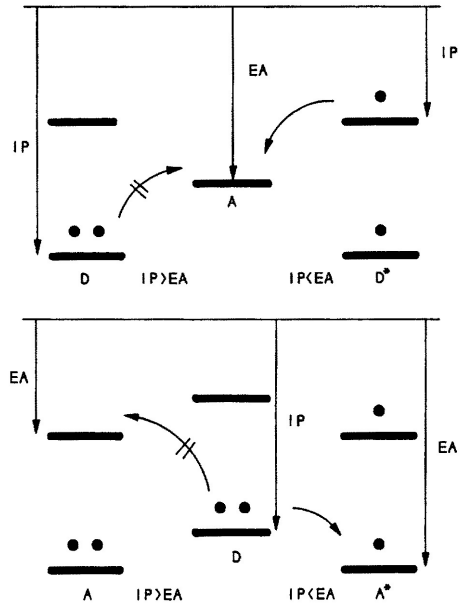

Figure A.2: Simplified orbital picture to explain the relative energies of donor and acceptor electrons and the influence of the photoexcitation on orbitals energy differences for the PET process in gas phase [91].

The electron redistribution in molecular orbitals induces the charge-transfer character of the excited state, that can vary from 0 to 1. The maximum value (1) corresponds to the transfer of one electron from the Donor to the Acceptor. The generated excited state is so called Charge Separated state (CS).
Even if the consideration of IP and EA value is useful to understand why an excited state is a better donor or acceptor of electrons, the equations presented above are valid only for molecules in the gas phase. PET processes in solution or solid environments are greatly influenced by electrostatic effects or solvation energies that must be considered in a precise thermodynamic description of reaction.

A.1.1 PET in solutions or solid environments

Since its evolution from reagent to product species, electron transfer can be considered as a *chemical* process. For this reason the driving force that quantify the spontaneity of the reaction is expressed trough the free energy difference of the reaction (ΔG_{el}).
Free energy of electron transfer depends on the redox potentials associated to the oxidation and reduction of the two interacting species. For this reason, PET is one of the quenching processes whose efficiency is much more predictable with respect to others, knowing the electrochemistry of the species involved.
Considering the electron donor as the excited specie pf the process (A.2), the free energy change (or driving force) for the photoinduced electron transfer is given by the sum between the free energy difference of the excited donor oxidation ($\Delta G_{D^* \to D^+}$) and the free energy difference associated to the acceptor reduction ($\Delta G_{A \to A^-}$). If the resulting free energy is expressed in electron volts and it is associated to a *one-electron* transfer process between two species, the final expression can be directly written using the redox potentials instead of ΔG parameters:

$$\Delta G_{el} = E^0(D^+/D^*) - E^0(A/A^-) \tag{A.6}$$

The redox potential for oxidation of the excited electron donor can be calculated as:

$$E^0(D^+/D^*) = E^0(D^+/D) - E_{00} \tag{A.7}$$

Substitution of equation (A.7) into (A.6) leads to

$$\Delta G_{el} = E^0(D^+/D) - E^0(A/A^-) - \Delta G_{00} \tag{A.8}$$

where ΔG_{00} is the free energy, in electron volts, corresponding to the equilibrium energy E_{00}.

After the electron migration, the two ions formed $[D^+ \cdots A^-]$ are subjected to an electrostatic interaction, that is influenced by the surrounding solvent and that leads to an effectively release of energy. For this reason, the free energy change, that accompany the photoinduced electron transfer between two species in a specific solvent, can be rewritten from equation (A.8) to the Rehm-Weller equation:

$$\Delta G_{el} = E^0(D^+/D) - E^0(A/A^-) - \Delta G_{00} - \frac{e^2}{\epsilon d} \tag{A.9}$$

The energy released with the electron transfer ($\frac{e^2}{\epsilon d}$) is influenced by the solvation of the ion couple and it depends on the dielectric constant of the solvent (ϵ) and on the distance between the charges (d). The two terms ΔG_{00} and $\frac{e^2}{\epsilon d}$ appear with negative sign because both light excitation and Coulomb attraction implicate an energy stabilization of the system.
Thanks to the estimation of the free energy changes associated with photoinduced electron transfer, it is possible to characterize the spontaneity of the process. However, the exothermicity of the reaction is not always enough to guarantee its proceeding, because some other factors control its rate. Kinetic barriers along the potential energy pathway from reagents to ionic couple, can prevent PET reaction from occurring (figure A.3).

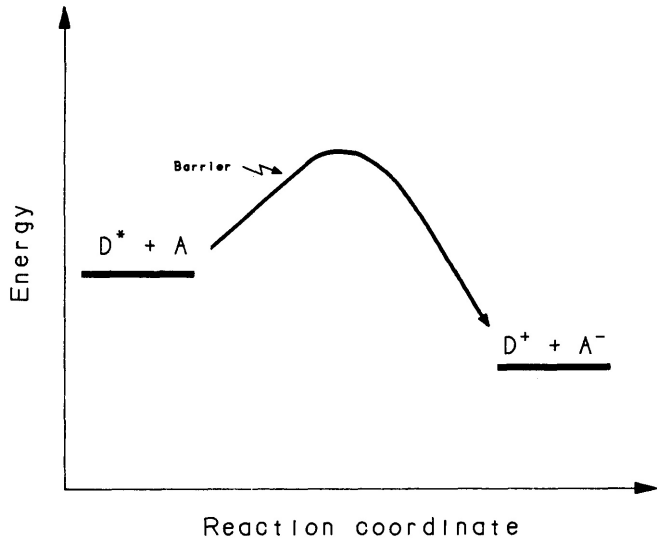

Figure A.3: Kinetic barrier that can prevent the development of the photoinduced electron transfer [1].

The extrapolation of those factors controlling the rate of reaction is a fundamental task. In this sense, many theoretical contributions must be summed up to explain the reactivity of PET, all related to the definition of the activation rate constant of the process (k_a).

A.2 Electron transfer rate constants

The rate constant of PET can be extrapolated using a steady-state treatment of the process based on the general view of encountering species. In this case, the system is considered as an ensemble of sensitizers and quenchers surrounded by several shells of solvent molecules.
For this type of system, the scheme that describe PET process is shown in equation (A.10), evidencing all the kinetic constants related. The scheme describes the specific case of PET in which the electron donor is the excited specie.

$$\mathrm{D}^* + \mathrm{A} \underset{\mathrm{k_{-dif}}}{\overset{\mathrm{k_{dif}}}{\rightleftharpoons}} \mathrm{D}^* \cdots \mathrm{A} \underset{k_{-el}}{\overset{\mathrm{k_{el}}}{\rightleftharpoons}} [\mathrm{D}^+ \cdots \mathrm{A}^-] \xrightarrow{\mathrm{k_{ret}}} [\mathrm{D}^+\mathrm{A}] \tag{A.10}$$

As depicted in the scheme, considering the system as an ensemble of diffusive and interacting donors and acceptors, introduces the strong dependence of the quenching dynamic of reactants on their diffusive encounters dynamic. The constant k_{dif} expresses the diffusion rate of the molecules dispersed in the solvent, while k_{-dif} defines the opposite rate of separation of the *encountered complex* $(D^* \cdots A)$.
Among the other parameters, the first-order rate constant of electron transfer is k_{el} and the constant assigned to the reverse step is k_{-el}.
Thanks to the analysis of the sequential scheme in eq. (A.10), it is possible to extrapolate the kinetic expression defining the quenching rate associated to the process (eq. (A.11)).

$$k_q = \frac{k_{dif}}{1 + (k_{-dif}/k_{el})} \tag{A.11}$$

In this expression, the process of charge recombination (k_{-el}) and that of electron return (k_{ret}) have not been considered. In fact, the former is generally thermodynamically uphill and for this reason unfavorable, while the latter is usually downhill and so it does not much influence the bimolecular rate of quenching by electron transfer (k_q).
The bimolecular rate constant for electron transfer (k_a) depends on the equilibrium rate constant for formation of the encounter complex ($K_{eq} = k_{dif}/k_{-dif}$) and on the already mentioned k_{el}. It is defined as follow:

$$k_a = \frac{k_{dif}}{k_{-dif}} k_{el} = K_{eq} k_{el} \tag{A.12}$$

Combining equation (A.12) with equation(A.11), the quenching constant can be expressed as:

$$\frac{1}{k_q} = \frac{1}{k_{dif}} + \frac{1}{k_a} = \frac{1}{k_{dif}} + \frac{1}{K_{eq} k_{el}} \tag{A.13}$$

The expression (A.13) evidences that the activation rate k_a can be easily determined thanks to the calculation of the diffusion constant k_{dif} and the calculation of the quenching rate k_q. The former can be obtained with the viscosity values of the solvent at a given temperature, while the latter is calculated with the Stern-Volmer experimental techniques.
In all those systems in which the diffusion dynamic does not influence the encounter of the two interacting species (for example in solid state and in rigid macromolecules where the donor and acceptor are linked together), the electron transfer is a *diffusionless* process and the kinetic stage that determines the formation of the encounter complex (k_{dif}) does not contribute to the activation rate of PET: $k_q \simeq k_a \simeq k_{el}$.
Even if the electron transfer rate constant can be calculated, its resulting value does not differentiate the rate-determining factors that contribute to it. The classification of these factors is fundamental for the complete understanding of reactivity in electron transfer. These factors are the ensemble of *electronic interactions* and *nuclear motions*. They determine the presence of energetic barriers along the reaction pathway that must be overcome for the continuation of the electron transfer reaction.
The dependence to the electronic and nuclear parameter can be introduced in the following theoretical expression:

$$k_{el} = \nu_n \kappa_n \kappa_{el} \tag{A.14}$$

where the ν_n term is the *nuclear frequency*, κ_n is the *nuclear factor* and κ_{el} is the *electronic factor*. A description of the electronic and nuclear factors is reported below.

Electronic factor

The *electronic factor* κ_{el} depends on the interaction between the electronic configuration of the reactant and the product state. In the reactant state, the reagents are separated and described as $[D^* + A]_{ST}$, while in the configuration of the product state, donor and acceptor are a ionic couple ($[D^+ \cdots A^-]_{ST}$). The magnitude of electronic interaction between the reactant and product state is expressed

trough the *matrix element for electronic interaction* H_{el}:

$$H_{el} = \langle \Psi_{D^*A} | \hat{H}_{el} | \Psi_{D^+A^-} \rangle \tag{A.15}$$

The interaction between the two potential energy surfaces of the reactant state and product state reflects the interaction between the donor and acceptor orbitals, whose eigenfunctions and eigenvalues, after the beginning of interaction, start to experience changes. In fact, H_{el} is influenced by many factors related to the Donor-Acceptor link, like their separation distance, spin changes, symmetry factors and their orientation.
Parabolic curves referring to the states just before and just following the electron migration can be used to represent the electron transfer pathway [1]. In this approximation, PET is analyzed in terms of intersecting harmonic potential surfaces as figure A.4 reports.

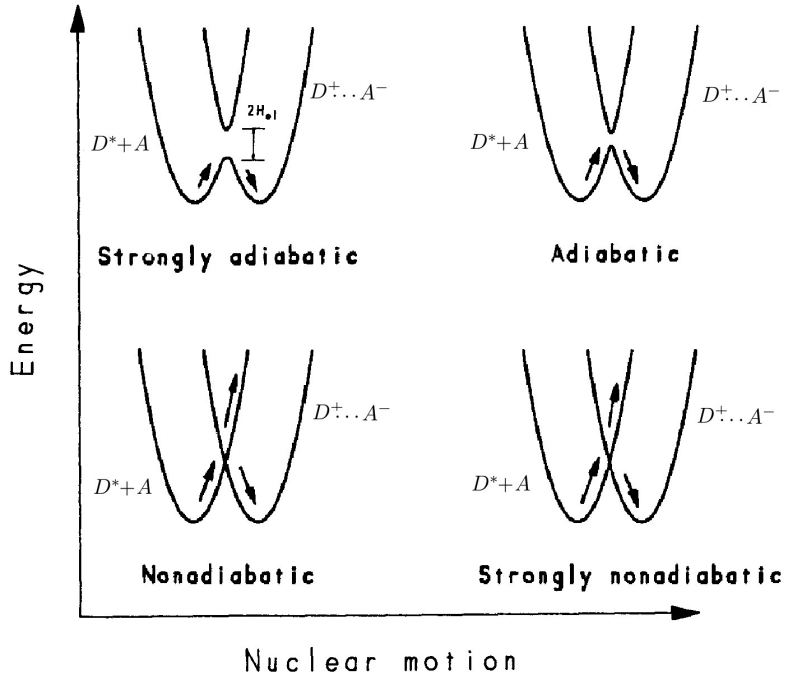

Figure A.4: Nuclear motion-energy representation of the four different cases in which the electron transfer can proceed from the reactant to the product state [1].

Looking at figure A.4, when the reactant molecules interact at distances within molecular dimensions, the interaction between the curves is strong and a perturbation of the system must be considered. If the perturbation is strong, it determines the presence of a new factor in the secular determinant of the system equation, whose resolution gives new potential energy curves for the initial and final states. These new resulting curves do not intersect, avoiding one another. The curves are defined as *adiabatic* and they do not cross because of the strong perturbation between the zero-order reactant state and the product state (figure A.4).
If the perturbation is neglecting, the resolution of the eigenfunction equation that describes the system gives as solution the potential energy of the zero-order states of reactant and product. In this case the two potential energy curves weakly interact and they intersect in the nuclear motion vs energy representation of electron

transfer evolution; these curves are so called *diabatic* or *nonadiabatic* intersecting curves (figure A.4).
As presented in figure A.4, electron transfer reaction can take place in both the extreme conditions in which the interaction between the reactants is strongly adiabatic ($\kappa_{el} = 1$) or strongly nonadiabatic ($\kappa_{el} = 0$). In the first case, H_{el} is so large that the reaction proceeds on one potential energy surface with the energy barrier, from one minimum to the other, that is proportional to the interaction energy ($2H_{el}$). In the second case, after numerous oscillations in the reactant curve, the electron has to jump the energy barrier that separates the donor and the acceptor.

Nuclear factor

The *nuclear factor* represents the reorganization of nuclear geometry needed to the actual formation of a transition state before the occurring of electron transfer. As a matter of fact, this factor is related to the free activation energy for electron transfer ($\Delta G_{el}^{\neq}$), that corresponds to the energy of the transition state itself.

$$\kappa_n = e^{\frac{\Delta G_{el}^{\neq}}{RT}} \tag{A.16}$$

Nuclear reorganization for the formation of the transition state includes not only the changes in the internal and vibrational modes of reactants but also all the changes in the nuclear polarization of the surrounding solvent molecules (Marcus theory, see paragraph A.3.1).

A.3 Theories of photoinduced electron transfer

Nuclear and electronic contributions are classified and presented by two main PET theories based on different approaches.

- The first one is the *classical Marcus theory*. This theory emphasizes the contribution of Coulumbic and nuclear factors to the energetic barriers along the electron transfer kinetic pathway, while neglecting the electronic ones ($\kappa_{el} \sim 1$). This theory extrapolates those factors determining the rate of the proces and permits predictions on the electron transfer reactivity for the excited state of an examining sample.

- The second theory is defined as *quantum mechanical* or *nonclassical theory*. It considers the overlap between the reactant and product wavefunctions of both nuclear and electronic configurations. In this case electronic barriers are strongly evaluated. Thanks to this theory it is possible to include in the treatment of PET processes the tunneling effect, that makes possible to overcome nuclear and electronic barrier limiting the rate process. Tunneling is a process through which the reaction coordinate crosses the transition state barrier even without the possession of activation energy ($\Delta G_{el}^{\neq}$) that, instead, is the necessary limiting factor of Marcus theory treatment.

A.3.1 Marcus theory

Nuclear and electronic motions taking part in photoinduced processes are generally treated separately as stated by the Born-Oppenheimer approximation. Electrons mass is smaller than the typical nucleus mass so that the electron motion is much faster and it can be separated from the response of the nuclei to the change of electron configuration.
Due to Born-Oppenheimer approximation, the electron excitation is considered as a vertical transition from a lower state of a molecule to a higher state called Frank-Condon state (excitation in figure A.5).

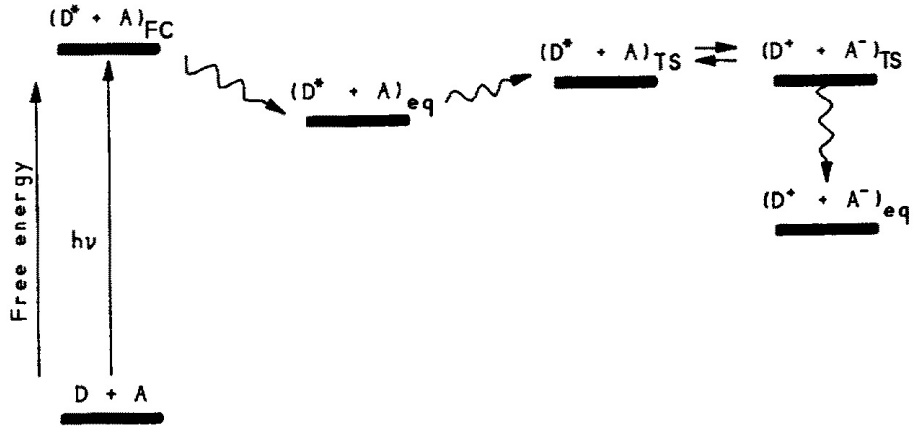

Figure A.5: Subsequent passages of PET process, from the photoexcitation of the donor specie to the formation of the nuclear relaxed product state, passing through the Frank-Condon-like transition state [91].

FC state is characterized by a different electronic configuration than the previous ground state, but by the same nuclear geometry. Nucleus motion arrives in a second moment with a rapid reorganization and equilibration of the excited state.
However, even in the electron transfer process (right part of figure A.5), the electron motion from donor to acceptor (horizontal transition) takes place so rapidly that the formation of the transition state can be considered not involving any appreciable nuclear motion [91]. The resulting state can be defined as a Frank-Condon-like radical ion pair ($[D^+ + A^-]_{TS}$). This state subsequently evolves to the equilibrated product state ($[D^+ + A^-]_{eq}$), with the nuclear relaxation of the molecule and the reorganization of the surrounding solvent molecules around the different nuclear geometry (figure A.5). The electron is transferred between the moieties without any nuclear motion during the transfer and without any release of energy. Only in this way, the total energy and momentum of the system are conserved.
Before electron transfer takes place from donor to acceptor, the system energy grows with formation of an initial transition state $[D^* + A]_{TS}$ (figure A.6).

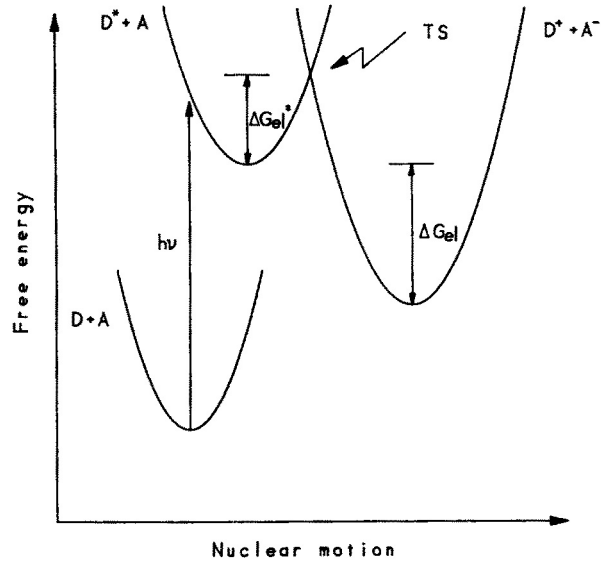

Figure A.6: Representation of PET process trough the parabolic relationship between free energy changes and nuclear motion . The three curves represent the ground state system of donor and acceptor, the excited state in which the photoexcited donor interacts with the acceptor (precursor state of PET) and the following ionic state after the electron transfer (successor state) [1].

The energy $\Delta G_{el}^{\neq}$ of the TS is required for the proceeding of the reaction and it is designed as *free activation energy*. $\Delta G_{el}^{\neq}$ is supplied by vibrational collisions between reacting molecules and neighboring solvent molecules, and it is a fundamental electron transfer condition in the classical Marcus theory of PET process. A brief description of this parameter is following reported.

Free activation energy

Free activation energy can be found in the expression of the kinetic constant for electron transfer:

$$k_{el} = \nu_n \cdot \kappa_{el} \cdot e^{\frac{\Delta G_{el}^{\neq}}{RT}} \tag{A.17}$$

As already evidenced in equation (A.16), the actual free activation energy of electron transfer ($\Delta G_{el}^{\neq}$) is related to the nuclear factor. In fact, bond changes taking place during the transition state formation and solvent orientation changes in the surrounding medium determine the nature and magnitude of the energy of TS. The total free energy can be so considered as the sum of two distinct contributions: one referring to vibrations within the reactants ($\Delta G_{v}^{\neq}$) and the other to solvent changes ($\Delta G_{s}^{\neq}$):

$$\Delta G_{el}^{\neq} = \Delta G_{v}^{\neq} + \Delta G_{s}^{\neq} \tag{A.18}$$

The chemist Rudolph A. Marcus inserted these two separated contributions inside the famous quadratic relationship taking afterwords his name (A.19).

$$\Delta G_{el}^{\neq} = \frac{\lambda}{4}\Big(1 + \frac{\Delta G_{el}}{\lambda}\Big) \tag{A.19}$$

In fact, the quadratic relationship associates the free activation energy for electron transfer ($\Delta G_{el}^{\neq}$) to the driving force ΔG_{el} and the nuclear reorganizational energy $\lambda = \lambda_v + \lambda_s$ (figure A.7).

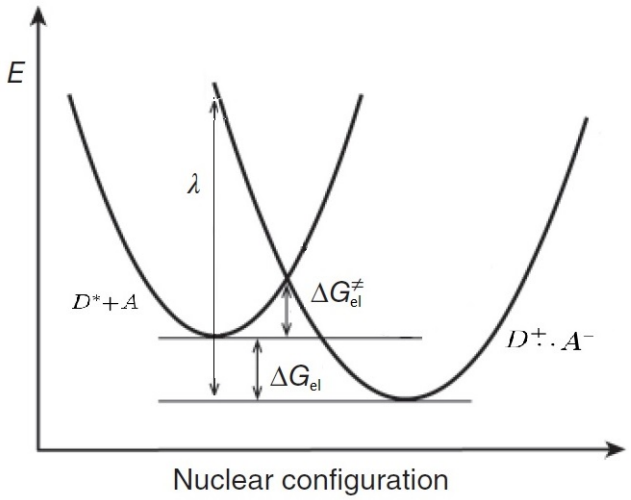

Figure A.7: Parabolic potential energy for a PET process, with the specification of the different energetic parameters of Marcus quadratic relationship [17].

The total reorganizational energy is expressed as the sum of the two vibrational and orientation contributes previously mentioned:

$$\lambda = \lambda_v + \lambda_s \tag{A.20}$$

The term λ_v is the reorganizational energy due to bond lengths and bond angles changes of reactants during the electron migration, while λ_s is the energy change associated to the solvent dipoles reorientation around the reagents. The energy required to overcome the transition state energy barrier is transferred from the thermal environment to the vibrational modes of reactants as well as from solvent molecules.
Both contributions ΔG_{el} and λ can be calculated thanks to experimental and theoretical considerations. The driving force defined in the Rehm-Weller equation (A.9) can be easily extrapolated from the system. The standard redox potentials of donor and acceptor are evaluated thanks to an electrochemical study in solution ($E^0(D^+/D), E^0(A/A^-)$), the energy donor (or acceptor) excited state is obtained from emission studies (ΔG_{00}), and molecules radii and solvent dielectric constant are experimentally calculated ($\frac{e^2}{\epsilon d}$).
Bond reorganization contribution (λ_v) can be evaluated thanks to calculations with the approximation of an harmonic behavior of all vibrational states. *Solvent reorganization* (λ_s) instead, can be calculated thanks to an expression where the reactants and product are considered as spheroidal molecules in a dielectric medium and where an inverse dependence to the dielectric constant of the solvent is highlighted. The energy contribution to the barrier generated by solvent polarity is due to the effect of solvent electron clouds that, during electron transfer, respond immediately to changes in charge distribution of the transition state (fast contribution).
Two important consideration must be done about Marcus quadratic relationship (A.19). This relation is valid only by assuming parabolic potential energy curves

for the different molecular states, with all reactive nuclear modes purely classical, and it is valid only in the so-called weakly adiabatic case in which κ_{el} value is in an intermediate region ($0 < \kappa_{el} < 1$). In the weak case donors and acceptors are close enough to have a direct and sufficient orbital overlap, experiencing an electronic interaction within distances of ~ 7Å.
Replacing Marcus quadratic relationship in the expression for the kinetic constant of electron transfer we obtain the global relation

$$k_{el} = \nu_n \cdot \kappa_{el} \cdot e^{\frac{\lambda}{4}\left(1+\frac{\Delta G_{el}}{\lambda}\right)/RT} \tag{A.21}$$

The equation (A.21) shows the direct relationship between the rate constant of PET process and its driving force (ΔG_{el}). Considering a series of homogeneous reactions (reactions having the same λ and $\kappa_{el} \sim 1$ values) and the relationship between their $\ln k_{el}$ and driving force, it is possible to identify three different regimes for PET reaction:

1. If $-\lambda < \Delta G_{el} > 0$, PET takes place in a *normal* regime in which the process is thermally activated and the value of $\ln k_{el}$ increases with an increase in driving force (right part of the graphic in figure A.8).

2. If $\Delta G_{el} = -\lambda$, PET process is in the *activationless* regime in which any change in driving force does not determine a large change in the reaction rate (central region of the bell-shape curve in figure A.8).

3. If $\Delta G_{el} < \lambda$, the electron transfer shows a counterintuitive behavior, because for driving force further increasing $\ln k_{el}$ progressively decreases; the regime is defined as *inverted* and it is associated to strongly exergonic processes (left part of the graphic in figure A.8).

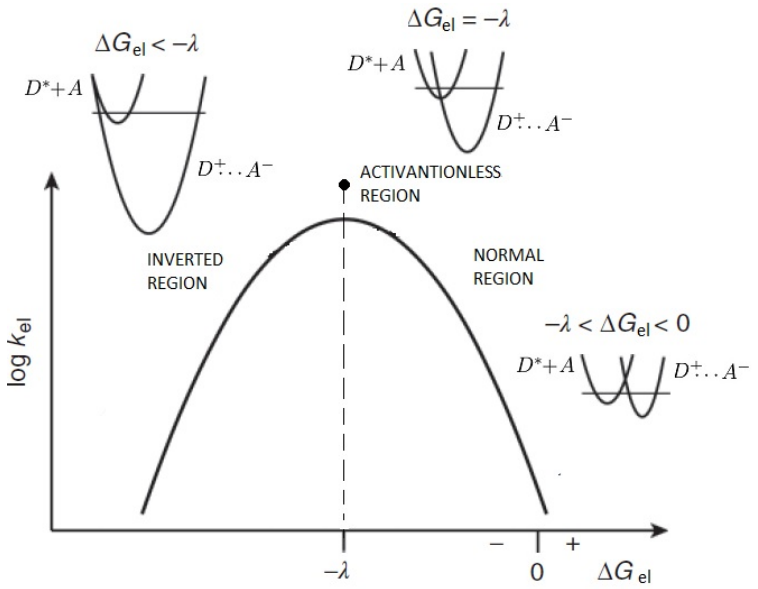

Figure A.8: Relationship between the electron transfer rate constant and the driving force of a PET process according to Marcus quadratic expression. Each regime has been evidenced by the bell-shape curve and by the insertion of the interactive parabolic potentials of reactant and product states [17].

PET in the *normal regime* requires thermal fluctuations to proceed. Electron transfer takes place only when the potential energy of the reactant nuclear configuration and that of its surrounding medium, is equal to that of the product and its surrounding (potential curves crossing point).
However, looking at the bell-shape curve that describes the relationship between $\ln k_{el}$ and the driving force, it is evident that the reaction rate attains its maximum value in the *activationless regime*, where $\Delta G_{el} = -\lambda$ or $\Delta G_{el}^{\neq} = 0$. Only in this condition, a thermal activation of the process is not required and the electron transfer can take place rapidly even with a wide electronic coupling. After this maximum of driving force, the increasing of exothermicities does not determine a reduction of the activation energy for the process but an inversion of the reaction speed.
However, in photoinduced electron transfer the *inverted region* has an important role, most of all considering its implication in the aim of controlling the processes of direct charge separation and back electron transfer. In fact, the relationship between the driving force and the reorganisational energy of the system can be used to control in which regime the forward electron migration can be found instead of the *back electron transfer*. The possibility to influence, for example with a change of solvent conditions, the magnitude of λ lets to prevent or promote one process with respect to the other.

A.3.2 Quantum mechanical theory

Marcus theory is not able to explain electron transfer processes where reactants are separated by large distances and are characterized by weak electronic coupling. However, these strongly nonadiabatic PET processes are numerous and they could even take place at rate hugely faster that one would predict using only classical treatments.
The huge nuclear and electronic barriers that make strongly nonadiabatic reactions forbidden in classical theories are penetrated by the possibility of a quantum jump from reactants to products potential surfaces. This quantum mechanical phenomenon is called *tunneling* and it can be differentiated in nuclear tunneling and electron tunneling [1]. Both of them provide a pathway for classically prohibited electron transfer.
In *nuclear tunneling*, the reaction coordinate passes through the transition state barrier when thermal energy is insufficient to exceed the barrier.The isoenergetic transition from the reactant to the product surface requires the coupling of the nuclear wavefunctions of reactant and product vibrational modes. This coupling depends on the electron coupling matrix H_{el} and the vibrational overlap integral of those modes of the product that are able to accept the exothermic energy resulting from electron transfer. Both nuclear bond deformations (inner modes) and vibrations and rotational motions of the solvent molecules (outer modes) contribute to the optical waves (phonons) that control the electron transfer rate.
For this reason, quantum mechanical theory describes PET process throughout the Fermi Golden Rule expression that gives the electronic constant of a *radiationless transition* between two eigenstates:

$$k_{el} = \frac{2\pi}{\hbar} \langle \Psi_{D^*A} | \hat{H}_{el} | \Psi_{D^+A^-} \rangle^2 FC^{el} \tag{A.22}$$

FC is the Franck-Condon factor, representing the weighted density of final states at the initial energy. It contains the sum of all overlap integrals of nuclear wavefunctions of initial and final states at the same energy, considering both inner and outer vibrational modes (A.23).

$$FC \propto \sum_{v} \sum_{w} \rho_v |\langle \chi_i | \chi_f \rangle|^2 \delta(E_{iw} - E_{fv}) \tag{A.23}$$

In this expression, w and v are the vibrational levels of the initial and final state, χ designates the nuclear wavefunction, ρ_v is the v level population density and $\delta(E_{iw} - E_{fv})$ is the energy difference between the w and v level.
Looking at the equation, it is evident that the transition corresponding to the greatest overlap between vibrational wavefunctions is the one much more favored. This overlap is strongly dependent on the separating distance among the reactants, that instead in the H_{el} factor appears with an opposite proportionality.
Considering the tunneling dependence on the system temperature, it is possible to separate two different limits for thermodynamic conditions.
In the high-temperature limit, where the thermal energy is bigger than the energy required for the vibration ($k_B T > \hbar\nu$), a sufficiently accurate *classical* approximation reduces FC expression to:

$$FC = \frac{exp[-(\Delta G_{el} + \lambda)^2 / 4\lambda k_B T]}{(4\pi\lambda k_B T)^{1/2}} \tag{A.24}$$

Combining this equation with k_{el} expression (A.22), the same exponential quadratic relation described by Marcus theory appears evident. For this reason, even the quantum theory at high temperature lets to differentiate the three distinct kinetic regimes of the classical treatment. However, one difference can be found in the inverted regime where the mechanical model predicts a nearly *linear* rather than *parabolic* decrease of PET rate parameter with the increasing of the reaction exothermicity (figure A.9).

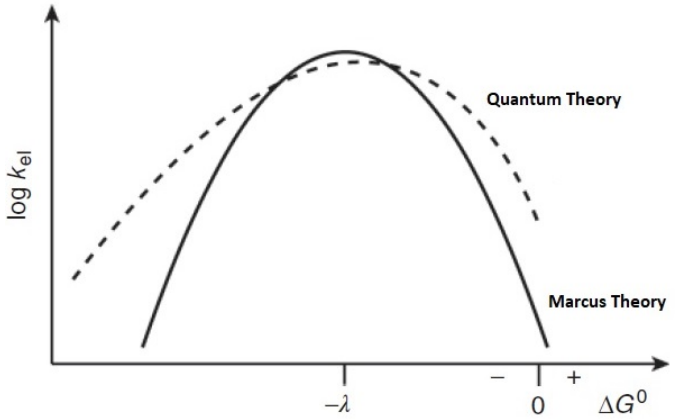

Figure A.9: Difference in the relationship between k_{el} and the driving force according to Marcus theory and quantum mechanical theory [17].

In the low-temperature limit, thermal energy is lower than the vibrational energy required for electron transfer ($k_B T < \hbar\nu$). In these conditions and when it is possible to approximate nuclear vibrations to a single effective harmonic

oscillator (ν_{eff}), FC factor can be written as:

$$FC = \frac{(\lambda/\hbar\nu_{eff})^{-\Delta G_{el}/\hbar\nu_{eff}} \quad e^{-(\lambda/\hbar\nu_{eff})}}{(-\Delta G_{el}/\hbar\nu_{eff})!} \tag{A.25}$$

This expression underlines that when thermal energy is unable to determine the overcome of the activation energy, a bond-length change (ν_{eff}) , that involves a high-frequency nuclear inner or outer vibration, determines the nonthermal electron transfer throughout nuclear tunneling effect [1].

Appendix B

Insights of solar cells and LSCs

Luminescent solar concentrators are one of the possible devices designed to lower the cost for the production of photovoltaic electricity and to replace the so more available and less expensive fossil fuels. Their innovation was presented already several decades ago but only recently, with the rising of the fuel cost and global warming, the interest on them is renewed drastically.
There are different generations of solar cells, but the one that is still dominating the market is the single/multi-crystalline silicon solar cells. In these devices, the semiconductor is silicon and the electric field is created at the junction of two regions of the lattice having contrasting types of conductivity. The different conductivity of the two regions is permitted by doping with two elements that differs in number of valence electrons. The different concentration of electrons and holes causes a permanent electric field that is directed from the region with more valence electrons (the n-type) to that with more numbers of holes (the p-type).
The p-n junction in silicon cells is generally obtained by diffusing a layer of phosphorus atoms (more valence electrons) into a wafer of silicon doped with boron. An extremely simplified scheme of a silicon solar cell is following reported in figure B.1.

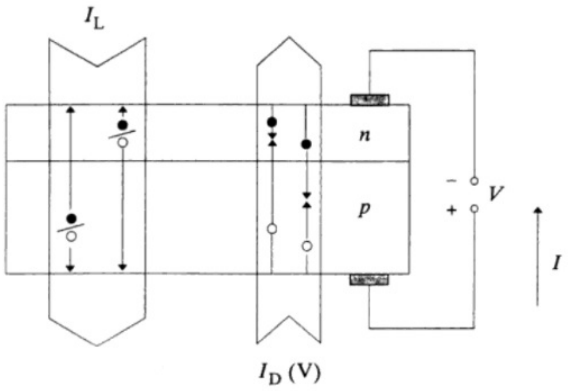

Figure B.1: Scheme of a solar cells with the specification of internal currents. The white circle represent the holes while the black ones are the electrons [45].

Looking at the scheme of a solar cell, the sequential events that operate in the creation of the electric current can be described in three steps:

1. At first the photons reach the interior of the cell and only those that have an

energy equal or greater than the bandgap of the semiconductor are absorbed, generating the electron-hole pairs called excitons.

2. In the second step the potential difference created by the p-n junction separates the carriers before their chance of recombining and determines the flow of a current inside the net to the cathode and anode of the cell (I_L).

3. At third, there is a counteractive event that obstacle this current and that is due to the presence of an external voltage across the terminal of the devices. This potential difference is necessary to deliver the power to the load and it determines the recombinations of the excitons. This contribution can be defined as a dark current (I_D) and it represents a big part of the loss of the cell.

Obviously a solar cell with a maximum value of light absorption and a minimal number of charge carrier recombination achieves the best performances.

B.1 Main losses of LSCs devices

LSCs are static and brightly colored block that collect the solar light and concentrate it onto the edges. Here, PV cells mounted onto the side of the waveguide converts the collected light in electrical current.
The light emitted by the molecules of the dye is omnidirectional and only that part emitted in the total internal reflection angle (TIR) is finally gathered at the edges. The definition of the loss cone of TIR depends on the refractive index of the matrix material chosen for the device [54] (figure B.3).

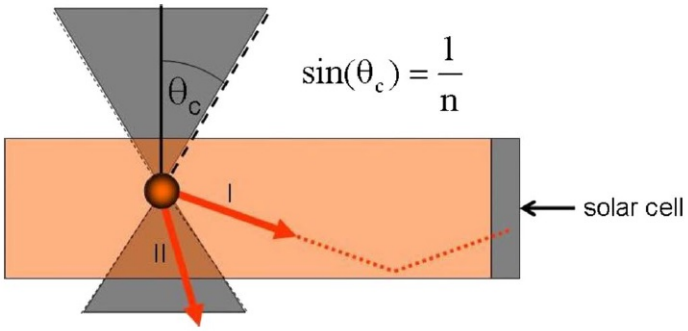

Figure B.2: Representation of the section of a LSC device with the sketch of the loss angle TIR. [54].

Only the light emitted with an angle greater than the critical angle θ_c is totally reflected (I direction in figure). All that emitted with an angle smaller than θ_c experience the Fresnel reflections, determining an important fraction loss for the concentrator (II direction in figure). This fraction of light lost inside the so called loss-cone depends on the emission characteristic of the dye dispersed in the matrix. If we assume an isotropic emission, the fraction can be ascribed to the 26% of all the light getting inside the concentrator [54].
Together with the difficulty for the luminescence emitted to escape beyond the critical angle, several other minor mechanisms increase the fraction lost. Among

them an important contribution is given by the self-absorption phenomena due to the unavoidable overlapping of the absorption and luminescence of the dye. The fluorophore is one of the crucial factors determining the device performance that until now seem not to overcome the 8.1% PCE superior limit [63] [53]. The numerous events preventing a fraction of light from reaching the solar cell are presented in the following figure.

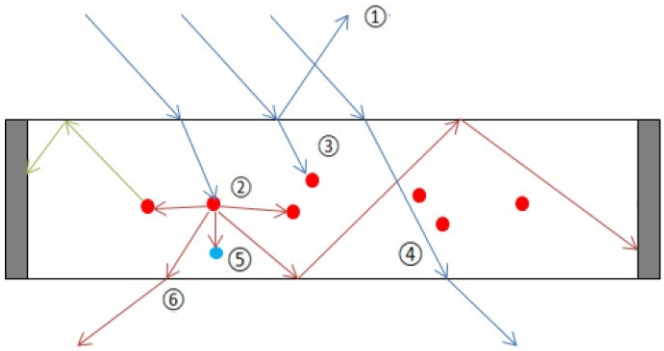

Figure B.3: Representation of the LSC different loss mechanisms. Red dots represents the dye molecules, blue dots represent host absorption while blue arrows represent the incident light [93].

When light hits the top of the device surface, a part is reflected by the surface of the plate and it does not achieve the inside matrix (1). Light entered in the matrix is absorbed by the dye molecules and re-emitted. If the absorption spectrum overlaps the emission, part of the fluorescence is re-adsorbed by other dye molecules (2) or host material (3). The light absorbed a second time by the dye can go partially lost due to the limited emission quantum yield of the dye, because it is transformed to heat and vibrations. In the same way of entering, another part of the transmitted light is re-trasmitted at the bottom of the device, out of the surface of the waveguide (4). The same path is followed by that part of the light emitted by the dye at an angle smaller than the critical angle (6, TIR loss).

Bibliography

[1] George J. Kavamos *Fundamentals of Photoinduced Electron Transfer*. VCH Publishers, Inc., 1993

[2] Robert W. Boyd *Nonlinear optics* San Diego, CA: Academic Press, 2003

[3] Di Donato M, Segado Centellas M, Lapini A, Lima M, Avila F, Santoro F, Cappelli C, Righini R.; *Combination of transient 2D-IR experiments and ab initio computations sheds light on the formation of the charge-transfer state in photoexcited carbonyl carotenoids.* J Phys Chem B. 2014;118(32):9613-30.

[4] Snellenburg JJ, Laptenok SP, Seger R, Mullen KM, van Stokkum IHM;*Glotaran: A Java-Based Graphical User Interface for the R Package TIMP*; Journal of Statistical Software, 2012, 49, 3

[5] Jianzhang Zhao,Wanhua Wu, Jifu Sun, Song Guo; *Triplet photosensitizers: from molecular design to applications*; Chem. Soc. Rev., 2013, 42, 5323

[6] Samuel G. Awuahab, Youngjae You; *Boron dipyrromethene (BODIPY)-based photosensitizers for photodynamic therapy*; RSC Adv., 2012,2, 11169-11183

[7] Christopher K. Prier, Danica A. Rankic, David W. C. MacMillan; *Visible Light Photoredox Catalysis with Transition Metal Complexes: Applications in Organic Synthesis* Chem. Rev. 2013 , 113, 5322-5363

[8] A. Monguzzi, D. Braga, M. Gandini, V. C. Holmberg, D. K. Kim, A. Sahu, D. J. Norris, F. Meinardi; *Broadband Up-Conversion at Subsolar Irradiance: Triplet–Triplet Annihilation Boosted by Fluorescent Semiconductor Nanocrystals* Nano Letters 2014 14 (11), 6644-6650

[9] Tanya N. Singh-Rachford, Felix N. Castellano; *Photon upconversion based on sensitized triplet–triplet annihilation*; Coordination Chemistry Reviews 254 (2010) 2560-2573

[10] Ira N. Levine; *Physical Chemistry*;Published by McGraw-Hill (2009), Inc., 1221 Avenue of the Americas, New York

[11] David Oxtoby; H. Gillis; Alan Campion; *Principles of Modern Chemistry* 6 edition 2007, Cengage Learning. p. 990.

[12] Emilie M. Giacobbe, Qixi Mi, Michael T. Colvin, Boiko Cohen, Charusheela Ramanan, Amy M. Scott, Sina Yeganeh, Tobin J. Marks, Mark A. Ratner, and Michael R. Wasielewski; *Ultrafast Intersystem Crossing and Spin Dynamics of Photoexcited Perylene-3,4:9,10-bis(dicarboximide) Covalently*

Linked to a Nitroxide Radical at Fixed Distances; J. Am. Chem. Soc. 2009, 131, 3700–3712.

[13] Yuqi Hou, Xue Zhang, Kepeng Chen, Dongyi Liu, Zhijia Wang, Qingyun Liu, Jianzhang Zhaoa, Antonio Barbond; *Charge Separation, Charge Recombination, Long-Lived Charge Transfer State and Intersystem Crossing in Organic Electron Donor-Acceptor Dyads* J. Mater. Chem. C., 2019, 7, 12048-12074.

[14] Y. Kobori, K. Takeda, K. Tsuji, A. Kawai, K. Obi *Exchange Interaction in Radical-Triplet Pairs: Evidences for CIDEP Generation by Level Crossings in Triplet-Doublet Interactions* The Journal of Physical Chemistry A 1998 102 (27), 5160-5170

[15] Jan W. Verhoeven; *On the role of spin correlation in the formation, decay, and detection of long-lived, intramolecular charge-transfer states* Journal of Photochemistry and Photobiology C: Photochemistry Reviews 7 (2006) 40–60

[16] Z. E. X. Dance, Q. Mi, D. W. McCamant, M. J. Ahrens, M. A. Ratner, M. R. Wasielewski; *Time-Resolved EPR Studies of Photogenerated Radical Ion Pairs Separated by p-Phenylene Oligomers and of Triplet States Resulting from Charge Recombination* J. Phys. Chem. B, 2006, 110, 25163-25173.

[17] V. Balzani, P. Ceroni, A. Juris *Photochemistry and Photophysics.* Wiley-VCH Verlag GmbH & Co, 2014

[18] Z. E. X. Dance, S. M. Mickley, T. M. Wilson, A. B. Ricks, A. M. Scott, M. A. Ratner, M. R. Wasielewski; *Intersystem Crossing Mediated by Photoinduced Intramolecular Charge Transfer: Julolidine-Anthracene Molecules with Perpendicular σ Systems* J. Phys. Chem. A., 2008, 112, 4194-4201.

[19] Mikhail A. Filatov; *Heavy-atom-free BODIPY photosensitizers with intersystem crossing mediated by intramolecular photoinduced electron transfer*; Org. Biomol. Chem., 2020, 18, 10.

[20] Zhijia Wang and Jianzhang Zhao; *Bodipy–Anthracene Dyads as Triplet Photosensitizers: Effect of Chromophore Orientation on Triplet-State Formation Efficiency and Application in Triplet–Triplet Annihilation Upconversion*; Org. Lett. 2017, 19, 17, 4492–4495.

[21] N. Rehmat, A. Toffoletti, Z. Mahmood, X. Zhang, J. Zhao, and A. Barbon; *Carbazole-perylenebisimide electron donor/acceptor dyads showing efficient spin orbit charge transfer intersystem crossing (SOCT-ISC) and photodriven intermolecular electron transfer* J. Mater. Chem. C, 2020,8, 4701-4712

[22] Yu Dong, Maria Taddei, Sandra Doria, Laura Bussotti, Jianzhang Zhao, Gloria Mazzone, and Mariangela Di Donato; *Torsion-Induced Nonradiative Relaxation of the Singlet Excited State of meso-Thienyl Bodipy and Charge Separation, Charge Recombination-Induced Intersystem Crossing in Its Compact Electron Donor/Acceptor Dyads*; J. Phys. Chem. B 2021, 125, 18, 4779–4793.

[23] K. Chen, M. Taddei, L. Bussotti, P. Foggi, J. Zhao, M. Di Donato; *Near-IR-Absorbing BODIPY-5,10-Dihydrophenazine Compact Electron Donor/Acceptor Dyads and Triads: Spin-Orbit Charge Transfer Intersystem Crossing and Charge-Transfer State* ChemPhotoChem 2020, 4, 487.

[24] M. Imran, A. M. El-Zohry, C. Matt, M. Taddei, S. Doria, L. Bussotti, P. Foggi, J. Zhao, M. Di Donato, O. F. Mohammed, S. Weber; *Intersystem Crossing via Charge Recombination in a Perylene- Naphthalimide Compact Electron Donor/Acceptor Dyad*;J. Mater. Chem. C, 2020,8, 8305-8319.

[25] D. Liu, A. M. El-Zohry, M. Taddei, C. Matt, L. Bussotti, Z. Wang, J. Zhao, O. F. Mohammed, M. Di Donato, S. Weber; *Long-Lived Charge-Transfer State Induced by Spin-Orbit Charge Transfer Intersystem Crossing (SOCT-ISC) in a Compact Spiro Electron Donor/Acceptor Dyad* Angew. Chem. Int. Ed. 2020, 59, 11591.

[26] Zafar Mahmood, Maria Taddei, Noreen Rehmat, Laura Bussotti, Sandra Doria, Qinglin Guan, Shaomin Ji, Jianzhang Zhao, Mariangela Di Donato, Yanping Huo, and Yong Heng Xing; *Color-Tunable Delayed Fluorescence and Efficient Spin-Orbit Charge Transfer Intersystem Crossing in Compact Carbazole-Anthracene-Bodipy Triads Employing the Sequential Electron Transfer Approach*; J. Phys. Chem. C 2020, 124, 5944-5957

[27] Akio Kawai, Kazuhiko Shibuya; *Electron spin dynamics in a pair interaction between radical and electronically-excited molecule as studied by a time-resolved ESR method*; Photochemistry Reviews 7 (2006) 89–103

[28] Xue Zhang, Andrey A. Sukhanov, Elif Akhuseyin Yildiz, Yuri E. Kandrashkin, Jianzhang Zhao, Halime Gul Yaglioglu, and Violeta K. Voronkova; *Radical Enhanced Intersystem Crossing in Bay-Substituted Perylenebisimide-TEMPO Dyad and the Electron Spin Polarization Dynamics Upon Photoexcitation*; ChemPhysChem2021, 22, 55–68 .

[29] Vinayak Rane and Ranjan Das; *Distance Dependence of Electron Spin Polarization during Photophysical Quenching of Excited Naphthalene by TEMPO* Radical; J. Phys. Chem. A 2015, 119, 22, 5515–5523

[30] Mushraf Hussain, Maria Taddei, Laura Bussotti, Paolo Foggi, Jianzhang Zhao, Qingyun Liu, and Mariangela Di Donato; *Intersystem Crossing in Naphthalenediimide–Oxoverdazyl Dyads: Synthesis and Study of the Photophysical Properties*; Chem. Eur. J. 2019, 25, 1 – 14.

[31] Y. Teki, H. Tamekuni, K. Haruta, J. Takeuchi, Y. Miura; *Design, synthesis, and uniquely electron-spin-polarized quartet photo-excited state of a π-conjugated spin system generated via the ion-pair state* ; J. Mater. Chem. 2008, 18, 381– 391.

[32] Y. Teki, M. Kimura, S. Narimatsu, K. Ohara, K. Mukai;*Excited High-Spin Quartet ($S = 3/2$) State of a Novel π-Conjugated Organic Spin System, Pyrene–Verdazyl Radical* ; Bull. Chem. Soc. Jpn. 2004, 77, 95–99..

[33] Z. Wang, J. Zhao, A. Barbon, A. Toffoletti, Y. Liu, Y. An, L. Xu, A. Karatay, H. G. Yaglioglu, E. A. Yildiz, M. Hayvali; *Radical-Enhanced Intersystem Crossing in New Bodipy Derivatives and Application for Efficient Triplet–Triplet Annihilation Upconversion*; J. Am. Chem. Soc. 2017, 139, 7831 –7842.

[34] S. M. Dyar, E. A. Margulies, N. E. Horwitz, K. E. Brown, M. D. Krzyaniak, M. R. Wasielewski, *Photogenerated Quartet State Formation in a Compact Ring-Fused Perylene-Nitroxide*; J. Phys. Chem. B 2015, 119, 13560 –13569.

[35] Norikazu Mizuochi, Yasunori Ohba, and Seigo Yamauchi; *First Observation of the Photoexcited Quintet State in Fullerene Linked with Two Nitroxide Radicals*; J. Phys. Chem. A, 1999, Vol. 103, No. 39

[36] Imran M., Taddei M., Sukhanov A..A., Bussotti L., Ni W., Foggi P., Gurzadyan G..G., Zhao J., Di Donato M. and Voronkova V..K.; *Radical-Enhanced Intersystem Crossing in Perylene-Oxoverdazyl Radical Dyads.*, ChemPhysChem (2022).

[37] Sakai, N.; Mareda, J.; Vauthey, E.; Matile, S; *Core-substituted naphthalenediimides*; Chem. Commun., 2010, 46 , 4225 4237

[38] Chattopadhyay, S. K.; Das, P. K.; Hug, G. L. ; *Photoprocesses in diphenylpolyenes. 2. Excited-state interactions with stable free radicals*; J. Am. Chem. Soc. 1983, 105, 6205–6210.

[39] Mie Saotome, Satoko Takano, Asako Tokushima, Syoji Ito, Satoru Nakashima, Yutaka Nagasawa, Tadashi Okada and Hiroshi Miyasaka; *Picosecond–nanosecond laser photolysis studies of a photoacid generator in solutions: Transient absorption spectroscopy and transient grating measurements*; Photochem. Photobiol. Sci., 2005,4, 83-88

[40] T. Higashino, T. Yamada, M. Yamamoto, A. Furube, N. V. Tkachenko, T. Miura, Y. Kobori, R. Jono, K. Yamashita, H. Imahori; *Remarkable Dependence of the Final Charge Separation Efficiency on the Donor-Acceptor Interaction in Photoinduced Electron Transfer* Angew. Chem. Int. Ed. 2016, 55, 629-633.

[41] Zhijia Wang and Jianzhang Zhao; *Bodipy–Anthracene Dyads as Triplet Photosensitizers: Effect of Chromophore Orientation on Triplet-State Formation Efficiency and Application in Triplet–Triplet Annihilation Upconversion*; Organic Letters 2017 19 (17), 4492-4495

[42] Filatov M. A.; Karuthedath S.; Polestshuk P. M.; Savoie H.; Flanagan K. J.; Sy C.; Sitte E.; Telitchko M.; Laquai F.; Boyle R. W.; et al. *Generation of Triplet Excited States via Photoinduced Electron Transfer in meso-anthra-BODIPY: Fluorogenic Response toward Singlet Oxygen in Solution and in Vitro.*; J. Am. Chem. Soc. 2017, 139, 62826285.

[43] Filatov M. A.; Karuthedath S.; Polestshuk P. M.; Callaghan S.; Flanagan K. J.; Telitchko M.; Wiesner T.; Laquai F.; Senge M. O.; *Control of triplet state generation in heavy atom-free BODIPY-anthracene dyads by media polarity and structural factors.*; Chem. Phys. 2018, 20, 80168031.

[44] Niladari Raju, M. V.; Mohanty, M. E.; Bangal, P. R.; Vaidya, J. R.; *Synthesis and Ultrafast Dynamics of a Donor-Acceptor-Donor Molecule Having Optoelectronic Properties.*; J. Phys. Chem. C. 2015, 119, 8563-8575.

[45] E. Lorenzo et al; *Solar Electricity: Engineering of Photovoltaic Systems.* Progensa, 1994.

[46] Jozef szlufcik et al.; *Low-Cost Industrial Technologies of Crystalline Silicon Solar Cells*; Proceedings of the IEEE, vol. 85, no. 5, pp. 711-730, 1997.

[47] Gratzel M., *Dye-sensitized solar cells.* Journal of Photochemistry and Photobiology C-Photochemistry Reviews 2003, 4, 145-153.

[48] Carey G. H.; Abdelhady A. L.; Ning Z. J.; Thon S. M.; Bakr O. M.; Sargent E. H., *Colloidal Quantum Dot Solar Cells.* Chemical Reviews 2015, 115, 12732-12763.

[49] Dou L. T.; You, J. B.; Hong, Z. R.; Xu, Z.; Li, G.; Street, R. A.; Yang, Y., *A Decade of Organic/Polymeric Photovoltaic Research.* Advanced Materials 2013, 25, 6642-6671.

[50] Yang S. D.; Fu W. F.; Zhang Z. Q.; Chen H. Z.; Li, C. Z., *Recent advances in perovskite solar cells: efficiency, stability and lead-free perovskite.* Journal of Materials Chemistry A 2017, 5, 11462-11482.

[51] Shin Woei Leow, Carley Corrado, Melissa Osborn, Michael Isaacson, Glenn Alers, Sue A. Carter; *Analyzing luminescent solar concentrators with front-facing photovoltaic cells using weighted Monte Carlo ray tracing*; Journal of Applied Physics, 2013, 113, 214510

[52] Finn M. Vossen, Mariëlle P.J. Aarts, Michael G. Debije, *Visual performance of red luminescent solar concentrating windows in an office environment*; Energy and Buildings, Volume 113, 2016, Pages 123-132

[53] I. Papakonstantinou, M. Portnoi, M. G. Debije; *The Hidden Potential of Luminescent Solar Concentrators*; Adv. Energy Mater. 2020, 2002883

[54] M. Peters, J. C. Goldschmidt, P. Löper, B. Bläsi, A. Gombert; *The effect of photonic structures on the light guiding efficiency of fluorescent concentrators*; J. Appl. Phys., 2009, 105, 014909

[55] Yilin Li, Xueqiao Zhang, Yongcao Zhang, Richard Dong, Christine K. Luscombe; *Review on the Role of Polymers in Luminescent Solar Concentrators*; J. Polym. Sci. Part A: Polym. Chem., 2019, 57, 201-215s

[56] Francisco José Ostos, Giuseppe Iasilli, Marco Carlotti, Andrea Pucci; *High-Performance Luminescent Solar Concentrators Based on Poly(Cyclohexylmethacrylate) (PCHMA) Films*;Polymers 2020, 12, 2898

[57] A. Goetzberger and W. Greubel; *Solar Energy Conversion with Fluorescent Collectors*; Appl. Phys. 14, 123–139 (1977)

[58] R. Reisfeld, *New developments in luminescence for solar energy utilization*, Optical Materials, Volume 32, Issue 9, 2010, Pages 850-856

[59] Mingying Peng and Lothar Wondraczek; *Bismuth-doped oxide glasses as potential solar spectral converters and concentrators*; J. Mater. Chem., 2009,19, 627-630

[60] X. Wang, T. X. Wang, X. J. Tian, L. J. Wang, W. X. Wu, Y. H. Luo and Q. J. Zhang; *Quantum dots for Luminescent Solar Concentrators*; Sol. Energy, 2011, 85, 2179–2184.

[61] C. L. Mulder, L. Theogarajan, M. Currie, J. K. Mapel, M. A. Baldo, M. Vaughn, P. Willard, B. D. Bruce, M. W. Moss, C. E. McLain and J. P. Morseman; *Luminescent Solar Concentrators Employing Phycobilisomes* Adv. Mater., 2009, 21, 3181.

[62] A. Sanguineti, M. Sassi, R. Turrisi, R. Ruffo, G. Vaccaro, F. Meinardi, L.Beverina; *High Stokes shift perylenedyes for luminescent solar concentrators* Chem. Commun. 2013, 49, 1618–1620.

[63] Barry McKenna and Rachel C. Evans; *Towards Efficient Spectral Converters through Materials Design for Luminescent Solar Devices*; Adv. Mater. 2017, 1606491

[64] Costanza Papucci, Tristan A. Geervliet, Daniele Franchi, Ottavia Bettucci, Alessandro Mordini, Gianna Reginato, Francesco Picchioni, Andrea Pucci, Massimo Calamante, Lorenzo Zani; *Green/Yellow-Emitting Conjugated Heterocyclic Fluorophores for Luminescent Solar Concentrators* Eur. J. Org. Chem. 2018, 2657–2666

[65] Costanza Papucci, Alessio Dessì, Carmen Coppola, Adalgisa Sinicropi, Greta Santi, Mariangela Di Donato, Maria Taddei, Paolo Foggi, Lorenzo Zani, Gianna Reginato, Andrea Pucci, Massimo Calamante, Alessandro Mordini; *Benzo[1,2-d:4,5-d']bisthiazole fluorophores for luminescent solar concentrators: synthesis, optical properties and effect of the polymer matrix on the device performances* Dyes and Pigments, Volume 188, 2021, 109207

[66] Lidia Marin, Laurence Lutsen, Dirk Vanderzandea, and Wouter Maes; *Quinoxaline derivatives with broadened absorption patterns*; Org. Biomol. Chem., 2013, 11, 5866

[67] Yongzhen Wu and Weihong Zhu; *Organic sensitizers from D–p–A to D–A–p–A: effect of the internal electron-withdrawing units on molecular absorption, energy levels and photovoltaic performances*; Chem. Soc. Rev., 2013,42, 2039-2058

[68] Gianmarco Griffini; *Host Matrix Materials for Luminescent Solar Concentrators: Recent Achievements and Forthcoming Challenges*; Front. Mater. 2019, 6, 29.

[69] Xing Li, Yue Hu, Irene Sanchez-Molina, Ying Zhou, Fengtao Yu, Saif A. Haque, Wenjun Wu, Jianli Hua, He Tiana and Neil Robertson; *Insight into quinoxaline containing $D^{\smile}\pi^{\smile}A$ dyes for dye-sensitized solar cells with cobalt and iodine based electrolytes: the effect of π-bridge on the HOMO energy level and photovoltaic performance*; J. Mater. Chem. A, 2015,3, 21733-21743

[70] M. G. Debije, R. C. Evans and G. Griffini; *Laboratory protocols for measuring and reporting the performance of luminescent solar concentrators*; Energy Environ. Sci., 2021, 14, 293–301

[71] Costanza Papucci, Rima Charaf, Carmen Coppola, Adalgisa Sinicropi, Mariangela di Donato, Maria Taddei, Paolo Foggi, Antonella Battisti, Bastiaan de Jong, Lorenzo Zani, Alessandro Mordini, Andrea Pucci, Massimo Calamante and Gianna Reginato; *Luminescent solar concentrators with outstanding optical properties by employment of D–A–D quinoxaline fluorophores*; J. Mater. Chem. C, 2021, 9, 15608

[72] Andréasson J. , Pischel U.; *Storage and Processing of Information Using Molecules: The All-Photonic Approach with Simple and Multi-Photochromic Switches.* Israel Journal of Chemistry (2013), vol. 53(5), pp. 236-246.

[73] Heilemann, M., Dedecker, P., Hofkens, J. and Sauer, M. ; *Photoswitches: Key molecules for subdiffraction-resolution fluorescence imaging and molecular quantification.*; Laser Photon. Rev. 2009, 3, 180-202

[74] Andréasson, J. ; Pischel, U.; *Storage and Processing of Information Using Molecules: The All-Photonic Approach with Simple and Multi-Photochromic Switches.* Israel Journal of Chemistry 2013, vol. 53(5), pp. 236-246.

[75] Irie M.; *Photochromism: Memories and Switches-Introduction.*; Chem Rev. 2000, 100(5), 1683-1684

[76] Wiktor Szymański, John M. Beierle, Hans A. V. Kistemaker, Willem A. Velema, and Ben L. Feringa; *Reversible Photocontrol of Biological Systems by the Incorporation of Molecular Photoswitches*; Chemical Reviews 2013, 113 (8), 6114-6178

[77] Ivan Aprahamian; *Hydrazone switches and things in between*; Chemical Communications 2017, 53, 6674-6684.

[78] Hatano, S.; Horino, T.; Tokita, A.; Oshima, T.; Abe, J.; *Unusual Negative Photochromism via a Short-Lived Imidazolyl Radical of 1,1'-Binaphthyl-Bridged Imidazole Dimer.* J. Am. Chem. Soc. 2013, 135, 3164-3172.

[79] Lerch M. M.; Szymanski W.; Feringa B. L.; *The (photo)chemistry of Stenhouse photoswitches: guiding principles and system design.* Chem. Soc. Rev. 2018, 47, 1910-1937

[80] D. Bleger, S. Hecht; *Visible-Light-Activated Molecular Switches* Angew. Chem. Int. Ed. 2015, 54, 11338-11349

[81] Feringa, B. L., Browne, W. R., Eds.; *Molecular Switches*, 2nd ed.; Wiley-VCH: Weinheim, 2011; Chapter 1

[82] D. van Dijken, Petr Kovaříček, Svante P. Ihrig, Stefan Hecht; *Acylhydrazones as Widely Tunable Photoswitches*; Journal of the American Chemical Society 2015, 137 (47), 14982-14991

[83] Andras Csehi, Lajos Ille, Gabor J. Halasza, Agnes Vibokb; *The effect of chemical substituents on the functionality of a molecular switch system:*

a theoretical study of several quinoline compounds; Phys. Chem. Chem. Phys.,2013, 15, 18048

[84] Baihao Shao, Hai Qian, Quan Li, Ivan Aprahamian, *Structure Property Analysis of the Solution and Solid-State Properties of Bistable Photochromic Hydrazones* Journal of the American Chemical Society 2019 141 (20), 8364-8371

[85] H. Qian, S. Pramanik, I. Aprahamian; *Photochromic Hydrazone Switches with Extremely Long Thermal Half-Lives*; J. Am. Chem. Soc. 2017, 139, 27, 9140–9143

[86] Bernard Mravec, Šimon Budzák, Miroslav Medved', Lukáš F. Pašteka, Chavdar Slavov, Torben Saßmannshausen, Josef Wachtveitl, Jozef Kožíšek, Lea Hegedüsová, Juraj Filo, and Marek Cigáň; *Design of High-Performance Pyridine/Quinoline Hydrazone Photoswitches* The Journal of Organic Chemistry 2021 86 (17), 11633-11646

[87] Gang Wang, Yazhen Li, Tingting Song, Congdi Shang, Jiawei Yang, Makroni Lily, Yu Fang, and Fengyi Liu; *Fluorescence Toggling Mechanism of Photochromic Phenylhydrazones: N–N Single Bond Rotation-Assisting E/Z Photoisomerization Differs from Imine.*; The Journal of Physical Chemistry A 2020 124 (32), 6411-6419

[88] Baihao Shao, Hai Qian, Quan Li, Ivan Aprahamian, *Structure Property Analysis of the Solution and Solid-State Properties of Bistable Photochromic Hydrazones* Supporting information DOI: 10.1021/jacs.9b03932

[89] Ragnoni E, Di Donato M, Iagatti A, Lapini A, Righini R.; *Mechanism of the intramolecular charge transfer state formation in all-trans-β-apo-8'-carotenal: influence of solvent polarity and polarizability* J Phys Chem B. 2015 Jan 15;119(2):420-32

[90] Iagatti, A.; Shao, B.; Credi, A.; Ventura, B.; Aprahamian, I.; Di Donato, M. Beilstein *Ultrafast processes triggered by one- and two-photon excitation of a photochromic and luminescent hydrazone*; J. Org. Chem. 2019, 15, 2438–2446.

[91] J. Mattay, *Photoinduced Electron Transfer I.* Springer-Verlag Berlin Heidelberg, 1990

[92] J. R. Lakowicz, *Principles of Fluorescence Spectroscopy.* Springer, 2006.

[93] Zhang, N. *Planar Waveguide Solar Concentrator with Couplers Fabricated by Laser-Induced BacksideWet Etching. Master's Thesis*, University of Toledo, Toledo, OH, USA, 2013.